University of Reading

Synoptic-scale mixing and precipitation:

A new perspective on convergence zones

Gabriel Martins Palma Perez

A thesis submitted for the degree of
Doctor of Philosophy

Department of Meteorology
University of Reading,
United Kingdom

September, 2022

Declaration

I confirm that this is my own work and the use of all material from other sources has been properly and fully acknowledged.

Gabriel M P Perez

Abstract

Variations in the location, intensity and duration of precipitation impact ecosystems and human activities such as agriculture, energy generation, and water reserves for human and animal consumption. Observation shows that persistent and intense precipitation often happens under synoptic-scale filaments of high moisture concentration; such events are typically referred to as convergence zones. Filaments of high tracer concentration emerge as a consequence of the deformation of fluid parcels during the process of fluid mixing. However, the mathematical basis to objectively identify coherent mixing features is relatively recent and the associated computational tools are lacking for meteorological datasets. Thus, it is unquantified the extent at which global precipitation depends on the horizontal mixing at synoptic timescales. It is also not known whether this framework can provide a basis for the development of convergence zone detection algorithms.

This thesis adapts the framework of mixing to identify atmospheric structures where the synoptic-scale kinematics favours the accumulation and filamentation of moisture in reanalyses and climate model data. Case-studies show that precipitation and moisture organise around coherent mixing features while climatological analyses show that precipitation anomalies during high mixing events are consistent with the convergence zone literature. It is shown that more than 60% of

the monthly precipitation variability can be explained by synoptic-scale mixing in many tropical and subtropical regions. Globally, more than half of precipitation falls during convergence zone events. The capability of climate models to reproduce convergence zone precipitation is evaluated in comparison with observational estimates: all of the analysed models overestimate the contribution of convergence zones to the total precipitation between approximately 7% and 20%. The proposed framework is revealed to be a promising process-based diagnostic to investigate mechanisms of precipitation variability and identifying circulation errors in weather and climate models which lead to errors in predicted precipitation.

Acknowledgements

First and foremost, I am deeply grateful to my parents, whose unwavering support and sacrifices have made this journey possible. Their belief in the value of education and their encouragement have been my greatest inspiration.

I would also like to extend my heartfelt thanks to my past mentors at the University of São Paulo. In particular, I am indebted to my MSc supervisor, Prof. Maria Assunção F. Dias, for her guidance and wisdom, as well as to my research colleague Thomas Martin, who has been a constant source of collaboration and insightful discussions.

At the University of Reading, I have had the privilege of working under the mentorship of Prof. Pier Luigi Vidale, whose expertise and encouragement have been instrumental in shaping my research. My cosupervisor, Dr. Helen Dacre, has been an invaluable guide throughout this process, and I am immensely thankful for her support. I am also deeply appreciative of Prof. Ted Shepherd and Prof. John Methven, whose insightful discussions about Lagrangian kinematics greatly enriched my understanding and academic growth. Prof. David Brayshaw, head of my monitoring committee, has also been of great support incentive throughout these years.

Finally, I am thankful for the camaraderie of my fellow PhD colleagues at the University of Reading, including James Fallon, Noel Clancy, Pinelopi Louizou, Wilfred Calder-Potts and many others. Their friendship and support made my time abroad not only more productive but also genuinely enjoyable. To all those who have contributed to this journey, whether mentioned here or not, my deepest thanks.

Authorship of papers

This thesis presents three papers as result chapters. The first paper has been published in *Weather and Climate Dynamics*, the second paper has been accepted in the *Journal of Climate* and the third one is a draft to be submitted to the *Journal of Geophysical Research*. The first two papers are unmodified from the accepted versions except from minor typographical adjustments and reformatting.

- Paper 1 - **Perez, Gabriel M P**, Pier Luigi Vidale, Nicholas P. Klingaman, and Thomas Martin. 2021. "Atmospheric convergence zones stemming from large-scale mixing". *Weather and Climate Dynamics*, 2 (2), 475–488.

  In this paper my contribution amounts to approximately 85%. I conceived the idea of applying the mixing framework to convergence zones, developed the associated computational tools, performed all the analysis and wrote the manuscript. Author Thomas Martin provided assistance with the implementation of the computational tools. Authors Pier Luigi Vidale and Nicholas Klingaman commented on the manuscript and discussed the results at all stages. Two anonymous reviewers provided comments on one earlier version of the manuscript

- Paper 2 - **Perez, Gabriel M P**, Pier Luigi Vidale, Helen Dacre and Jorge

Garcia-Franco. 2022. "Using a synoptic-scale mixing diagnostic to explain global precipitation variability from weekly to interannual timescales". *Journal of Climate*, In Press.

In this paper my contribution amounts to approximately 80%. I developed the methodology, performed most of the analysis and wrote the manuscript. The analysis of the influence of the North Atlantic Oscillation on South America was conceived along with author Garcia-Franco. Authors Pier Luigi Vidale and Helen Dacre commented on the manuscript and discussed the results at all stages. Prof. Heini Wernli and an anonymous reviewer provided comments on two earlier versions of the manuscript.

- Paper 3 - **Perez, Gabriel M P**, Pier Luigi Vidale, Helen Dacre and Thomas Martin. "How much does it rain over convergence zones? Assessing observations and climate model biases". To be submitted to the *Journal of Geophysical Research*.

  In this draft paper my contribution amounts to approximately 85%. I developed the methodology, performed most of the analysis and wrote the manuscript. All authors commented on the manuscript and discussed the results at all stages.

Contents

List of Figures

List of Tables

Acronyms

AMIP Atmospheric Model Intercomparison Project.

AMS American Meteorological Society.

CDF Cumulative Density Function.

CMIP Coupled Model Intercomparison Project.

CMORPH Climate Prediction Center morphing method.

CZ convergence zone.

DJF December-January-February.

ECMWF European Centre for Medium-range Weather Forecast.

ENSO El-Niño Southern Oscillation.

EOF Empirical Orthogonal Function.

ERA5 5^{th} generation of the ECMWF atmospheric reanalysis.

ETC extratropical cyclone.

FTLE Finite-Time Lyapunov Exponent.

GCM general circulation model.

GPCP Global Precipitation Climatology Project.

GPCP-1DD Global Precipitation Climatology Project 1° daily precipitation analysis.

ITCZ Intertropical Convergence Zone.

JJA June-July-August.

LCS Lagrangian Coherent Structure.

MAM March-April-May.

MCC mesoscale convective complexes.

MJO Madden-Julian Oscillation.

MSLP mean sea-level pressure.

NAO North Atlantic Oscillation.

PDF probability density function.

PLS Partial Least Squares.

PSA Pacific-South American.

RHS right hand side.

SACZ South Atlantic Convergence Zone.

SALLJ South American Low-Level Jet.

SAMS South American Monsoon System.

SICZ South Indian Convergence Zone.

SON September-October-November.

SPCZ South Pacific Convergence Zone.

SST sea surface temperature.

TCWV total column water vapour.

Chapter 1

Introduction

> "A particular idea becomes general by being made to represent all other particular ideas of the same sort."
>
> George Berkeley, *A treatise concerning the principles of human knowledge*

Precipitation directly impacts natural livelihoods, activities and well-being on a wide range of spatio-temporal scales. In urban centres, precipitation events may reduce traffic speed (Zhang et al. 2019), promote traffic accidents (Sherretz and Farhar 1978) and lead to flash floods (Marengo et al. 2020). A recent tragic example are the flash floods a landslides that caused 231 human deaths in February 2021 in the State of Rio de Janeiro, Brazil (Alcântara et al. 2022). On weekly and longer timescales, precipitation variability impacts agriculture and hydropower generation (Silveira et al. 2019); prolonged periods of drought may threaten water supplies for human and animal consumption (Hillman and Hillman 1977; Coelho et al. 2016). The impact of interannual precipitation trends on certain animal populations is even more substantial than temperature trends (Herrando et al. 2019).

Plants also suffer from variations and changes in the precipitation regime. For example, the intensification of the dry season in South America increases the risk of forest dieback in the Amazon, which, in its turn, may contribute to further enhancing the regional dry season (Zemp et al. 2017).

Despite the accumulated advances in numerical weather prediction (Bauer et al. 2015), numerical models still struggle to anticipate extreme precipitation events even at relatively short lead times of one day or less (Hamill 2014; Sukovich et al. 2014). At lead times longer than two weeks, the performance of sub-seasonal forecast systems to predict week-to-week variations substantially drops (Klingaman et al. 2021). On decadal or longer timescales, climate models disagree both in terms of intensity and sign of regional precipitation changes; this uncertainty appears to originate from the atmospheric circulation-related aspects of climate change (Shepherd 2014). Therefore, it is crucial to understand the atmospheric mechanisms controlling precipitation and develop diagnostics that disentangle sources of error and uncertainty in weather and climate predictions, with the aim to increase their reliability.

1.1 Large-scale precipitation mechanisms and their intersection with mixing concepts

Precipitation often occurs within synoptic-scale filaments of high water vapour concentration, the type of which can be visualised in satellite images and are usually denominated as "convergence zones" (CZs). Filaments of high tracer concentration in the large-scale atmospheric flow arise from the Lagrangian stretching

and folding of air parcels (Welander 1955; Aref 1984); a process simply known as mixing[1] (Ottino 1989; Pierrehumbert 1991). Mixing diagnostics, however, have not yet been employed to diagnose precipitation or identify CZs.

Although mixing is a central concept in the study of the transport of tracers and atmospheric properties (Methven and Hoskins 1999; Shepherd et al. 2000), climatologies of mixing diagnostics are scarce in the literature; the only global climatological study I encountered is in Garaboa-Paz et al. 2017. Moreover, I could not find studies investigating the role of synoptic-scale mixing in precipitation apart from Garaboa-Paz et al. 2015, who link a mixing diagnostic to atmospheric rivers in the North Atlantic. This scarcity of studies can be explained by two reasons: (i) the relatively recent development of the mathematical framework to quantify mixing and identify distinct mixing features (Haller and Yuan 2000; Shadden et al. 2005, see review in Haller 2015) and (ii) the absence of computational tools to easily extract such diagnostics from atmospheric data. Quantifying the link between synoptic-scale horizontal mixing and precipitation could lead to a better understanding of the underlying mechanisms and impacts of CZs and provide an automated tool for their identification on global atmospheric datasets.

Currently, most automated CZ identification algorithms have been based on (i) regional characteristics of scalar fields such as precipitation or cloudiness, that are unable to produce global climatologies or (ii) Eulerian metrics that fail to represent the Lagrangian nature of moisture transport in the atmosphere (Carvalho et al. 2004; Van Der Wiel et al. 2015; Ambrizzi and Ferraz 2015; Weller et al. 2017; Zilli and Hart 2021). In this section I review the literature on CZs and similar

[1]Some authors, such Methven and Hoskins 1999, prefer the term "stirring", but here I adopt "mixing" following Ottino 1989.

coherent precipitation bands, discussing their intersection with concepts of mixing from tracer transport studies; I also expand on the limitations of existing CZ definitions and detection algorithms.

1.1.1 Intertropical convergence zone

The Intertropical Convergence Zone (ITCZ) was first described as a region of encounter of air parcels from the northern and southern hemispheres (Simpson 1947); in other words, a region of high mixing where parcels originating in distant regions meet. This Lagrangian idea is still present in the Glossary of the AMS, that defines the ITCZ as: *"the dividing line between the southeast trades and the northeast trades"*. Its zonal-mean position is co-located with the ascending branch of the Hadley cell and its seasonal displacement is correlated with cross-equatorial energy fluxes (Donohoe et al. 2013). Despite its original association with parcel trajectories, a review of ITCZ identification methods (Nicholson 2018) reveals that none of the existing algorithms employs Lagrangian concepts. Schneider et al. 2014 identify the ITCZ as a region of maximum time-mean precipitation. Siongco et al. 2015 propose an object-detection algorithm to identify aspects of the ITCZ as precipitation clusters. Berry and Reeder 2014 employ an Eulerian convergence diagnostic, combined with thermodynamic masks, to derive the position of the ITCZ. An automated algorithm was proposed by Castelli et al. 2018 to derive the position of the ITCZ based on infra-red estimates of total column water vapour (TCWV).

It is crucial to understand and predict the variability and changes in the ITCZ since it is a major driver of precipitation in many tropical land areas. The ITCZ di-

rectly influences extreme precipitation events in Northeast Brazil (Cavalcanti 2012) and played an important role in the 2014 record drought in Singapore (McBride et al. 2015). Its seasonal migration, combined with monsoon systems, explain a substantial part of the rainfall seasonality in most tropical land masses such as Africa (Nicholson 2018), South America (Marengo et al. 2012), the Maritime Continent (Hassim and Timbal 2019) and Asia (Gadgil 2018). However, general circulation models (GCMs) present important limitations in simulating ITCZ precipitation. For example, Coupled Model Intercomparison Project (CMIP) models present a double-ITCZ bias (Adam et al. 2018; Tian and Dong 2020); i.e., climate models simulate a secondary convergence zone in the equatorial South Atlantic and southeastern Pacific. In the European Centre for Medium-range Weather Forecast (ECMWF) seasonal hindcasts, the ITCZ systematically drifts northward in the western Pacific (Shonk et al. 2018).

1.1.2 Subtropical convergence zones

While the ITCZ was originally described as an airmass interface, subtropical CZs were first identified as semi-stationary cloud bands in early satellite images of the Southern Hemisphere by Streten 1973. The author analysed 5-day mean fields between 1968 and 1971 and identified major cloudiness bands associated with troughs in the South Pacific, South Atlantic and Indian oceans. Kodama 1992 investigated the common features between the Baiu frontal zone in East Asia and the subtropical CZs in the Southern Hemisphere; two of the common aspects outlined by the author were: (i) they are poleward boundaries of tropical air masses and (ii) they are associated with strong horizontal moisture gradients. These two

aspects are essentially Lagrangian and defining characteristics of regions of high mixing.

Despite the Lagrangian concepts noticed by Kodama in the early 1990s, diagnostics of subtropical CZs almost exclusively employ cloudiness and/or precipitation as a central criteria, frequently without any considerations about the wind field (Carvalho et al. 2004; Ambrizzi and Ferraz 2015). In fact, the underlying kinematics or dynamics are often revealed after the CZ is detected based on cloudiness (Zilli and Hart 2021). In summary, existing diagnostics are well equipped to answer questions of the type: *"given a certain organised cloudiness/precipitation pattern, what are the associated circulation and dynamical mechanisms?"*. However, some studies present evidence derived from cloudiness-based CZ diagnostics to support conclusions about the impact of CZs on regional precipitation regimes (Carvalho et al. 2004); since cloudiness is closely related to precipitation, this incurs in a certain degree of circularity (Section 1.3 expands the discussion on this issue).

In terms of dynamical mechanisms, there is abundant evidence that organised diagonal cloud bands in the subtropics are conditioned to the presence of Rossby waves (Van Der Wiel et al. 2015; Zilli and Hart 2021). Rossby waves skew the kinetic energy spectrum to lower frequencies, which increases the probability of structures of high mixing and favours tracer filamentation (Shepherd et al. 2000). In studies of tracer evolution, this regime is known as "spectrally nonlocal" (Bennett 1984), where the fine scale distribution of tracers (i.e., the width of the tracer filaments) is controlled by the large wavenumbers. Therefore, observations of subtropical CZs conditioned to Rossby waves is consistent with the theory of mixing and supports an attempt to employ a mixing framework to diagnose such subtropical cloud bands.

1.1.3 Moisture filaments and mixing in the mid-latitudes

Filaments of high water vapour concentration arise in the mid-latitudes as extratropical cyclones (ETCs) sweep up moisture ahead of cold fronts (Dacre et al. 2015). Such moisture filaments are typically not exactly co-located with the fronts, even though both the temperature (used to define fronts) and moisture fields are subject to the same mixing caused by the cyclone motion. This is because not only energy and moisture are ruled by different conservation laws and distinct sources and sinks, but the spatial distribution of these variables during early stages of cyclogenesis is also different. Mixing acts upon existing gradients in order to reshape their spatial distributions (Lapeyre 2002); therefore, moisture and temperature gradients are not expected to become exactly parallel when under the action of extratropical cyclones (ETCs) mixing.

Nonetheless, mixing features have been identified in the neighbourhood of both fronts and atmospheric rivers. Cohen and Kreitzberg 1997 computed the Lagrangian deformation of back-trajectories in the neighbourhood of a cyclone to identify airstream boundaries, regions of high mixing interfacing air masses that originated in distinct regions. Garaboa-Paz et al. 2015 identified mixing features parallel to atmospheric rivers. The fact that mixing features have been observed in association with both fronts and atmospheric rivers highlights the important role of mixing in the mid-latitudes: gradients of variables with distinct sources and sinks and distinct initial distributions (i.e., temperature and moisture) become aligned due to the ETC motion.

Cohen and Schultz 2005 and Thomas and Schultz 2019 identify airstream boundaries with an instantaneous (Eulerian) contraction rate that corresponds

to a first-order approximation of the Lagrangian deformation computed in Cohen and Kreitzberg 1997. Weller et al. 2017 applied a line joining algorithm on the Eulerian divergence field to identify convergence lines. Although these approaches are a practical substitute for the more computationally heavy Lagrangian diagnostics, they are not appropriate to investigate mixing features underlying moisture distribution. This is because trajectories cannot be reasonably approximated by streamlines within the median residence time of water vapour; that is estimated to be between 4-5 days in a global average and range between 1 and 8 days in different regions (Läderach and Sodemann 2016). This inadequacy can be concluded by a simple scale analysis in the same spirit of Equations 6 to 8 in Doswell III 1984: the Lagrangian deformation is only reasonably approximated by the Eulerian deformation if the first-order term in a Taylor expansion of the trajectories is at least one order of magnitude (10 times) larger than the higher order terms. This results in the inequality $\Delta t < T/10$, where Δt is the time interval where the instantaneous approximation is valid and T is the timescale of motion. If we consider T a synoptic timescale between 2 and 4 days (typical lifetime of an ETC), then, Δt will lie between 5 and 10 hours, which is much shorter than the median residence time of water vapour.

1.2 Convergence zone detection for assessing model precipitation

Leung et al. 2022 classify model precipitation diagnostics into (1) spatiotemporal characteristics metrics, (2) process-oriented and (3) phenomena-based approaches.

Phenomena-based approaches attribute precipitation to specific atmospheric features such as fronts and atmospheric rivers and, combined with the other two diagnostics may help disentangle sources of model biases and contribute to model improvement. In the previous sections, we have seen that most algorithms are tuned to capture specific CZs such as the ITCZ and the SACZ. Therefore, it is currently not possible to quantify the role of CZs in the hydrological cycle and to assess the model biases associated with these features globally.

Climate model precipitation biases have been attributed to specific convergence zones such as the ITCZ and the South Atlantic Convergence Zone (SACZ) (Mechoso et al. 1995; Custodio et al. 2017; Tian and Dong 2020). However, this has been performed using spatiotemporal analyses of precipitation. Therefore, it is not known whether these errors are due to a misrepresentation of the large-scale kinematics underlying convergence zones or if they stem from other sources, such as column-physics parametrization. Systematically identifying CZs as regions of high mixing may provide a new way of disentangling model precipitation errors.

1.3 Epistemic limitations of existing convergence zone definitions

To a certain extent, this thesis proposes a fresh look at convergence zones with a new definition based on the mixing of the synoptic flow. Therefore, I believe that it is useful to present to the reader my view on why a new definition is needed. While some practical limitations have been discussed in the previous sections (e.g., existing definitions are region-specific), this section is dedicated to

clarify the epistemic limitations of the current CZ definitions. In other words, I aim to clarify the type of scientific question that can be answered with the approach proposed here that cannot be answered with the usual approaches. Particularly, I am contrasting the approach proposed here with "moist" definitions of CZs that employ precipitation or variables that almost directly translate into precipitation, such as cloudiness or the convergence of the vertically integrated moisture flux (Gadgil and Guruprasad 1990; Carvalho et al. 2004; Ambrizzi and Ferraz 2015). Let us consider the following question of interest:

Q1: What is the impact of convergence zones on precipitation?

If, for example, our hypothesis is that CZs increase the probability of precipitation, in Bayesian language, we need to ascertain if $\Pr(P|C) > \Pr(P)$, where $\Pr(P)$ is the prior probability of a precipitation event P and C is a circulation pattern that defines convergence zone events. In other words, for the hypothesis to be true, the occurrence of a CZ circulation pattern (CZ event) must increase the probability of occurrence of precipitation.

However, existing moist algorithms are suitable to investigate a different question. Since they are designed to capture events based on cloudiness or precipitation (P), they can be used to ascertain if the occurrence of P changes our belief that a circulation C is in place at the time. In probability terms, moist algorithms are suitable to ascertain if $\Pr(C|P) > \Pr(C)$. From the Bayes theorem, we can immediately see that this is different than answering **Q1** because $\Pr(P|C) \neq \Pr(C|P)$. Nonetheless, this type of reasoning can be useful to answer questions of the following kind:

Q2: Given a precipitation/cloudiness pattern, what are the circulation

patterns in place?

Zilli and Hart 2021, for example, answer **Q2** by showing that Rossby wave trains are precursors of diagonal cloud bands in South America.

Another epistemic problem that is introduced when trying to answer **Q1** with moist diagnostics is circularity. Consider the following statement:

> *Convergence zones are important to the precipitation regime because they are associated with significant precipitation anomalies.*

Here, the degree of change in the belief that convergence zones are important for precipitation depends on the strength of the presented evidence (the precipitation anomalies). However, if convergence zones are themselves defined as regions of strong precipitation (or cloudiness), then, the evidence is simply a re-statement of the claim, leading to no belief revision. Although circularity is not necessarily problematic and widely used in science, evidences lose their power when they are nearly direct re-statements of the claim they are supporting. Therefore, analysing precipitation anomalies during CZ events is more informative to answer **Q1** when CZs are defined by circulation diagnostics rather than moist diagnostics. A modern review of the problem of circularity in science can be found in Hahn 2011.

The problem of confirmation bias can also arise when answering **Q1** with moist diagnostics. If CZs are defined based on the prior expectation that they are regions of intense and lasting precipitation, such as in Ambrizzi and Ferraz 2015, the answer to **Q1** will (unsurprisingly) be that they significantly impact the precipitation regime. Nonetheless, some of the most cited studies in the CZ literature define CZs as regions of intense and lasting cloudiness and conclude that CZs increase the probability of high precipitation accumulations (e.g., Fig. 16 in Carvalho et al.

2004). In this thesis, by defining CZs purely based on horizontal mixing, we mitigate the problems of circularity and confirmation bias, allowing scientific questions related to **Q1** to be answered more soundly.

1.4 Objectives and thesis outline

Lagrangian concepts related to mixing, such as airmass boundary and gradient intensification, have been previously used to describe CZs and similar large-scale precipitation mechanisms. However, mixing has not yet been systematically employed to investigate precipitation. Moreover, existing definitions of CZs are based on automated algorithms that either employ: (i) Eulerian diagnostics that are not representative of moisture transport or (ii) moist diagnostics, such as cloudiness, that are region-specific and fall into epistemic limitations when used to assess the impact of CZs on precipitation.

In this thesis, my general aim is to present to the broad meteorology readership a Lagrangian diagnostic of mixing features underlying synoptic-scale moisture accumulation and precipitation. The approach proposed here adapts the framework of Lagrangian Coherent Structures (LCSs) (Haller and Yuan 2000; Shadden et al. 2005) to diagnose mixing features in atmospheric datasets. With this new methodology, I address scientific questions that are related to **Q1**:

- First scientific question (**SQ1**): How relevant is synoptic-scale mixing to precipitation? Does the mixing diagnostics identify features that are consistent with the current understanding of convergence zones and similar moisture/precipitation bands?

- Second scientific question (**SQ2**): Can we quantify the relationships between mixing and precipitation? In what regions/circumstances is this relationship more pronounced?

- Third scientific question (**SQ3**): What is the contribution of convergence zones to global precipitation? To what extent are precipitation biases in climate models related to the misrepresentation of convergence zones precipitation?

Aiming to answer the questions above, this thesis is composed of three result chapters, with the following specific objectives:

- **Chapter 2** is composed by a paper published in *Weather and Climate Dynamics* in 2021. The paper describes the mathematical framework of mixing and LCSs, as well as the algorithmic details of its implementation on atmospheric reanalyses data. The method is then used to address **SQ1** in South America. It is found that the signature of LCS events is consistent with previous studies about the SACZ, the ITCZ and other large-scale precipitation mechanisms in the region.

- **Chapter 3** consists of a paper accepted for publication in the *Journal of Climate*. In this study, the methodology of the first paper is expanded to a global domain and a climatology of mixing and its relationship with precipitation is provided. The results reveal that mixing and precipitation are related at temporal scales ranging from weather to annual and that the two variables present a high degree of co-variability in the tropics and subtropics, answering **SQ2**. Some aspects of the results are consistent with convergence

zone literature in many different regions, supporting the conclusion that the methodology can diagnose convergence zones globally.

- **Chapter 4** consists of a draft of a third paper, to be submitted to the *Journal of Geophysical Research*. The mixing diagnostic is adapted to assign precipitation to CZ events and quantify their global contribution to precipitation. In this study, the contribution of CZ precipitation to CMIP6 biases is investigated in terms of frequency and intensity errors. This study answers **SQ3**.

- **Chapter 5** is the Conclusions chapter, consisting of: (i) a summary and discussion of implications of the main results of this thesis, (ii) a discussion of limitations and recommendations for future work and (iii) the final remarks.

References

Adam, Ori, Tapio Schneider, and Florent Brient. 2018. "Regional and seasonal variations of the double-ITCZ bias in CMIP5 models". *Climate Dynamics* 51 (1): 101–117.

Alcântara, Enner, et al. 2022. "Deadly disasters in Southeastern South America: Flash floods and landslides of February 2022 in Petrópolis, Rio de Janeiro". *Natural Hazards and Earth System Sciences Discussions*: 1–27.

Ambrizzi, Tércio, and Simone ET Ferraz. 2015. "An objective criterion for determining the South Atlantic Convergence Zone". *Frontiers in Environmental Science* 3:23.

Aref, Hassan. 1984. "Stirring by chaotic advection". *Journal of fluid mechanics* 143:1–21.

Bauer, Peter, Alan Thorpe, and Gilbert Brunet. 2015. "The quiet revolution of numerical weather prediction". *Nature* 525 (7567): 47–55.

Bennett, AF. 1984. "Relative dispersion: Local and nonlocal dynamics". *Journal of Atmospheric Sciences* 41 (11): 1881–1886.

Berry, Gareth, and Michael J Reeder. 2014. "Objective identification of the intertropical convergence zone: Climatology and trends from the ERA-Interim". *Journal of Climate* 27 (5): 1894–1909.

Carvalho, Leila MV, Charles Jones, and Brant Liebmann. 2004. "The South Atlantic convergence zone: Intensity, form, persistence, and relationships with intraseasonal to interannual activity and extreme rainfall". *Journal of Climate* 17 (1): 88–108.

Castelli, Elisa, et al. 2018. "ITCZ trend analysis via Geodesic P-spline smoothing of the AIRWAVE TCWV and cloud frequency datasets". *Atmospheric Research* 214:228–238.

Cavalcanti, Iracema Fonseca Albuquerque. 2012. "Large scale and synoptic features associated with extreme precipitation over South America: A review and case studies for the first decade of the 21st century". *Atmospheric Research* 118:27–40.

Coelho, Caio AS, et al. 2016. "The 2014 southeast Brazil austral summer drought: regional scale mechanisms and teleconnections". *Climate Dynamics* 46 (11): 3737–3752.

Cohen, Robert A, and Carl W Kreitzberg. 1997. "Airstream boundaries in numerical weather simulations". *Monthly weather review* 125 (1): 168–183.

Cohen, Robert A, and David M Schultz. 2005. "Contraction rate and its relationship to frontogenesis, the Lyapunov exponent, fluid trapping, and airstream boundaries". *Monthly weather review* 133 (5): 1353–1369.

Custodio, Maria de Souza, et al. 2017. "Impact of increased horizontal resolution in coupled and atmosphere-only models of the HadGEM1 family upon the climate patterns of South America". *Climate Dynamics* 48 (9): 3341–3364.

Dacre, Helen F, et al. 2015. "How do atmospheric rivers form?" *Bulletin of the American Meteorological Society* 96 (8): 1243–1255.

Donohoe, Aaron, et al. 2013. "The relationship between ITCZ location and cross-equatorial atmospheric heat transport: From the seasonal cycle to the Last Glacial Maximum". *Journal of Climate* 26 (11): 3597–3618.

Doswell III, Charles A. 1984. "A kinematic analysis of frontogenesis associated with a nondivergent vortex". *Journal of Atmospheric Sciences* 41 (7): 1242–1248.

Gadgil, Sulochana. 2018. "The monsoon system: Land–sea breeze or the ITCZ?" *Journal of Earth System Science* 127 (1): 1–29.

Gadgil, Sulochana, and Asha Guruprasad. 1990. "An objective method for the identification of the intertropical convergence zone". *Journal of Climate* 3 (5): 558–567.

Garaboa-Paz, Daniel, Jorge Eiras-Barca, and Vicente Pérez-Muñuzuri. 2017. "Climatology of Lyapunov exponents: the link between atmospheric rivers and large-scale mixing variability". *Earth System Dynamics* 8 (3): 865–873.

Garaboa-Paz, Daniel, et al. 2015. "Lagrangian coherent structures along atmospheric rivers". *Chaos: An Interdisciplinary Journal of Nonlinear Science* 25 (6): 063105.

Hahn, Ulrike. 2011. "The problem of circularity in evidence, argument, and explanation". *Perspectives on Psychological Science* 6 (2): 172–182.

Haller, George. 2015. "Lagrangian coherent structures". *Annu. Rev. Fluid Mech* 47 (1): 137–162.

Haller, George, and Guocheng Yuan. 2000. "Lagrangian coherent structures and mixing in two-dimensional turbulence". *Physica D: Nonlinear Phenomena* 147 (3-4): 352–370.

Hamill, Thomas M. 2014. "Performance of operational model precipitation forecast guidance during the 2013 Colorado Front-Range floods". *Monthly Weather Review* 142 (8): 2609–2618.

Hassim, Muhammad EE, and Bertrand Timbal. 2019. "Observed rainfall trends over Singapore and the Maritime Continent from the perspective of regional-scale weather regimes". *Journal of Applied Meteorology and Climatology* 58 (2): 365–384.

Herrando, Sergi, et al. 2019. "Contrasting impacts of precipitation on Mediterranean birds and butterflies". *Scientific reports* 9 (1): 1–7.

Hillman, Jesse C, and Alison KK Hillman. 1977. "Mortality of wildlife in Nairobi National Park, during the drought of 1973–1974". *African Journal of Ecology* 15 (1): 1–18.

Klingaman, Nicholas P, et al. 2021. "Subseasonal prediction performance for austral summer South American rainfall". *Weather and Forecasting* 36 (1): 147–169.

Kodama, Yasumasa. 1992. "Large-scale common features of subtropical precipitation zones (the Baiu frontal zone, the SPCZ, and the SACZ) Part I: Characteristics of subtropical frontal zones". *Journal of the Meteorological Society of Japan. Ser. II* 70 (4): 813–836.

Läderach, Alexander, and Harald Sodemann. 2016. "A revised picture of the atmospheric moisture residence time". *Geophysical Research Letters* 43 (2): 924–933.

Lapeyre, Guillaume. 2002. "Characterization of finite-time Lyapunov exponents and vectors in two-dimensional turbulence". *Chaos: An Interdisciplinary Journal of Nonlinear Science* 12 (3): 688–698.

Leung, L Ruby, et al. 2022. "Exploratory precipitation metrics: spatiotemporal characteristics, process-oriented, and phenomena-based". *Journal of Climate* 35 (12): 3659–3686.

Marengo, JA, et al. 2012. "Recent developments on the South American monsoon system". *International Journal of Climatology* 32 (1): 1–21.

Marengo, Jose A, et al. 2020. "Trends in extreme rainfall and hydrogeometeorological disasters in the Metropolitan Area of São Paulo: a review". *Annals of the New York Academy of Sciences* 1472 (1): 5–20.

McBride, John L, et al. 2015. "The 2014 record dry spell at Singapore: an Intertropical Convergence Zone (ITCZ) drought". *Bulletin of the American Meteorological Society* 96 (12): S126–S130.

Mechoso, Carlos R, et al. 1995. "The seasonal cycle over the tropical Pacific in coupled ocean–atmosphere general circulation models". *Monthly Weather Review* 123 (9): 2825–2838.

Methven, John, and Brian Hoskins. 1999. "The advection of high-resolution tracers by low-resolution winds". *Journal of the Atmospheric Sciences* 56 (18): 3262–3285.

Nicholson, Sharon E. 2018. "The ITCZ and the seasonal cycle over equatorial Africa". *Bulletin of the American Meteorological Society* 99 (2): 337–348.

Ottino, Julio M. 1989. *The kinematics of mixing: stretching, chaos, and transport.* Vol. 3. Cambridge university press.

Pierrehumbert, RT. 1991. "Large-scale horizontal mixing in planetary atmospheres". *Physics of Fluids A: Fluid Dynamics* 3 (5): 1250–1260.

Schneider, Tapio, Tobias Bischoff, and Gerald H Haug. 2014. "Migrations and dynamics of the intertropical convergence zone". *Nature* 513 (7516): 45–53.

Shadden, Shawn C, Francois Lekien, and Jerrold E Marsden. 2005. "Definition and properties of Lagrangian coherent structures from finite-time Lyapunov exponents in two-dimensional aperiodic flows". *Physica D: Nonlinear Phenomena* 212 (3-4): 271–304.

Shepherd, Theodore G. 2014. "Atmospheric circulation as a source of uncertainty in climate change projections". *Nature Geoscience* 7 (10): 703–708.

Shepherd, Theodore G, John N Koshyk, and Keith Ngan. 2000. "On the nature of large-scale mixing in the stratosphere and mesosphere". *Journal of Geophysical Research: Atmospheres* 105 (D10): 12433–12446.

Sherretz, Lynn A, and Barbara C Farhar. 1978. "An analysis of the relationship between rainfall and the occurrence of traffic accidents". *Journal of Applied Meteorology and Climatology* 17 (5): 711–715.

Shonk, Jonathan KP, et al. 2018. "Identifying causes of western Pacific ITCZ drift in ECMWF System 4 hindcasts". *Climate Dynamics* 50 (3): 939–954.

Silveira, Cleiton Da Silva, et al. 2019. "Performance evaluation of AR5-CMIP5 models for the representation of seasonal and multi-annual variability of pre-

cipitation in Brazilian hydropower sector basins under RCP8. 5 scenario". *Hydrological Sciences Journal* 64 (11): 1279–1296.

Simpson, Robert H. 1947. "Synoptic aspects of the intertropical convergence near Central and South America". *Bulletin of the American Meteorological Society* 28 (7): 335–346.

Siongco, Angela Cheska, Cathy Hohenegger, and Bjorn Stevens. 2015. "The Atlantic ITCZ bias in CMIP5 models". *Climate Dynamics* 45 (5): 1169–1180.

Streten, Neil A. 1973. "Some characteristics of satellite-observed bands of persistent cloudiness over the Southern Hemisphere". *Monthly Weather Review* 101 (6): 486–495.

Sukovich, Ellen M, et al. 2014. "Extreme quantitative precipitation forecast performance at the Weather Prediction Center from 2001 to 2011". *Weather and forecasting* 29 (4): 894–911.

Thomas, Carl M, and David M Schultz. 2019. "Global climatologies of fronts, airmass boundaries, and airstream boundaries: Why the definition of "front" matters". *Monthly Weather Review* 147 (2): 691–717.

Tian, Baijun, and Xinyu Dong. 2020. "The double-ITCZ bias in CMIP3, CMIP5, and CMIP6 models based on annual mean precipitation". *Geophysical Research Letters* 47 (8): e2020GL087232.

Van Der Wiel, Karin, et al. 2015. "A dynamical framework for the origin of the diagonal South Pacific and South Atlantic convergence zones". *Quarterly Journal of the Royal Meteorological Society* 141 (691): 1997–2010.

Welander, Pierre. 1955. "Studies on the general development of motion in a two-dimensional, ideal fluid". *Tellus* 7 (2): 141–156.

Weller, Evan, et al. 2017. "Precipitation associated with convergence lines". *Journal of Climate* 30 (9): 3169–3183.

Zemp, Delphine Clara, et al. 2017. "Self-amplified Amazon forest loss due to vegetation-atmosphere feedbacks". *Nature Communications* 8 (1): 1–10.

Zhang, Weiwei, et al. 2019. "Impact analysis of rainfall on traffic flow characteristics in Beijing". *International Journal of Intelligent Transportation Systems Research* 17 (2): 150–160.

Zilli, Marcia T, and Neil CG Hart. 2021. "Rossby wave dynamics over South America explored with automatic tropical–extratropical cloud band identification framework". *Journal of Climate* 34 (20): 8125–8144.

Chapter 2

Atmospheric convergence zones stemming from large-scale mixing

This chapter has been published in *Weather and Climate Dynamics* with the following reference:

Perez, Gabriel M P, Pier Luigi Vidale, Nicholas P. Klingaman, and Thomas Martin. 2021. "Atmospheric convergence zones stemming from large-scale mixing". *Weather and Climate Dynamics*, 2 (2), 475–488.

Abstract

Organised cloud bands are important features of tropical and subtropical rainfall. These structures are often regarded as convergence zones, alluding to an association with coherent atmospheric flow. However, the flow kinematics is not usually taken into account in classification methods for this type of event, as large-scale lines are rarely evident in instantaneous diagnostics such as Eulerian convergence. Instead, existing convergence zone definitions rely on heuristic rules of shape, duration and size of cloudiness fields. Here we investigate the role of large-scale turbulence in shaping atmospheric moisture in South America. We employ the Finite-Time Lyapunov Exponent (FTLE), a metric of deformation among neighboring trajectories, to define convergence zones as attracting Lagrangian Coherent Structures (LCSs). Attracting LCSs frequent tropical and subtropical South America, with climatologies consistent with the South Atlantic Convergence Zone (SACZ), the South American Low-level Jet (SALLJ) and the Intertropical Convergence Zone (ITCZ). In regions under the direct influence of the ITCZ and the SACZ, rainfall is significantly positively correlated with large-scale mixing measured by the FTLE. Attracting LCSs in South and Southeast Brazil are associated with significant positive rainfall and moisture flux anomalies. Geopotential height composites suggest that the occurrence of attracting LCSs in these regions is related with teleconnection mechanisms such as the Pacific-South American. We believe that this kinematical approach can be used as an alternative to region-specific convergence zone classification algorithms; it may help advance the understanding of underlying mechanisms of tropical and subtropical rain bands and their role in the hydrological cycle.

2.1 Introduction

Large-scale organised zones of cloudiness and rainfall stand out in tropical and subtropical weather, which is otherwise dominated by non-organised convection. These cloud bands were initially identified in the equatorial belt (Alpert 1945) and associated with the interaction of inter-hemispheric air masses along the easterlies (Fletcher 1945; Simpson 1947); i.e., the Intertropical Convergence Zone (ITCZ). Despite these historical associations with coherent trajectories, convergence zones have been more frequently identified by heuristic rules applied to satellite imagery or cloudiness/rainfall data (Barros et al. 2000; Van Der Wiel et al. 2015; Ambrizzi and Ferraz 2015; Vindel et al. 2020). These approaches require detailed previous knowledge of the spatio-temporal characteristics of convergence zones in specific locations. Therefore, they do not provide a general definition for these events.

In other studies, convergence zones were characterized using the divergence of instantaneous or average velocity fields (Berry and Reeder 2014; Weller et al. 2017). These approaches are in principle more general. However, because Eulerian metrics such as divergence reveal instantaneous features in their immediate neighborhoods, they respond strongly to local processes such as convection. More generally, in unsteady flows, Eulerian features do not reveal the underlying structures of tracer mixing such as air mass interfaces (Boffetta et al. 2001; d'Ovidio et al. 2009). Rather, from the kinematics point of view, flow structures shaping tracer evolution are more suitably inspected under Lagrangian frameworks (Ottino 1989; Pierrehumbert 1991; Bowman 1999; Haller and Yuan 2000). By offering temporally integrated trajectory information, Lagrangian diagnostics synthesize pathline features that determine atmospheric transport.

In this study, we investigate attracting coherent structures arising from large-scale mixing in South America and their relationship with rainfall and water vapour. We propose that such structures are skeletons of atmospheric convergence zones and provide an identification criterion that can be applied to reanalyses and model data (Sections 2 and 3). In Section 4, we discuss the physical interpretation of the quantities involved. In Section 5, we discuss the methodology applied to a recent South Atlantic Convergence Zone (SACZ) event. Finally, we present their impacts on rainfall and moisture fluxes in South America (Section 6) and associate them with teleconnections (Section 7).

2.1.1 Mixing and Lagrangian coherent structures in the atmosphere

In time-dependent flows, advection reshapes the distribution of tracers into complex filamentous patterns (Aref 1984). This process of mixing intensifies tracer gradients and is characterised by the stretching and folding of parcels (Ottino 1989); it can be observed in the atmosphere on synoptic time scales even in relatively simple flows (Welander 1955). We consider convergence zones, from the point of view of mixing, as coherent structures associated with strong attraction of trajectories with the potential to organise moisture filaments or bands.

The Finite-Time Lyapunov Exponent (FTLE) is a convenient tool to visualize underlying structures of flow mixing. It is defined as the average separation rate among neighboring trajectories in a fixed propagation time interval. Ridges of the FTLE identify Lagrangian Coherent Structures (LCSs) (Haller 2001; Shadden et al. 2005), structures by which advected passive tracer is strongly attracted or

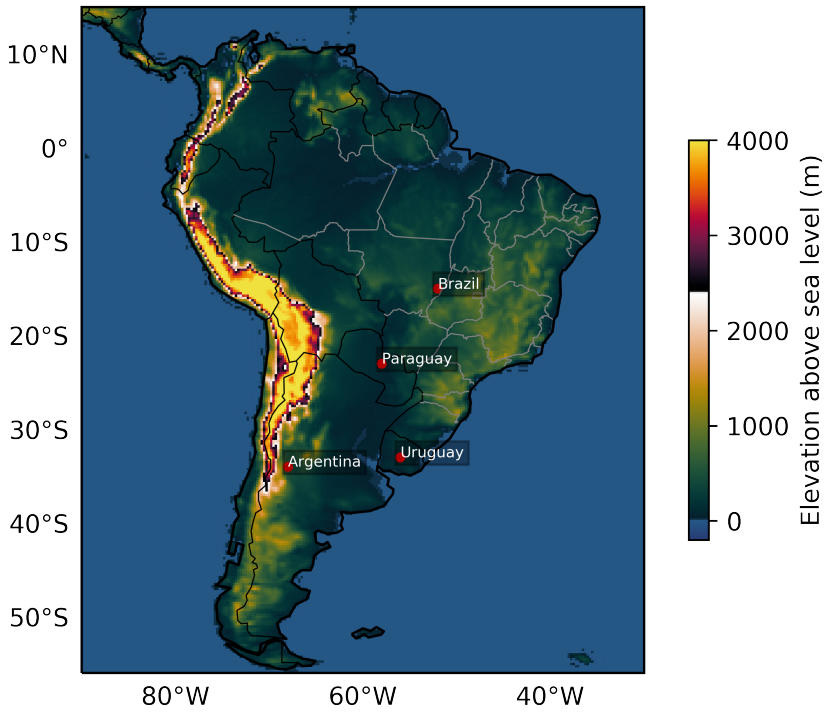

Figure 2.1: Elevation above the sea level. Derived from ECMWF's ERA5 surface geopotential.

repelled within the time interval of interest. While this is an active area of research and more rigorous methods to investigate Lagrangian coherence exist (Haller and Beron-Vera 2012; Farazmand et al. 2014), the FTLE has been employed in previous studies to investigate features of atmospheric and oceanic transport.

Pioneering studies by Pierrehumbert 1991 and Pierrehumbert and Yang 1993 applied the FTLE to investigate large-scale atmospheric mixing and tropics/extratropics transport barriers. Shepherd et al. 2000 computed probability density functions of the FTLE to investigate chaotic advection in the stratosphere. Rutherford et al. 2011 and Guo et al. 2016 employed the FTLE to visualize flow features in tropical cyclones. Garaboa-Paz et al. 2015 and Garaboa-Paz et al. 2017 suggested that FTLE ridges are closely linked to atmospheric rivers in boreal winter, when advec-

tion shapes the spatial distribution of water vapour. The criterion for convergence zones proposed here is closely related to the framework proposed by Garaboa-Paz et al. 2015 for atmospheric rivers. We leverage the framework of LCSs to investigate the underlying flow features organising rainfall and moisture accumulation in South America.

2.1.2 Aspects of the moisture transport in South America

The largest portion of the South American continent is located in tropical and subtropical latitudes (Figure 2.1). Along the western coast, the Andes mountain range extends across a considerable latitudinal interval as the dominant topographical feature. Its high altitudes pose a barrier to low and mid-tropospheric zonal flow. This barrier to the zonal flow deflects the climatological sea-to-land easterly flow as it enters the continent from the equatorial Atlantic, forming a meridional channel of north-to-south moisture transport between 850 and 700 hPa (Gimeno et al. 2016) that supplies moisture for rainfall in populated areas in southeastern and southern South America (Zemp et al. 2014). When intensified, this north-to-south moisture flux characterizes the South American Low-Level Jet (SALLJ) (Vera et al. 2006). Occasionally, the SALLJ resembles atmospheric rivers (Arraut et al. 2012; Poveda et al. 2014), filaments of intense moisture associated with the motion of extratropical cyclones (Dacre et al. 2015).

During austral summer, increased sensible heat flux from the land surface and latent heat released through Amazonian convection, combined with the southward seasonal shift of the ITCZ, intensify the sea-to-land moisture transport, characterising the wet phase of the South American Monsoon System (SAMS) (Marengo

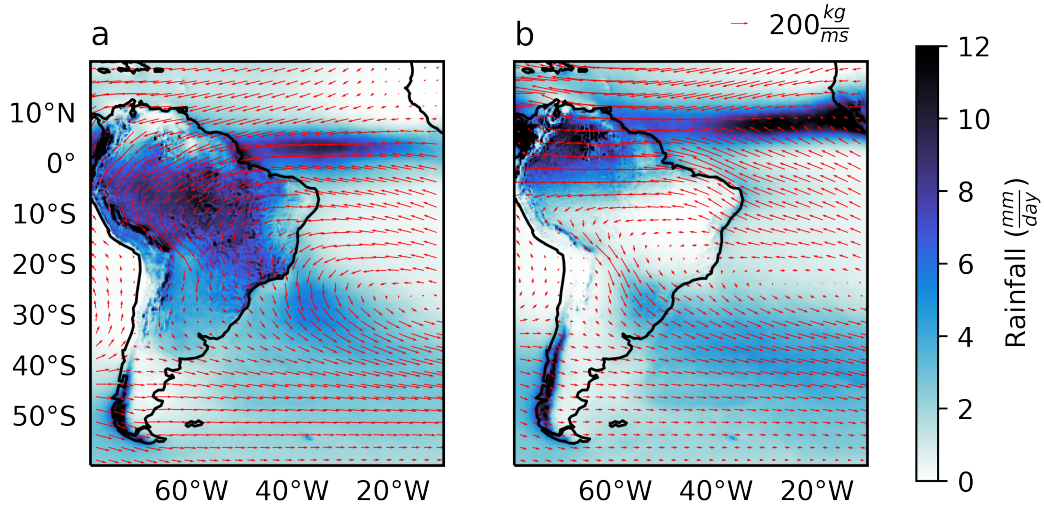

Figure 2.2: Mean rainfall and vertically integrated moisture flux (vectors) in December-January-February (DJF) (a) and June-July-August (JJA) (b). Averages were computed from ECMWF's ERA5 from 1980 to 2009.

et al. 2012). The SAMS can be illustrated by the contrast between rainfall and moisture flux climatologies in summer and winter (Figure 2.2). In summer, there is increased oceanic moist air input to the continent, associated with the tropical Atlantic easterlies and the South Atlantic subtropical high. The northeasterly moisture flux is deflected southeast after crossing the Amazon, supplying moisture for southeastern and southern South America (Zemp et al. 2014). This higher moisture input in summer coincides with higher rainfall, particularly in Central and Southeast Brazil. In winter, the angle of the easterlies in the Atlantic tilts northwards and the moisture flux from the South Atlantic subtropical high weakens, such that the moisture flux and rainfall are stronger in northernmost South America and weaker in most other parts of the continent. These observations point to the sensitivity of rainfall in central and southern South America to disruptions in the climatological SAMS moisture transport.

Extratropical cyclones are central to the synoptic scale variability of the South American climate. These structures originate most frequently in cyclogenesis regions spanning from South Argentina to the coast of Southeast Brazil (Crespo et al. 2021). These cyclones have an average life cycle of three days (Mendes et al. 2010); their associated cold fronts cause cold incursions (Lanfredi and Camargo 2018) and rainfall over the continent (Lenters and Cook 1999; Vera et al. 2002). In the wet season of the SAMS, the interaction between tropical sources of heat and moisture with extratropical cyclones resonate at submonthly scales often manifested as diagonally oriented (northwest-southeast) cloud bands (Nieto and Chao 2013; Raupp and Silva Dias 2010). The diagonal aspect of these cloud bands is a characteristic feature of the SACZ; it has been attributed to the deformation of low-level vorticity centres by equatorward Rossby waves originating from circulation anomalies in the Pacific (Van Der Wiel et al. 2015). This relationship renders circulation and rainfall in the SACZ region sensitive to the Pacific-South American (PSA) teleconnection patterns (Mo and Paegle 2001).

The objective definition and automatic identification of large-scale features shaping the moisture distribution in a long-term climatology is, thus, key to understanding the processes driving the seasonal and intraseasonal variability of the South American hydrological cycle. Currently, most identification algorithms for convergence zones focus on the SACZ and rely on rules of shape, duration and intensity of cloud bands usually given by an Empirical Orthogonal Function (EOF) analysis of outgoing longwave radiation or rainfall (Barros et al. 2000; Jorgetti et al. 2014; Van Der Wiel et al. 2015; Ambrizzi and Ferraz 2015). A drawback of cloudiness-based approaches is that they lack the means for attributing contributions from processes at different scales to a single cloud band. For example,

cloudiness originating from local convection adjacent to cloudiness originating from large-scale flow coherence would appear to be the same structure from a satellite image. Furthermore, describing a physical phenomenon with a single EOF is problematic, as EOFs do not necessarily individually correspond to dynamical modes and can produce patterns with little connection to physical processes (Dommenget and Latif 2002; Monahan et al. 2009; Fulton and Hegerl 2019).

2.2 Mathematical framework

2.2.1 Vertically scaled horizontal moisture flux

Water vapour in the atmosphere concentrates close to its source at the Earth's surface. Thus, it is natural to analyse features of moisture transport using the low-level flow. Weller et al. 2017 employed an Eulerian metric to identify convergence lines at 950 hPa over the Pacific Ocean and Australian landmass. Garaboa-Paz et al. 2017 investigated atmospheric rivers at 850 hPa. While water vapour is concentrated at lower levels, selecting a particular level becomes problematic near topography, such as the Andes, for two reasons: (a) topography often crosses lower tropospheric pressure levels; and (b) it causes the level of maximum moisture transport to rise in its vicinity (Insel et al. 2010). The SALLJ, for example, transports substantial amounts of water vapour and flows parallel to the Andes between 850 and 700 hPa (Gimeno et al. 2016).

We employed a horizontal flow $\boldsymbol{V}_{\rho_v}$ derived from a vertical scaling of the horizontal momentum $\boldsymbol{V}_H$ that takes into account the vertical distribution of water vapour density (ρ_v). The scaling divides the vertically integrated moisture flux

by the total column water vapour (Eq. 2.1). Physically, $\boldsymbol{V}_{\rho_v}$ is the average flow by which the total column water vapour is transported. A similar weighting was employed by Garaboa-Paz et al. 2015 to identify atmospheric rivers and by Ruiz-Vásquez et al. 2020 to investigate sources and sinks of water vapour in South America. It is important to notice, however, that strong vertical shear across heights of high moisture concentration may render $\boldsymbol{V}_{\rho_v}$ not representative of the actual horizontal pathways of moisture, obscuring the interpretation of attracting structures in this flow.

$$\boldsymbol{V}_{\rho_v} = \frac{\int_0^\infty \rho_v \boldsymbol{V}_H dz}{\int_0^\infty \rho_v dz}[m/s] \tag{2.1}$$

We expect $\boldsymbol{V}_{\rho_v}$ not to be affected by moisture sources and sinks as the water vapour density ρ_v is both in the numerator and denominator of Eq. 2.1 In other words, the resulting flow is independent of the horizontal water vapour distribution. The role of ρ_v in Eq. 2.1 is, thus, only to provide a vertical weighting to $\boldsymbol{V}_H$ such that moist levels are favoured. The following sections discuss how we computed the trajectory deformation and identified LCSs in $\boldsymbol{V}_{\rho_v}$.

2.2.2 Finite-time Lyapunov exponent

The FTLE measures the average deformation rate among initially close trajectories after a characteristic advection time $\Delta t = t_1 - t_0$, where t_1 and t_0 are respectively the times of arrival and departure of these trajectories. The flow-map $F_{t_0}^{t_1}$ (Eq. 2.2) links the departure position $\boldsymbol{x_0}(t_0)$ of a parcel to its arrival position $\boldsymbol{x_1}(t_1; \boldsymbol{x_0}, t_0)$, where $\boldsymbol{x_0}$ and $\boldsymbol{x_1}$ are in $\mathbb{R}^2$ representing positions on the Earth's surface (latitude and longitude points).

$$F_{t_0}^{t_1}(\boldsymbol{x_0}) := \boldsymbol{x_1}(t_1; \boldsymbol{x_0}, t_0) \tag{2.2}$$

The flow-map can be found at any given point in time and space by numerically integrating the trajectories for every departure point on a discrete grid:

$$\frac{D\boldsymbol{x}}{Dt} = \boldsymbol{V}_{\rho_v}(\boldsymbol{x}, t) \tag{2.3}$$

The exponential rate of separation of trajectories departing from the neighborhood of $\boldsymbol{x_0}$ is expressed by the FTLE, represented by σ:

$$\sigma(\boldsymbol{x_0}) = \frac{1}{|\Delta t|} ln\left(\sqrt{\lambda_{max}(C)}\right) \tag{2.4}$$

Where $\lambda_{max}(C)$ is most positive eigenvalue of the right-hand Cauchy-Green strain tensor (Eq. 2.5).

$$C = [\nabla F_{t_0}^t]^T \nabla F_{t_0}^t \tag{2.5}$$

The gradient of the flow-map $\nabla F_{t_0}^t$ was obtained by a centred finite-difference scheme (Haller 2001) by converting $\boldsymbol{x_0}$ and $\boldsymbol{x_1}$ from spherical to Cartesian coordinates in $\mathbb{R}^3$. Higher accuracy discretizations can be obtained by solving Equation 2.3 on unstructured meshes with adaptive resolution (Lekien and Ross 2010). A more detailed derivation of the FTLE and the Cauchy-Green strain tensor can be found in Haller 2015 and references therein.

The eigenvalue $\lambda_{max}(C)$ in Eq. 2.4 essentially quantifies the stretching or folding along the main axis of deformation experienced by a parcel undergoing transformation by the flow-map. If the time trajectories are propagated backwards (i.e.,

back-trajectories), the FTLE represents the exponential rate of folding; its ridges characterize attracting LCSs. In the forward-in-time case, the FTLE represents the stretching rate and its ridges identify repelling LCSs. As we are interested in the Lagrangian skeletons that potentially organise moisture accumulation and rainfall along a preferred axis, we employ the backwards-in-time convention to identify attracting LCSs as FTLE ridges. However, in principle attracting coherent structures could be identified by the most negative eigenvalue, this approach is not numerically accurate because the arrival points cannot be much closer than their original arrival distance.

Here we employ an integration time interval of $\Delta t = 2$ days, such that the trajectories are allowed to explore large-scale flow structures. This time scale is also not too long such that the effect of the typical extratropical cyclone, whose average life cycle is three days (Mendes et al. 2010), is filtered out. Although not shown here, features associated with the ITCZ and the SACZ were also found with other integration times (1, 3 and 4 days).

2.2.3 Convergence zones as FTLE ridges

While the scalar FTLE field at a given time characterizes chaotic mixing spatially, its ridges are associated with the most locally intense attraction of back-trajectories arriving in its neighborhood (Haller 2001; Allshouse and Peacock 2015). Here we simply define attracting LCSs as curvature ridges of the FTLE scalar field (Shadden et al. 2005). We also impose additional criteria of size and intensity (see Section 2.3) to further isolate strong attracting structures that are more likely to organise large-scale cloud bands.

Shadden et al. 2005 argue that the flux across curvature FTLE ridges is negligible. This would mean that LCSs defined as such could be regarded as transport barriers. While this is not always true and counterexamples exist (Haller 2011), FTLE can approximate transport barriers in geophysical flows such as stratrospheric circulations (Boffetta et al. 2001), oceanic currents in the Gulf of Mexico (Olascoaga et al. 2006) and subtropical and polar jets (Beron-Vera et al. 2012). Moisture flux anomalies in Section 2.5 indicate that FTLE ridges in Southeast Brazil act as barriers to important preferential pathways of moisture along the Andes, leading to negative rainfall anomalies in South Brazil and surroundings.

Therefore, by approximating transport barriers, our definition of convergence zone as attracting LCSs is also consistent with the association of convergence zones to air mass interfaces (Simpson 1947). Such interfaces can be characterized as sharp gradients of the flow-map that are directly represented in the scalar FTLE field.

2.3 Data and implementation

We computed $\boldsymbol{V}_{\rho v}$ (Eq. 2.1) using total column water vapour and the zonal and meridional components of the vertically integrated moisture flux at full spatial resolution ($\approx$ 30km) and 6-hourly time resolution from the ECMWF's ERA5 reanalysis between 1980 and 2009. Gridded rainfall data are also obtained from ERA5 at the same spatial and temporal resolutions.

The back-trajectories are calculated by numerically solving Eq. 2.3 with a two-time-level Lagrangian advection scheme (SETTLS, Hortal 2002), extrapolated in time iteratively using a second-order Taylor expansion. The velocity $\boldsymbol{V}_{\rho v}$ along the

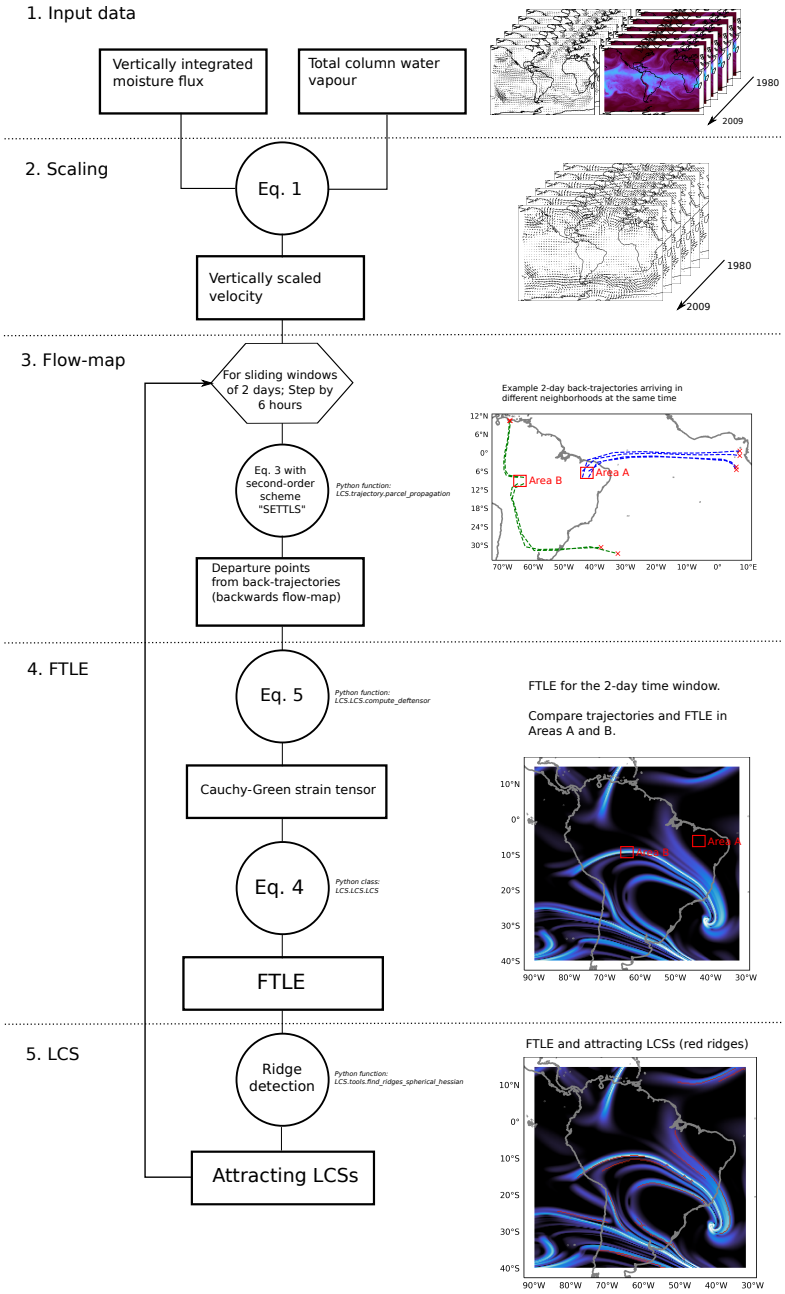

Figure 2.3: Schematic summary of the methodology employed to compute the FTLE and identify attracting LCSs. Corresponding Python classes and functions are referenced. See "Code and data availability" for repository link.

trajectories was interpolated with a bivariate spherical spline (Dierckx 1995). The intensity of the FTLE ridges is dependent on the accuracy of the advection scheme because numerical diffusion can weaken the gradients of the flow-map. The trajectory integration domain was chosen as a wide area ($180^oW/30^oE$, $85^oS/60^oN$) around South America in order to avoid boundary contamination in the domain of interest.

We identified candidate convergence zones as ridges of the FTLE scalar field by relaxing the criteria proposed by Shadden et al. 2005. The criteria involves isolating curves parallel to the FTLE gradient (condition SR1) and normal to the direction of most negative curvature of the FTLE scalar field (condition SR2). The latter is given by the eigendecomposition of the Hessian matrix. However, in practice, Shadden's criterion is too restrictive (Peikert et al. 2013). Peikert and Sadlo 2008 suggests relaxing SR1 by admitting a tolerance angle (ϵ_θ) between the curve representing the ridge and the gradient. We tested a range of ϵ_θ values and visually inspected the outputs to find that a tolerance angle of $\epsilon_\theta = 15^o$ produced satisfactory results. The derivatives for the gradient and the Hessian matrix were computed with a centered-difference scheme on the sphere.

Convergence zones were obtained by subsetting the candidate FTLE ridges by size and average intensity. Ridges with average FTLE ($\overline{\sigma}$) below 1.2 day^{-1} and major axis length (L) shorter than 500 km were discarded. While these thresholds are arbitrarily defined to filter out weaker and shorter structures, the relative distribution of convergence zones is robust to slight perturbations of the order of $\pm 20\%$. The steps to compute the FTLE and identify attracting LCSs are summarised in Figure 2.3 and the relevant parameters are listed in Table 2.1

Table 2.1: Summary of the parameters employed to compute the FTLE and its ridges (LCSs).

	Parameter	**Value**
FTLE	Spatial res.	$\approx$ 30km
	Temporal res.	6 hours
	Integration time	2 days
LCSs	ϵ_θ	$< 15^o$
	$\overline{\sigma}$	> 1.2 day^{-1}
	L	> 500 km

2.4 Interpreting the FTLE scalar field and LCSs

An important distinction in this study is the one between the FTLE scalar field and the attracting LCSs represented by ridges in this field. The FTLE field at a given time depicts the state of mixing in a particular integration time interval. Relatively high FTLE in the backwards-in-time perspective reveals regions where mixing is stronger. In such regions, the departure distance among parcels back-advected from neighboring arrival points is large. The FTLE represents this exponential folding rate along the principal axis of deformation. Regions where the FTLE is relatively low experience less mixing; i.e., arriving parcels departed from nearby locations. Ridges in this field correspond to the locally strongest attracting structures (i.e., attracting LCSs) associated with strong flow-map deformation. This relationship between trajectory deformation and the FTLE is exemplified in Figure 2.3.

Figures 2.4a and 2.4b represent the zonal and meridional components of the 2-day backwards flow-map on 24 January 2020 at 18 UTC. This event was classified by Brazilian meteorology agencies as a particularly strong SACZ associated with intense rainfall in Southeast Brazil (CPTEC 2020). The gradients of the departure positions represented in Fig. 2.4a and Fig. 2.4b are the components of

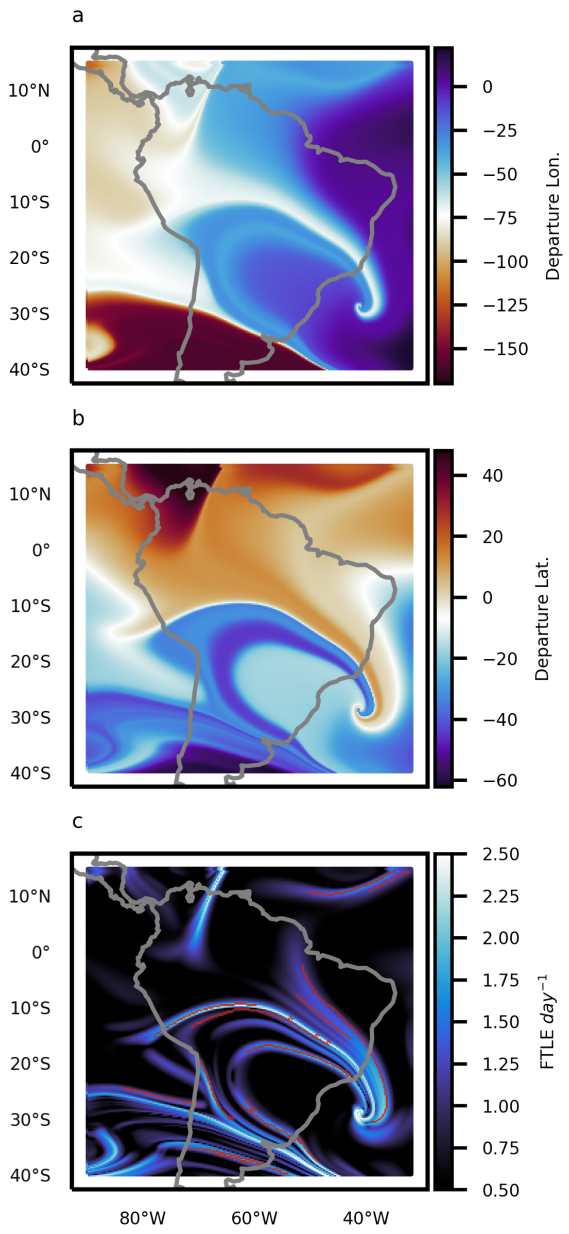

Figure 2.4: Example of the relationship between the meridional (a) and zonal (b) components of the flow-map, the FTLE scalar field and convergence zones (c). Colors in (a) and (b) correspond to the departure longitudes and latitudes, respectively, of trajectories arriving on the ERA5 grid on 24 January 2020 at 18 UTC after advection by $\boldsymbol{V}_{\rho_v}$ for 2 days. Blue shades in (c) correspond to the 2-day FTLE (Eq. 2.4) and red lines correspond to height ridges, i.e., attracting LCSs. This day corresponds to the peak activity of an SACZ event.

the strain-tensor C used to compute the FTLE scalar field in Fig. 2.4c. Filaments of high FTLE are immediately evident by visual inspection; ridges corresponding to attracting LCSs are highlighted in red.

The inspection of attracting LCSs and the flow-map components in Figure 2.4 indicate that convergence zones represent interfaces of initially separated air masses. These interfaces can be visualized as sharp gradients of departure latitudes and longitudes. We highlight the sharp diagonal gradient in Fig. 2.4b across Brazil: parcels that originated in equatorial latitudes seem to face a transport barrier at about 10^oS; they are deflected east instead of proceeding to southern parts of the continent as they would in the climatological SAMS flow (Fig. 2.2). This suggests that such structures control the exchanges of moisture between the Amazon and Southeast/South South America. In the next section we will examine this SACZ event in more detail and discuss how the LCSs relate with rainfall and moisture distribution.

2.5 LCSs, moisture and rainfall in a recent SACZ event

Attracting LCSs are structures that shape the evolution of passive tracers in time dependent flows. Atmospheric moisture, however, is not a passive tracer, nor it is homogeneously distributed in the initial times of integration. Therefore, it is not guaranteed that flow entities such as attracting LCSs will shape moisture or rainfall in any meaningful way. In other words, the horizontal distribution of atmospheric moisture could be simply dominated by local sources and sinks. We

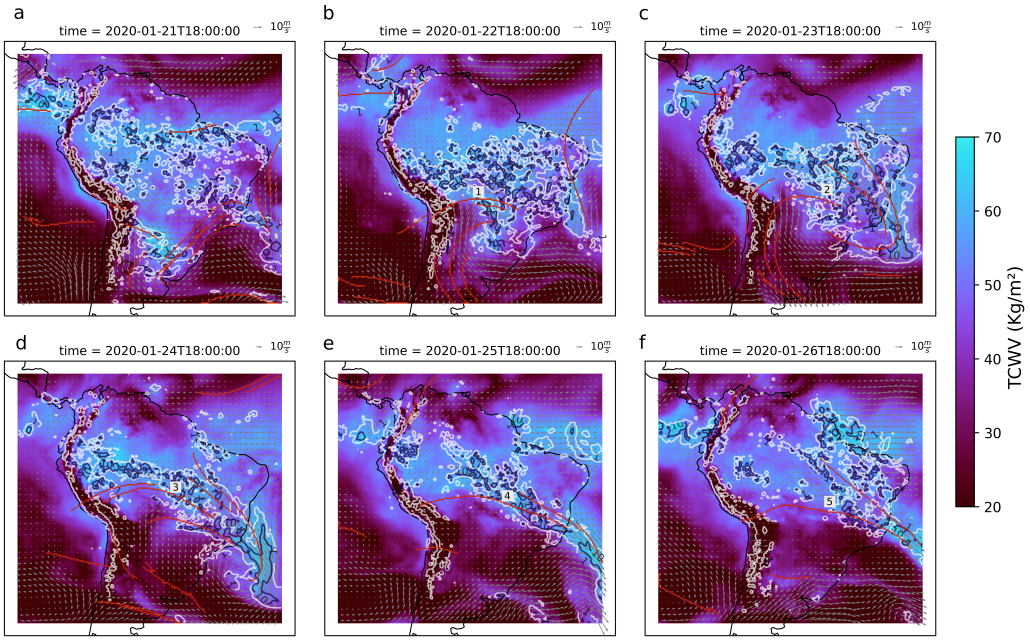

Figure 2.5: Rainfall (contours of 1, 5 and 10 mm/h), vectors of $\boldsymbol{V}_{\rho_v}$ and attracting LCSs (red lines) computed as ridges of the FTLE scalar field given by Eq. 2.4. Time labels are in UTC.

know, however, from a climatological perspective, that advection is important for the global hydrological cycle (Trenberth 1999; Demory et al. 2014). In this section we explore the interplay of attracting LCSs, moisture and rainfall in a recent and significant SACZ event.

Figure 2.5 shows the evolution of attracting LCSs, total column water vapour, $\boldsymbol{V}_{\rho_v}$ and rainfall during an SACZ event in January 2020. In Fig. 2.5a, the SACZ is not yet formed and water vapour is roughly uniformly distributed around the continent. In the equatorial Atlantic, rainfall and moisture are closely aligned along an attracting LCS revealing the Atlantic ITCZ. In the South Atlantic (bottom-right corner of Fig. 2.5a), LCSs appear near rainfall a cyclonic circulation. During the next day (Fig. 2.5b), an attracting LCS appears in western/central Brazil (Label 1) as an interface along which northward flux from southern South America meets

southward flux from the Amazon; they are both deflected east. This interface, identified by the LCS, appears to behave as a transport barrier to the climatological southward Amazonian moisture flux (Figure 2.2) that supplies moisture to southern South America. In fact, this barrier (Labels 1 to 5 in Figs. 2.5b to 2.5f) persists as total column water vapour remains low in southern South America.

However, the LCSs in this case study are perhaps most evidently associated with the organisation of moisture and rainfall along a well defined convergence zone. By definition, these LCSs are the locally strongest attracting structures; therefore, we expect that they are the cause of the well-organised rainfall bands in Figures 2.5d, e and f. The initial situation of uniformly distributed moisture in Fig. 2.5a and scattered rainfall evolves into a situation where moisture and rainfall are narrowly distributed along attracting LCSs (Figs. 2.5d, e and f), forming a single diagonal band across the continent. The whole entity, which we may call the SACZ, stems from a favorable configuration of the large-scale mixing depicted by an ensemble of attracting LCSs. The attracting LCSs, in their turn, arise from large-scale stirring, caused by the motion of a cyclone.

Convergence features such as the SACZ are responsible for intraseasonal rainfall variability in South America and, in their turn, are subject to seasonal and interannual variations (Carvalho et al. 2004; Muza et al. 2009). In the following sections we provide a long-term analysis of the seasonal occurrence of LCSs in South America as well as their impact on intraseasonal rainfall and moisture flux variability.

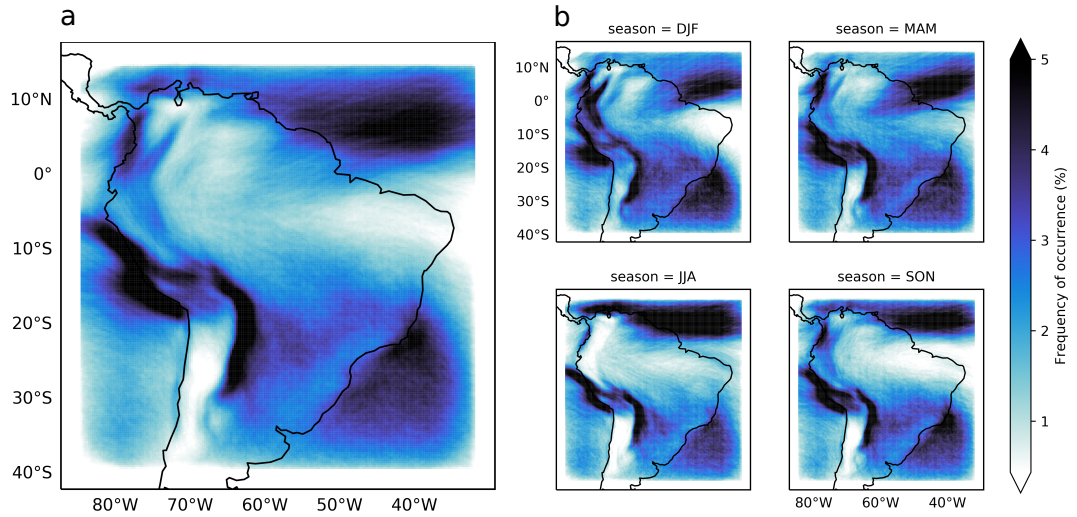

Figure 2.6: Annual (a) and seasonal (b) average frequency of occurrence of convergence zones defined as attracting LCSs between 1980 and 2009. Frequency of occurrence represents the number of LCS events in a grid box divided by the number of samples.

2.6 Climatology and impact on rainfall and moisture

2.6.1 Frequency of occurrence

The annual and seasonal frequencies of occurrence of convergence zones defined as attracting LCS are shown in Figure 2.6. Here the frequency of occurrence is computed as the number of LCS events in a grid box divided by the total number of time steps. A local maximum in the tropical Atlantic coincides with the climatological position of the ITCZ; its frequency increases in austral winter consistent with the increase of rainfall in the ITCZ (Custodio et al. 2017). Between 10^oS and 30^oS at 60^oW, there is a band of higher frequencies along the eastern side of the Andes in all seasons, coinciding with the SALLJ position (Montini et al. 2019). In austral summer, the frequency of convergence zones increases in

Southeast Brazil and South Atlantic near the climatological SACZ position. The local frequency maximum in South Atlantic (approx. 20^oS - 40^oW) is somewhat oriented along the coast. This could result from the interactions of the large-scale flow, sea-breezes and coastal mountain ranges (Fig. 2.1), which contribute substantially to the wind and rainfall regimes in that region (Silva Dias et al. 1995; Perez and Silva Dias 2017).

Given that LCSs frequent regions that coincide with the aforementioned rainfall mechanisms, we expect large-scale mixing to be playing a role in intensifying or generating these rainfall and moisture features such as the ITCZ or the SACZ. In the next section we quantify the local linear influence of mixing as measured by the FTLE on moisture and rainfall.

2.6.2 Correlation between the FTLE and rainfall

In this section we investigate how the FTLE correlates with rainfall and water vapour at grid-point scale during austral summer and winter. Since these are Eulerian quantities, a degree of care must be taken when interpreting these correlations. From the moisture budget, changes in the moisture content and rainfall are associated with moisture advection, mass convergence and evaporation in the immediate neighborhood of the atmospheric column considered. The FTLE is a Lagrangian quantity representing the average deformation of arriving trajectories. It is only directly associated with Eulerian mass convergence in slowly varying or steady flows, where the Lagrangian strain can be approximated by the Eulerian strain (Ottino 1989). Nevertheless, correlating the FTLE with rainfall and moisture is a simple way to quantify their dependence on mixing. Garaboa-Paz

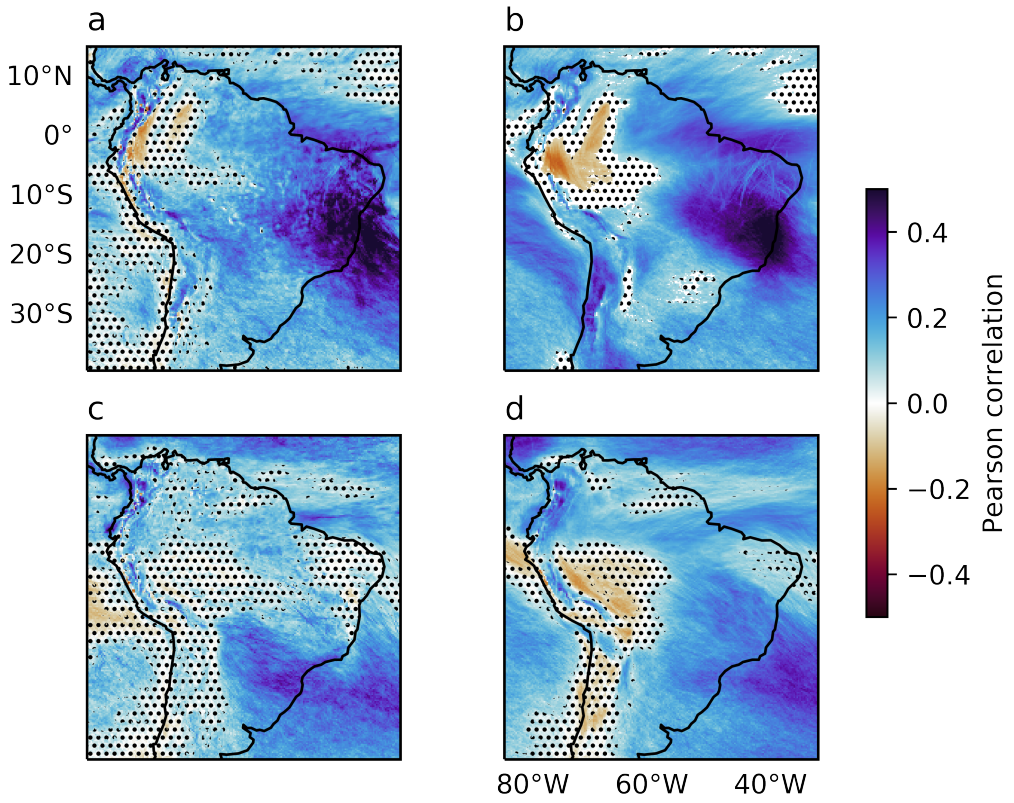

Figure 2.7: Pearson's correlation coefficient between the FTLE and: rainfall (a, c) and total column water vapour (b, d) in DJF (a, b) and JJA (c, d). Correlations were computed in 6-hourly data. Stippled regions are inside the 99% confidence interval for the null-hypothesis of zero correlation.

et al. 2017 have similarly correlated the FTLE with other atmospheric variables such as the Eady growth to identify the dependence of atmospheric rivers on the mixing variability.

Figure 2.7 shows the Pearson's correlation coefficient between the FTLE, rainfall and total column water vapour at 2-day intervals in summer and winter. The 99% confidence interval was calculated for the null hypothesis of zero correlation. Significant correlations are seen throughout most of the domain, indicating that the moisture content and rainfall in most regions are related, to some degree, to large-scale mixing. Two features of positive correlations are prominent in summer in Figs. 2.7a and 2.7b: a maximum in southeastern/central Brazil and a zonal band in equatorial northern/northeastern Brazil. Rainfall in these regions is directly influenced by the ITCZ and SACZ (Uvo et al. 1998; Ambrizzi and Ferraz 2015). Negative correlations with total column water vapour in summer can be seen in western Amazon (approx. 5^oS, 70^oW), indicating that the rainfall and moisture content rely on local sources or non-mixed (parallel trajectories) transport. In winter (Figs. 2.7c and 2.7d), the FTLE is positively correlated with rainfall in South Brazil; Paraguay and Uruguay are the most correlated with rainfall, while the storm-track in the South Atlantic is where the positive correlation of FTLE with total column water vapour is highest.

While the FTLE scalar field presents significant grid-point correlations with rainfall and moisture, we expect that distinct features of large-scale mixing also influence these variables in the surroundings. For example, in the case study in Section 2.5 we have seen that LCSs intensified the moisture gradients and organised a continental scale rainfall band. In the next section we investigate this regional impact of LCSs in intraseasonal variability by the composite analysis of LCS events

on key regions in South and Southeast Brazil.

2.6.3 Moisture flux and rainfall anomalies in the SACZ and the SALLJ regions

To investigate how the location of attracting LCSs influences rainfall and moisture transport variability, we focus on two watersheds that are tributaries of the La Plata River: Tietê and Uruguay. These basins were chosen because they are typically influenced by two of the mechanisms of interest: the SACZ in Tietê and the SALLJ in Uruguay. Economic activity in both watersheds depend on rainfall particularly due to hydroelectric power generation and agriculture. Moreover, a number of densely populated cities, including São Paulo, are located in the Tietê catchment area.

Figure 2.8 shows the anomalies of rainfall and vertically integrated moisture flux in summer and winter during events of attracting LCSs over the Tietê and Uruguay watersheds. The events were selected when LCSs intersected the watershed areas. In summer in the Tietê basin (Fig. 2.8a), attracting LCS events are associated with a significant anomalous rainfall dipole and cyclonic moisture flux. North of the basin, positive rainfall anomalies form a diagonal band extending from central Brazil to the South Atlantic; to the south, there is a negative rainfall anomaly. Similar anomalies were associated with the SACZ by Muza et al. 2009. A northward anomalous flux along the Andes indicates a weaker SALLJ during attracting LCS events in Tietê. This is also noticed in winter (Fig. 2.8b), although the positive rainfall anomalies are weaker and the cyclonic anomaly is centered in the South Atlantic. The SALLJ weakening could produce the significant negative

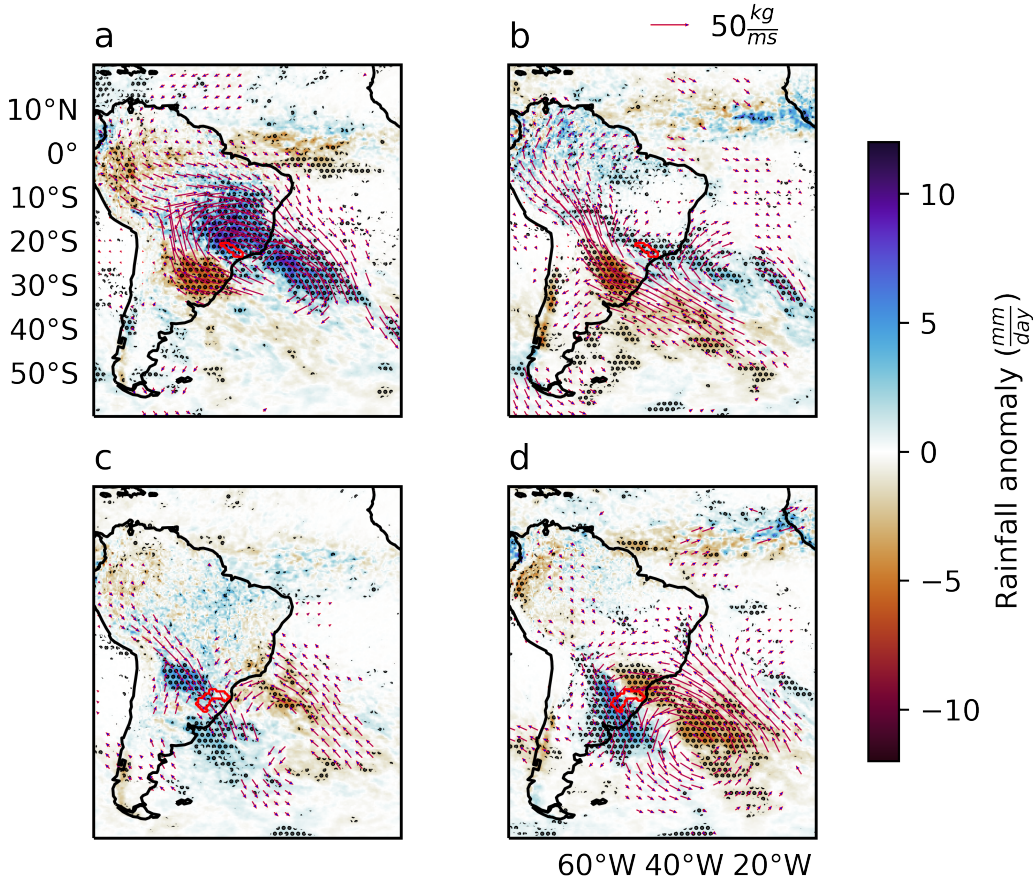

Figure 2.8: Anomalies of rainfall and vertically integrated moisture flux (vectors) during attracting LCS events in the Tietê (a, b) and Uruguay (c, d) basins in DJF (a, c) and JJA (b, d). Anomalies significant at the 99% confidence level are stippled. The watershed boundaries are represented by red polygons.

rainfall anomalies near South Brazil and Paraguay. This interplay between the SACZ and SALLJ is a documented feature of the South American climate (Boers et al. 2014).

During LCS events in the Uruguay basin (Figs. 2.8c and 2.8d), there is an anti-cyclonic moisture flux anomaly in the South Atlantic associated with a southward flux along the Andes, indicating stronger SALLJ. The rainfall anomalies are positive near South Brazil, Uruguay and Paraguay. Liebmann et al. 2004 found similar rainfall anomalies of about 4 mm/day in the vicinity of the Uruguay basin during strong SALLJ events.

The consistency of the anomalies in Figure 2.8 with previous studies about the SACZ and SALLJ highlights the potential of the methodology to identify important mechanisms of moisture transport. Moreover, it indicates that the SACZ and the SALLJ, from a kinematical point of view, are similar coherent structures stemming from large-scale mixing. This raises a question about the dynamical mechanisms that create these kinematical features. Both the SACZ and the SALLJ have been associated with teleconnection patterns across the Pacific, thus, in the next section we verify if LCS events in the Tietê and Uruguay basins are associated with similar dynamical settings.

2.6.4 Dynamical mechanisms of LCS in the SACZ and the SALLJ regions

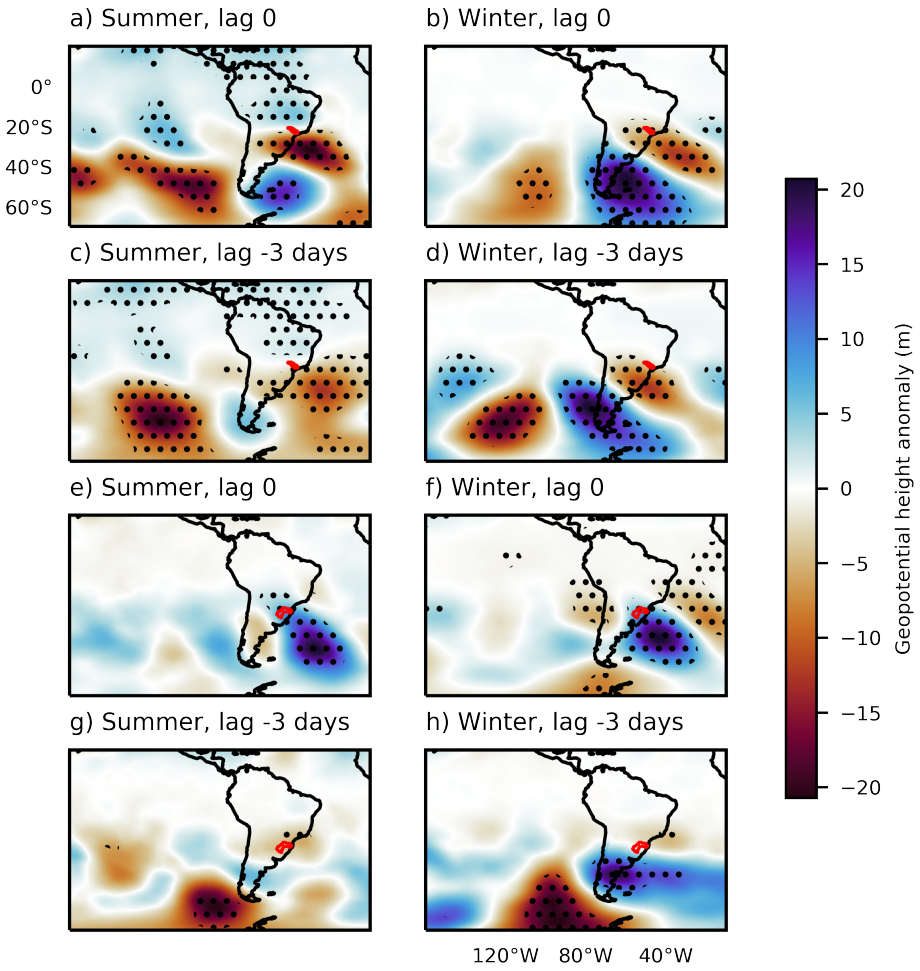

Figure 2.9: Geopotential height anomalies at 250 hPa during attracting LCS events in the Tietê (a, b, c and d) and Uruguay basins (e, f, g and h) during the austral summer (DJF) and winter (JJA) for lags 0 and -3 days. Anomalies significant at the 99% confidence interval are stippled. Red polygons represent the watershed boundaries.

Figure 2.9 shows the geopotential anomalies at 250 hPa in summer and winter during LCS events in the Tietê and Uruguay basins. During events in Tietê in summer (Figs. 2.9a and 2.9c), an anomalous trough is positioned south of the

watershed roughly aligned with the cyclonic circulation in Figure 2.8a. This trough is connected with a wave pattern that appears to propagate from the South Pacific (Fig. 2.9c). This observation is consistent with the mechanism of SACZ formation proposed by Van Der Wiel et al. 2015 based on ray-tracing diagnostics of Rossby waves initiated by a heat source in the same location. Anomalous convective activity in the West Pacific and a pulse of the Madden-Julian Oscillation have also been reported to create similar wavetrain patterns (Cunningham et al. 2006; Grimm 2019).

In winter in Tietê (Fig. 2.9b and 2.9d), a wave pattern arises similar to the PSA teleconnection (Ambrizzi et al. 1995), positioning a trough south of the Tietê watershed. This trough is slightly to the east (downstream) of the anomalous low-level circulation in Figure 2.8b, indicating baroclinicity. This type of configuration has been noted as a cyclogenesis mechanism in Southeast and South Brazil (Crespo et al. 2021). During LCS events in the Uruguay basin in both seasons (Figs. 2.9e and 2.9f), an anomalous 250 hPa ridge is positioned in the South Atlantic, aligned with the anti-cyclonic circulation in Figures 2.8c and d. The lagged anomalies (Figs. 2.8g and 2.8h) indicate that this ridge originates from a perturbation in higher latitudes.

These geopotential anomalies associated with LCS events indicate that large-scale dynamical mechanisms are providing a favorable kinematical configuration for the development of LCSs and the further organisation of moisture and rainfall in bands. This is consistent with the discussion in Shepherd et al. 2000 that increased Rossby wave activity changes the kinetic energy spectrum such that coherent structures of tracer accumulation are more likely to appear.

2.7 Summary and conclusions

This is the first study to investigate the role of Lagrangian Coherent Structures (LCSs) in tropical and subtropical rainfall. We defined skeletons of atmospheric convergence zones as attracting LCSs given by ridges of the Finite-Time Lyapunov Exponent (FTLE). The FTLE is a measure of deformation among neighboring trajectories that synthesizes the state of mixing in fixed time intervals and allows the visualization of transport barriers. Defining convergence zones as attracting LCSs is consistent with a Lagrangian understanding of convergence zones as regions where remotely sourced air masses interact (Simpson 1947). This definition also implies that convergence zone skeletons are associated with tracer accumulation, potentially explaining the organization of cloud and rainfall bands.

Attracting LCSs frequent tropical and subtropical South America, with climatologies consistent with previous studies of large-scale phenomena such as the Intertropical Convergence Zone, the South Atlantic Convergence Zone (SACZ) and the South American Low-Level Jet (SALLJ). Point by point correlations showed that, in the typical areas of action of these mechanisms, moisture and rainfall depend to some extent on the large-scale mixing represented by the FTLE scalar field.

Fixing locations of interest in watersheds in South and Southeast Brazil, we showed that significant rainfall and moisture flux anomalies are associated with attracting LCS events. These anomalies are consistent with previous climatologies (e.g., Boers et al. 2014) of the SACZ and the SALLJ. We also analysed geopotential anomalies at 250 hPa during LCS events in these two basins. The geopotential composites suggest that remotely sourced perturbations are stirring the low-level

synoptic-scale flow such that attracting LCSs arise and organise the moisture transport and rainfall in fine bands. This behaviour resembles the spectrally non-local regime in the stratosphere, where the evolution of tracer features is set by low wavenumber perturbations (Shepherd et al. 2000).

In the case of the SACZ, our approach differs substantially from existing classifications that equate the SACZ to patterns associated with convective or rainfall variability (Carvalho et al. 2004; Ambrizzi and Ferraz 2015). Our approach first asserts the existence of coherent flow features organising atmospheric moisture. Only then do we associate them with rainfall variability. Because of that, the approach is general and may be applied in other locations to identify similar structures. Nonetheless, our results are consistent with the current understanding of the main features of the SAMS (Marengo et al. 2012), supporting that the methodology can be employed as a detection criterion for these features, particularly the SACZ. Such objective classification of convergence zone skeletons could assist operational weather forecasters in identifying these weather systems. By considering the mean FTLE along an LCS, the forecaster could estimate their potential to intensify moisture gradients, thus anticipating the development of rain bands or moisture channels.

For future developments, we suggest refining the classification by allowing different types of convergence zones. This could be done by analysing physical quantities across and along the attracting LCSs. For example, if the temperature gradient is strong perpendicular to the FTLE ridge, such convergence zone could be associated with a frontal system. Similarly, a convergence zone could be associated with orography if the LCS is parallel to elevation features. Alternatively, convergence zones could be filtered by properties of the arriving parcels, such

as temperature and water vapour concentration, likewise the trajectory filtering available in LAGRANTO (Sprenger and Wernli 2015). This refined classification would help understanding the mechanisms that generate the LCSs and, ultimately, organised rainfall bands. As a final goal, the proposed framework could serve as basis for a global criterion for convergence zones, replacing or being combined with region-specific classification methods.

References

Allshouse, Michael R, and Thomas Peacock. 2015. "Refining finite-time Lyapunov exponent ridges and the challenges of classifying them". *Chaos: An Interdisciplinary Journal of Nonlinear Science* 25 (8): 087410.

Alpert, Leo. 1945. "The intertropical convergence zone of the eastern Pacific region (I)". *Bulletin of the American Meteorological Society* 26 (10): 426–432.

Ambrizzi, Tércio, and Simone ET Ferraz. 2015. "An objective criterion for determining the South Atlantic Convergence Zone". *Frontiers in Environmental Science* 3:23.

Ambrizzi, Tercio, Brian J Hoskins, and Huang-Hsiung Hsu. 1995. "Rossby wave propagation and teleconnection patterns in the austral winter". *Journal of the Atmospheric Sciences* 52 (21): 3661–3672.

Aref, Hassan. 1984. "Stirring by chaotic advection". *Journal of fluid mechanics* 143:1–21.

Arraut, Josefina Moraes, et al. 2012. "Aerial rivers and lakes: looking at large-scale moisture transport and its relation to Amazonia and to subtropical rainfall in South America". *Journal of Climate* 25 (2): 543–556.

Barros, Vicente, et al. 2000. "Influence of the South Atlantic convergence zone and South Atlantic Sea surface temperature on interannual summerrainfall variability in Southeastern South America". *Theoretical and Applied Climatology* 67 (3-4): 123–133.

Beron-Vera, Francisco J, et al. 2012. "Zonal jets as meridional transport barriers in the subtropical and polar lower stratosphere". *Journal of the Atmospheric Sciences* 69 (2): 753–767.

Berry, Gareth, and Michael J Reeder. 2014. "Objective identification of the intertropical convergence zone: Climatology and trends from the ERA-Interim". *Journal of Climate* 27 (5): 1894–1909.

Boers, Niklas, et al. 2014. "The South American rainfall dipole: A complex network analysis of extreme events". *Geophysical Research Letters* 41 (20): 7397–7405.

Boffetta, Guido, et al. 2001. "Detecting barriers to transport: a review of different techniques". *Physica D: Nonlinear Phenomena* 159 (1-2): 58–70.

Bowman, Kenneth P. 1999. "Manifold geometry and mixing in observed atmospheric flows". *preprint*.

Carvalho, Leila MV, Charles Jones, and Brant Liebmann. 2004. "The South Atlantic convergence zone: Intensity, form, persistence, and relationships with intraseasonal to interannual activity and extreme rainfall". *Journal of Climate* 17 (1): 88–108.

CPTEC. 2020. "Synoptic synthesis January 2020". Visited on 10/02/2020. `https://s1.cptec.inpe.br/admingpt/tempo/pdf/sintese_mensal_012020%20%5C[Modo%5C%20de%5C%20Compatibilidade%5C].pdf`.

Crespo, Natália Machado, et al. 2021. "A potential vorticity perspective on cyclogenesis over centre-eastern South America". *International Journal of Climatology* 41 (1): 663–678.

Cunningham, Castro, Christopher Alexander, and Iracema Fonseca de Albuquerque Cavalcanti. 2006. "Intraseasonal modes of variability affecting the South Atlantic Convergence Zone". *International Journal of Climatology: A Journal of the Royal Meteorological Society* 26 (9): 1165–1180.

Custodio, Maria de Souza, et al. 2017. "Impact of increased horizontal resolution in coupled and atmosphere-only models of the HadGEM1 family upon the climate patterns of South America". *Climate Dynamics* 48 (9): 3341–3364.

d'Ovidio, Francesco, et al. 2009. "Comparison between Eulerian diagnostics and finite-size Lyapunov exponents computed from altimetry in the Algerian basin". *Deep Sea Research Part I: Oceanographic Research Papers* 56 (1): 15–31.

Dacre, Helen F, et al. 2015. "How do atmospheric rivers form?" *Bulletin of the American Meteorological Society* 96 (8): 1243–1255.

Demory, Marie-Estelle, et al. 2014. "The role of horizontal resolution in simulating drivers of the global hydrological cycle". *Climate Dynamics* 42 (7-8): 2201–2225.

Dierckx, Paul. 1995. *Curve and surface fitting with splines*. Oxford University Press.

Dommenget, Dietmar, and Mojib Latif. 2002. "A cautionary note on the interpretation of EOFs". *Journal of Climate* 15 (2): 216–225.

Farazmand, Mohammad, Daniel Blazevski, and George Haller. 2014. "Shearless transport barriers in unsteady two-dimensional flows and maps". *Physica D: Nonlinear Phenomena* 278:44–57.

Fletcher, Robert D. 1945. "The general circulation of the tropical and equatorial atmosphere". *Journal of Meteorology* 2 (3): 167–174.

Fulton, James, and Gabriele Hegerl. 2019. "Reliable pattern extraction for climate data". *9th International Workshop on Climate Informatics*.

Garaboa-Paz, Daniel, Jorge Eiras-Barca, and Vicente Pérez-Muñuzuri. 2017. "Climatology of Lyapunov exponents: the link between atmospheric rivers and large-scale mixing variability". *Earth System Dynamics* 8 (3): 865–873.

Garaboa-Paz, Daniel, et al. 2015. "Lagrangian coherent structures along atmospheric rivers". *Chaos: An Interdisciplinary Journal of Nonlinear Science* 25 (6): 063105.

Gimeno, Luis, et al. 2016. "Major mechanisms of atmospheric moisture transport and their role in extreme precipitation events". *Annual Review of Environment and Resources* 41:117–141.

Grimm, Alice M. 2019. "Madden–Julian Oscillation impacts on South American summer monsoon season: precipitation anomalies, extreme events, teleconnections, and role in the MJO cycle". *Climate Dynamics* 53 (1): 907–932.

Guo, Hanqi, et al. 2016. "Finite-time lyapunov exponents and lagrangian coherent structures in uncertain unsteady flows". *IEEE transactions on visualization and computer graphics* 22 (6): 1672–1682.

Haller, George. 2011. "A variational theory of hyperbolic Lagrangian coherent structures". *Physica D: Nonlinear Phenomena* 240 (7): 574–598.

— . 2001. "Distinguished material surfaces and coherent structures in three-dimensional fluid flows". *Physica D: Nonlinear Phenomena* 149 (4): 248–277.

— . 2015. "Lagrangian coherent structures". *Annu. Rev. Fluid Mech* 47 (1): 137–162.

Haller, George, and Francisco J Beron-Vera. 2012. "Geodesic theory of transport barriers in two-dimensional flows". *Physica D: Nonlinear Phenomena* 241 (20): 1680–1702.

Haller, George, and Guocheng Yuan. 2000. "Lagrangian coherent structures and mixing in two-dimensional turbulence". *Physica D: Nonlinear Phenomena* 147 (3-4): 352–370.

Hortal, Mariano. 2002. "The development and testing of a new two-time-level semi-Lagrangian scheme (SETTLS) in the ECMWF forecast model". *Quarterly Journal of the Royal Meteorological Society: A journal of the atmospheric sciences, applied meteorology and physical oceanography* 128 (583): 1671–1687.

Insel, Nadja, Christopher J Poulsen, and Todd A Ehlers. 2010. "Influence of the Andes Mountains on South American moisture transport, convection, and precipitation". *Climate Dynamics* 35 (7-8): 1477–1492.

Jorgetti, Tatiana, Pedro Leite da Silva Dias, and Edmilson Dias de Freitas. 2014. "The relationship between South Atlantic SST and SACZ intensity and positioning". *Climate Dynamics* 42 (11-12): 3077–3086.

Lanfredi, Isaque Saes, and Ricardo de Camargo. 2018. "Classification of Extreme Cold Incursions over South America". *Weather and Forecasting* 33 (5): 1183–1203.

Lekien, Francois, and Shane D Ross. 2010. "The computation of finite-time Lyapunov exponents on unstructured meshes and for non-Euclidean manifolds". *Chaos: An Interdisciplinary Journal of Nonlinear Science* 20 (1): 017505.

Lenters, JD, and Kerry Harrison Cook. 1999. "Summertime precipitation variability over South America: Role of the large-scale circulation". *Monthly Weather Review* 127 (3): 409–431.

Liebmann, Brant, et al. 2004. "Subseasonal variations of rainfall in South America in the vicinity of the low-level jet east of the Andes and comparison to those in the South Atlantic Convergence Zone". *Journal of Climate* 17 (19): 3829–3842.

Marengo, JA, et al. 2012. "Recent developments on the South American monsoon system". *International Journal of Climatology* 32 (1): 1–21.

Mendes, David, et al. 2010. "Climatology of extratropical cyclones over the South American–southern oceans sector". *Theoretical and Applied Climatology* 100 (3-4): 239–250.

Mo, Kingtse C, and Julia N Paegle. 2001. "The Pacific–South American modes and their downstream effects". *International Journal of Climatology: A Journal of the Royal Meteorological Society* 21 (10): 1211–1229.

Monahan, Adam H, et al. 2009. "Empirical orthogonal functions: The medium is the message". *Journal of Climate* 22 (24): 6501–6514.

Montini, Tessa L, Charles Jones, and Leila MV Carvalho. 2019. "The South American low-level jet: a new climatology, variability, and changes". *Journal of Geophysical Research: Atmospheres* 124 (3): 1200–1218.

Muza, Michel N, et al. 2009. "Intraseasonal and interannual variability of extreme dry and wet events over southeastern South America and the subtropical Atlantic during austral summer". *Journal of Climate* 22 (7): 1682–1699.

Nieto, Rosana Ferreira, and Winston C Chao. 2013. "Aqua-planet simulations of the formation of the South Atlantic Convergence Zone". *International Journal of Climatology* 33 (3): 615–628.

Olascoaga, Maria J, et al. 2006. "Persistent transport barrier on the West Florida Shelf". *Geophysical Research Letters* 33 (22).

Ottino, Julio M. 1989. *The kinematics of mixing: stretching, chaos, and transport*. Vol. 3. Cambridge university press.

Peikert, Ronald, David Günther, and Tino Weinkauf. 2013. "Comment on "Second derivative ridges are straight lines and the implications for computing Lagrangian Coherent Structures, Physica D 2012.05. 006"". *Physica D: Nonlinear Phenomena* 242 (1): 65–66.

Peikert, Ronald, and Filip Sadlo. 2008. "Height ridge computation and filtering for visualization". In *2008 IEEE Pacific Visualization Symposium*, 119–126. IEEE.

Perez, Gabriel MP, and Maria AF Silva Dias. 2017. "Long-term study of the occurrence and time of passage of sea breeze in São Paulo, 1960–2009". *International Journal of Climatology* 37 (S1): 1210–1220.

Pierrehumbert, Richard T, and Hong Yang. 1993. "Global chaotic mixing on isentropic surfaces". *Journal of the Atmospheric Sciences* 50 (15): 2462–2480.

Pierrehumbert, RT. 1991. "Large-scale horizontal mixing in planetary atmospheres". *Physics of Fluids A: Fluid Dynamics* 3 (5): 1250–1260.

Poveda, Germán, Liliana Jaramillo, and Luisa F Vallejo. 2014. "Seasonal precipitation patterns along pathways of South American low-level jets and aerial rivers". *Water Resources Research* 50 (1): 98–118.

Raupp, Carlos FM, and Pedro L Silva Dias. 2010. "Interaction of equatorial waves through resonance with the diurnal cycle of tropical heating". *Tellus A: Dynamic Meteorology and Oceanography* 62 (5): 706–718.

Ruiz-Vásquez, Melissa, et al. 2020. "Effects of Amazon basin deforestation on regional atmospheric circulation and water vapor transport towards tropical South America". *Climate Dynamics* 54 (9): 4169–4189.

Rutherford, Blake, Gerhard Dangelmayr, and Michael T Montgomery. 2011. *Lagrangian coherent structures in tropical cyclone intensification.* Tech. rep. Naval Postgraduate School Monterey CA. Dept. of Meteorology.

Shadden, Shawn C, Francois Lekien, and Jerrold E Marsden. 2005. "Definition and properties of Lagrangian coherent structures from finite-time Lyapunov exponents in two-dimensional aperiodic flows". *Physica D: Nonlinear Phenomena* 212 (3-4): 271–304.

Shepherd, Theodore G, John N Koshyk, and Keith Ngan. 2000. "On the nature of large-scale mixing in the stratosphere and mesosphere". *Journal of Geophysical Research: Atmospheres* 105 (D10): 12433–12446.

Silva Dias, Maria AF, Pier Luigi Vidale, and Cintia MR Blanco. 1995. "Case study and numerical simulation of the summer regional circulation in São Paulo, Brazil". *Boundary-Layer Meteorology* 74 (4): 371–388.

Simpson, Robert H. 1947. "Synoptic aspects of the intertropical convergence near Central and South America". *Bulletin of the American Meteorological Society* 28 (7): 335–346.

Sprenger, Michael, and Heini Wernli. 2015. "The LAGRANTO Lagrangian analysis tool–version 2.0". *Geoscientific Model Development* 8 (8): 2569–2586.

Trenberth, Kevin E. 1999. "Atmospheric moisture recycling: Role of advection and local evaporation". *Journal of Climate* 12 (5): 1368–1381.

Uvo, Cintia Bertacchi, et al. 1998. "The relationships between tropical Pacific and Atlantic SST and northeast Brazil monthly precipitation". *Journal of Climate* 11 (4): 551–562.

Van Der Wiel, Karin, et al. 2015. "A dynamical framework for the origin of the diagonal South Pacific and South Atlantic convergence zones". *Quarterly Journal of the Royal Meteorological Society* 141 (691): 1997–2010.

Vera, Carolina S, Paula K Vigliarolo, and Ernesto Hugo Berbery. 2002. "Cold season synoptic-scale waves over subtropical South America". *Monthly Weather Review* 130 (3): 684–699.

Vera, Carolina, et al. 2006. "The South American low-level jet experiment". *Bulletin of the American Meteorological Society* 87 (1): 63–78.

Vindel, Jose M, et al. 2020. "Temporal and spatial variability analysis of the solar radiation in a region affected by the intertropical convergence zone". *Meteorological Applications* 27 (1): e1824.

Welander, Pierre. 1955. "Studies on the general development of motion in a two-dimensional, ideal fluid". *Tellus* 7 (2): 141–156.

Weller, Evan, et al. 2017. "Precipitation associated with convergence lines". *Journal of Climate* 30 (9): 3169–3183.

Zemp, DC, et al. 2014. "On the importance of cascading moisture recycling in South America". *Atmospheric Chemistry and Physics* 14 (23): 13337–13359.

Chapter 3

Using a synoptic-scale mixing diagnostic to explain global precipitation variability from weekly to interannual timescales

This is chapter has been accepted in the *Journal of Climate* with the following reference:

Perez, Gabriel M P, Pier Luigi Vidale, Helen Dacre and Jorge Garcia-Franco. 2022. "Using a synoptic-scale mixing diagnostic to explain global precipitation variability from weekly to interannual timescales". *Journal of Climate*, In Press.

Abstract

Precipitation often happens along organised filaments or bands of moisture such as convergence zones. Recent regional studies have shown that these moisture filaments arise from synoptic-scale mixing features known as attracting "Lagrangian Coherent Structures" (LCSs). In this study, we present a climatology of synoptic-scale mixing and investigate its co-variability with precipitation on temporal scales ranging from weekly to interannual. We characterise mixing with the Finite-time Lyapunov Exponent (FTLE), a measure of parcel deformation, in ERA5 reanalysis data between 1980 and 2009. Attracting LCSs are identified as ridges of the FTLE. At the interannual time scale, we compare El Niño and La Niña events and find that composites of precipitation and mixing anomalies share similar spatial patterns. We also compare summer and winter seasons and find that composites of seasonal-mean precipitation and mixing anomalies present similar characteristics; i.e., precipitation is particularly intense (weak) where mixing is strong (weak). In particular, these patterns closely match the typical signatures of the Intertropical Convergence Zone (ITCZ) and monsoon systems and the migrations of extratropical cyclone tracks. At the subseasonal scale, we employ daily composites to investigate the influence of the Madden-Julian Oscillation and the North Atlantic Oscillation on the mixing regimes of the Atlantic and East Pacific; our results indicate that these oscillations control the synoptic-scale horizontal mixing and the occurrence of LCSs as to suppress or enhance precipitating systems like the ITCZ and the South Atlantic Convergence Zone. The results presented in this first climatology of synoptic-scale mixing and LCSs indicate that these are powerful diagnostics

to identify circulation mechanisms underlying precipitation variability.

3.1 Introduction

Water vapour in the Earth's atmosphere is constantly sourced from the surface by evaporation and removed by precipitation. Notable moisture sources are on the sea surface under subtropical anticyclones, while important sinks can be found along the Intertropical Convergence Zone (ITCZ) and over tropical and subtropical landmasses under the action of convergence zones and monsoon systems (Wills and Schneider 2015). The median lifetime of water vapour in the atmosphere is approximately 4 days (Läderach and Sodemann 2016). During their lifetime, moist parcels are deformed by the large-scale flow such that filaments and bands of high moisture concentration arise. These moist bands are often associated with weather events such as convergence zones (Kodama 1992) and atmospheric rivers (Dacre et al. 2015).

The ceaseless process of reshaping the horizontal moisture distribution is Lagrangian in essence, as it depends on the history of air masses during the residence time of water vapour. Although Eulerian horizontal velocity fields can be used to quantify instantaneous or time-averaged convergence (Herdies et al. 2002; Berry and Reeder 2014), they cannot reveal the kinematical structures organising the moisture transport. This is because, in the time dependent atmospheric flow, streamlines and pathlines quickly diverge. Therefore, frameworks that incorporate the Lagrangian nature of mixing are more appropriate to investigate kinematical structures of accumulation of moisture and other tracers whose residence times are comparable or longer than the dominant time-scales of motion (Huntley et

al. 2015; Garaboa-Paz et al. 2017; Perez et al. 2021).

The nature of mixing in a flow can be characterised by the stretching and folding of its fluid parcels (Ottino 1989), a process that determines how tracers and properties are redistributed by advection (Pierrehumbert 1991; Shepherd et al. 2000). During tracer redistribution, distinct structures of high or low concentration may arise around attracting or repelling kinematical skeletons known as Lagrangian Coherent Structures (LCSs)(Haller and Yuan 2000; Shadden et al. 2005). Recent studies in regional domains show that the mathematical framework of mixing offers promising tools to identify atmospheric circulation features associated with precipitation and moisture transport (Garaboa-Paz et al. 2015; Garaboa-Paz et al. 2017; Niang et al. 2020; Perez et al. 2021). However, there are still no global climatologies to support more general discussions and conclusions about the relationships between mixing and precipitation.

In this study, we address two main questions: (1) can we employ the framework of mixing and LCSs to objectively identify converge zones and other structures relevant for regional precipitation regimes, expanding the results of Perez et al. 2021 to a global domain? (2) What is the nature and spatiotemporal scales of the mixing-precipitation relationship? To answer these questions, we present a 30-year global climatology of mixing and LCSs in reanalysis data and discuss the spatial distribution and temporal variability of precipitation in light of this climatology. We investigate interannual, seasonal and subseasonal scales of variability, focusing on the role of general circulation features such as subtropical anticyclones and monsoons in providing a favourable environment for the formation of moisture bands and precipitation.

3.2 Methods and data

3.2.1 Mixing diagnostics: FTLE and LCSs

In order to diagnose mixing in the horizontal atmospheric flow, we first obtain a two-dimensional flow from the scaling of the vertically integrated moisture flux by the total column water vapour ($\boldsymbol{V}_{\rho_v}$, Eq. 3.1). The aim of weighting the horizontal momentum $\boldsymbol{V}_H$ by the water vapour content ρ_v on each level is to construct a horizontal flow that is representative of levels along which the moisture transport is stronger. This 2-D flow is more appropriate to investigate moisture pathways than simply taking a pressure level close to the surface such as 925 or 850 hPa, which could overlap with topography. Alternatively, a more computationally expensive three-dimensional trajectory integration could be performed. However, the two-dimensional $\boldsymbol{V}_{\rho_v}$ is useful to diagnose the horizontal features of moisture accumulation (Garaboa-Paz et al. 2015; Perez et al. 2021).

$$\boldsymbol{V}_{\rho_v} = \frac{\int_0^\infty \rho_v \boldsymbol{V}_H dz}{\int_0^\infty \rho_v dz} \qquad [\text{m s}^{-1}] \tag{3.1}$$

The flow $\boldsymbol{V}_{\rho_v}$ is then spatially smoothed such that only its large-scale components are retained. This is done by calculating the spherical harmonics of the wind field and retaining wavenumbers smaller than 20 (Sardeshmukh and Hoskins 1984). This spatial smoothing is not expected to significantly affect the position of Lagrangian Coherent Structures (LCSs), since displacement errors of Lagrangian features are at least six times smaller than the resolution of the wind field (Methven and Hoskins 1999). The procedure substitutes the smoothed spherical spline interpolation employed in Perez et al. 2021 as it allows a more explicit control on

the spatial scales that are retained.

In time-dependent flows, coherent tracer filaments are expected to emerge due to a process known as chaotic mixing (Aref 1984; Ottino 1989; Lapeyre 2002; Balasuriya et al. 2018; Ghosh et al. 2021). The kinematical skeletons underlining these filaments are referred to as LCSs (Haller and Yuan 2000; Shadden et al. 2005). One way to characterise mixing and identify attracting LCSs in $\boldsymbol{V}_{\rho_v}(t)$ is to compute the backwards Finite-Time Lyapunov Exponent (FTLE) in sliding finite time windows $\Delta t = t_1 - t_0$ with $t_1 > t_0$. The FTLE ($\sigma(x_0)$, Eq. 3.2) measures the average stretching rate experienced by back-trajectories departing from the neighborhood of $\boldsymbol{x_0}$ after being advected in the 2-dimensional wind field $\boldsymbol{V}_{\rho_v}(t)$ for a time interval Δt. The time interval chosen here was 2-days, as this is long enough to allow trajectories to explore large-scale weather systems but it is well within the median residence time of moisture in the atmosphere of 4 days (Läderach and Sodemann 2016).

$$\sigma(\boldsymbol{x_0}) = \frac{1}{|\Delta t|} \ln\left(\sqrt{\lambda_{max}(C)}\right) \tag{3.2}$$

where λ_{max} is the largest eigenvalue of the Cauchy-Green strain tensor (C). Attracting LCSs can be found as ridges of the FTLE. Here we employ a relaxed version of the ridge criteria proposed by Shadden et al. 2005, that seeks for curves that are parallel to FTLE contours and normal to the direction of most negative FTLE curvature. Shadden et al. 2005 argues that such ridges approximate transport barriers, with small perpendicular flux. A more detailed description of the trajectory computation, ridge detection and linear algebra routines can be found in Perez et al. 2021 and are available online (see the "Code availability" section).

Figure 3.1 exemplifies the methodology for a particular day in the 5$^{\text{th}}$ generation of the ECMWF atmospheric reanalysis (ERA5). Figures 3.1a and 3.1b represent the locations of departure, or origin points, of trajectories that arrived at each grid-box. The departure points were found after two days of back-propagation in $\boldsymbol{V}_{\rho_v}$. Figure 3.1c shows the FTLE and the associated LCSs, computed based on the departure points in Figs. 3.1a and 3.1b. Trajectories of air with similar arrival points can originate from a wide range of longitudes (Fig. 3.1a) and latitudes (Fig.3.1b). In regions of strong mixing, there are particularly sharp gradients of origin latitude and longitude, revealing interfaces of air masses. Parcels arriving in regions of sharp gradients are associated with strong stretching in the back-trajectory integration, as revealed by the FTLE ridges (LCSs) in Figure 3.1c. A visual interpretation of parcel stretching around LCSs can be found in Haller 2015. In fact, Cohen and Kreitzberg 1997 employed FTLE ridges to identify airstream boundaries around extratropical cyclones (ETCs) in the North Atlantic.

Figure 3.2 illustrates two examples of the evolution of total column water vapour (TCWV) and precipitation around LCSs identified at the same timestamp (Fig. 3.2a) and 48 hours after (3.2b) the timestamp of Figure 3.1 (15 December 1989). The example in Fig. 3.2a shows a filament of high TCWV aligned with a set of LCSs around a cyclone close to the coast of Europe; precipitation contours closer to the cyclone core also align with the same set of LCSs. After 2 days, in Fig. 3.2c, a second cyclone arises close to northeastern North America. Around this second cyclone, we notice a new set of LCSs whereby contours of high FTLE and precipitation are aligned. The second example, in Figs. 3.2b and 3.2d, shows that contours of precipitation and high TCWV in the South Pacific evolve to become aligned with the LCSs. Both examples illustrate how LCSs resulting from

synoptic-scale mixing in $\boldsymbol{V}_{\rho_v}$ reshape TCWV and precipitation. Such case studies can be combined with the ones in Garaboa-Paz et al. 2015 and Perez et al. 2021 to build the hypothesis that precipitation and synoptic-scale mixing features are related in different regions across the globe.

3.2.2 Precipitation and mixing co-variability

The examples in Figure 3.2 reveal moisture and precipitation bands aligned along LCSs. This is expected due to the role of mixing in shaping gradients of tracers in fluid flows (Ottino 1989; Lapeyre 2002). Recalling that the FTLE was computed in a horizontal and spatially filtered flow ($\boldsymbol{V}_{\rho_v}$, Eq.3.1) based on the 2-day back-trajectories, we are characterising horizontal mixing in the synoptic-scale. In tropical regions, a synoptic-scale enhancement of column moisture has been observed to start two days before precipitation events (Holloway and Neelin 2010). In the extratropics, where parcel saturation typically only happens via adiabatic cooling, horizontal moisture transport may still play a role in determining the intensity of precipitation events, such as when filaments of high TCWV are created by Rossby wave breaking (De Vries 2021).

To assess if this relationship that takes place in synoptic time scales reflects on longer time scales, we compute the monthly averages of the FTLE and precipitation and identify their principal modes of co-variability through the Partial Least Squares (PLS) decomposition. By performing the co-variability analysis on monthly means, we substantially reduce the computational cost of the PLS decomposition at the expense of potentially obscuring the interpretation of causal relationships between mixing and precipitation. The co-variability analysis on

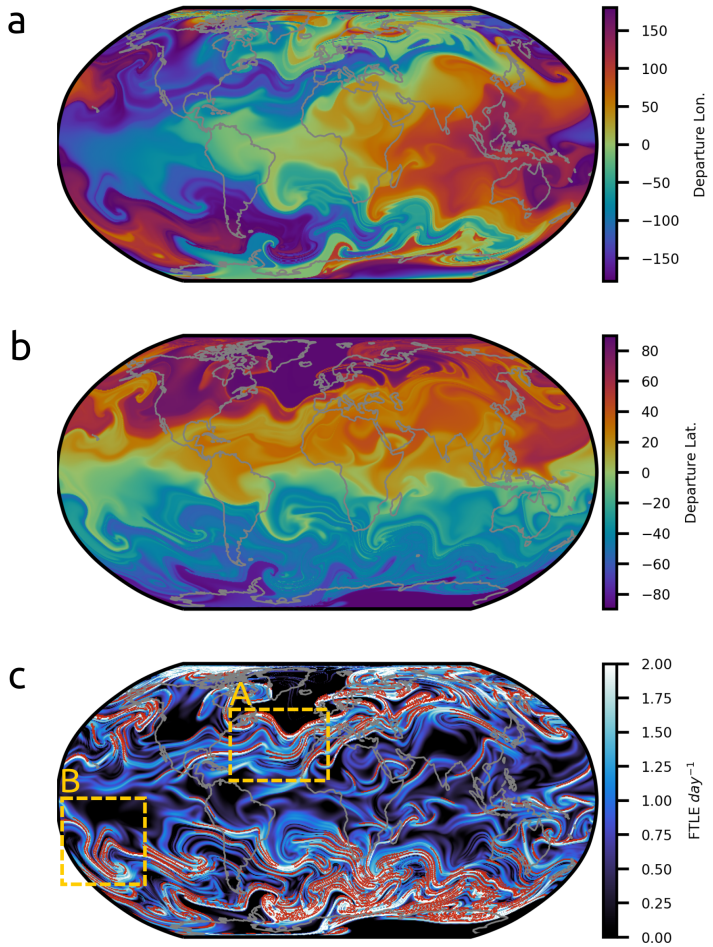

Figure 3.1: Diagnostics of large-scale mixing on $\boldsymbol{V}_{\rho_v}$ on 15 December 1989 using ERA5 data. "a" and "b" show, respectively, the departure longitudes and latitudes of parcels arriving in a regular a 0.5° lat-lon grid after 2 days of backwards advection. Shades of blue in "c" show the FTLE while LCSs are depicted as red filaments. Regions A and B shown in "c" are the spatial domains for the case studies in Figure 3.2

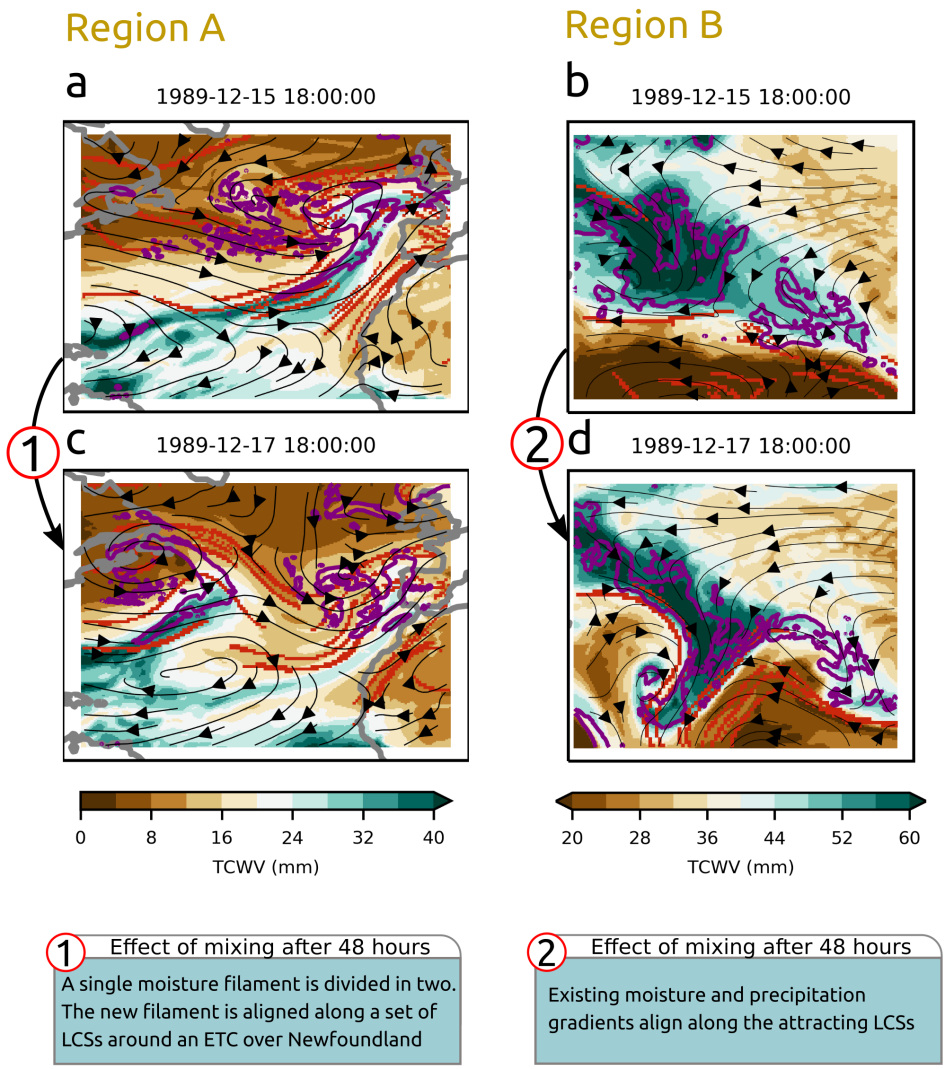

Figure 3.2: Examples of the interaction between total column water vapour (TCWV), precipitation (purple contours denote rates above 2 mm day^{-1}) and LCSs (red filaments) over the North Atlantic ("a" and "c") and South Pacific ("b" and "d"). The spatial domains of Regions A and B are depicted in Figure 3.1c.

monthly means, however, still reveals important circulation mechanisms associated with precipitation anomalies, as shown in the Results section, and in Section 4c we expand the discussion on possible causal pathways.

The PLS finds R pairs of latent variables $\boldsymbol{\xi}_r, \boldsymbol{\omega}_r$, with r in $\{1, 2, ..., R\}$, that maximise the information retained from $X^T Y$ in the least-square sense, where X and Y correspond to 2-dimensional arrays of FTLE and precipitation with latitude/longitude dimensions stacked as columns and time as rows. A description of the PLS algorithm can be found in Wegelin 2000; the author also provides an interesting discussion on how the PLS algorithm relate with canonical correlation analysis.

Considering the uneven area of grid-boxes in a regular lat-lon grid, before applying the PLS method, we multiply X and Y by a weight vector $\boldsymbol{w}$ that is a function of the latitude vector $\boldsymbol{\theta}$: $\boldsymbol{w} = \sqrt{cos(\boldsymbol{\theta})}$. This a standard approach to scale climate data before employing methods based on quadratic covariance matrices (Chung and Nigam 1999; Hawkins and Sutton 2007).

The first pair of latent variables $(\boldsymbol{\xi_1}, \boldsymbol{\omega_1})$ is obtained by finding coefficient vectors $\boldsymbol{u_1}$ and $\boldsymbol{v_1}$ that maximise:

$$\text{Cov}(\boldsymbol{\xi}_1, \boldsymbol{\omega}_1) = \max \text{ Cov}(X\boldsymbol{u_1}, Y\boldsymbol{v_1}) \tag{3.3}$$

Each subsequent pair of latent scores $(\boldsymbol{\xi_r}, \boldsymbol{\omega_r})$ is computed by repeating the procedure on the residual matrices $(X^{(r)}, Y^{(r)})$ obtained by subtracting approximations based on the existing pairs of scores $\{(\boldsymbol{\xi_1}, \boldsymbol{\omega_1})...(\boldsymbol{\xi_r}, \boldsymbol{\omega_r})\}$ from the original matrices (X, Y).

In the case of atmospheric data, $\boldsymbol{u}_r$ and $\boldsymbol{v}_r$ correspond to the spatial patterns,

or modes, that map the pair of latent variables $(\boldsymbol{\xi_r}, \boldsymbol{\omega_r})$ to the original X and Y matrices. After reversing the latitude weighting, these spatial modes are physically interpretable: they are proportional to the covariance between the original variable X or Y and the latent variable of the other (Y or X). Therefore, the spatial modes are presented in the Annex as correlations between one variable (FTLE or precipitation) of each grid point and the latent variable of the other.

By construction, the pairs of latent variables $(\boldsymbol{\xi}_1, \boldsymbol{\omega}_1)$ are maximally correlated; this correlation is close to 1 in the case of the first four modes presented in the Results section. Therefore, for each of the four pairs of modes, we have chosen to discuss only one element of the pair, i.e., the latent scores associated with the FTLE. By taking this viewpoint, we are implicitly addressing the question "what are the FTLE modes that best explain the precipitation variability?". The time series of the precipitation scores are presented in the Annex.

3.3 Results

In this section we present global climatologies and seasonal anomalies of the FTLE and LCS occurrence; these are compared with global climatologies and seasonal anomalies of precipitation and simple diagnostics of general circulation features. All the data employed in this study originates from ERA5 comprising the period between 1980 and 2009. We start with a description of the spatiotemporal variability of large-scale mixing and examine where this variability could be linked with mechanisms of coherent precipitation (e.g. ITCZ) using monthly averaged FTLE, LCS occurrence and precipitation data. We then focus on subseasonal scales and analyse FTLE and LCS composites using daily averaged data to investigate mech-

anisms underpinning changes of precipitation associated with modes of variability such as the Madden-Julian Oscillation (MJO) and the North Atlantic Oscillation (NAO), narrowing the analysis to the Atlantic/Americas sector. Finally, we present meridional overturning anomalies to explain an observed influence of the NAO on South America/South Atlantic precipitation.

3.3.1 Global climatology of large-scale mixing and LCSs

Here we describe general aspects of the global climatologies of mixing, LCSs and precipitation (Fig. 3.3) grouped by latitudinal (Sec. 3.3.1.3.3.1) and longitudinal (Sec. 3.3.1.3.3.1) sectors.

Meridional variability

Extratropical features In the extratropics, we first notice that LCS frequency of occurrence peaks at the mid-latitudes while the FTLE peaks at higher latitudes. We can compare regions north and south of the stars in Figures 2a and 2b. The higher mixing in high latitudes can be explained by the parcel deformation caused by the increased ETC core activity in those regions (Jones and Simmonds 1993; Ulbrich et al. 2009). Cyclone cores, however, are characterised as elliptic LCSs (Haller and Beron-Vera 2012; Haller 2015), while the LCSs identified here as FTLE ridges are expected to identify hyperbolic material lines (Haller 2002); hence the lower frequency of occurrence of LCSs in higher latitudes in Figure 2b. Fronts, on the other hand, can be identified as FTLE ridges (Cohen and Kreitzberg 1997; Garaboa-Paz et al. 2015) and are more frequent at the mid-latitudes (Berry et al. 2011). Therefore, the discrepancies between FTLE intensity and LCS fre-

quency of occurrence in the extratropics can be understood in terms of the spatial distribution of ETC cores and fronts.

Subtropical features In some subtropical regions such as South America, southern North America, South Pacific and East Asia, diagonal FTLE contours and high LCS occurrence (denoted by squares in Figs. 3.3a and b) coincide with precipitation features (Fig. 3.3c), e.g.: South Atlantic Convergence Zone (SACZ) region at $15°S$, $45°W$; Meiyu front region at $20°N$, $140°E$; South Indian Convergence Zone (SICZ) region at ($20°S$, $45°E$) and North America around Mexico and southern United States ($23°N$, $105°W$). These regions are known to be under strong precipitation seasonality driven by convergence zones (Kodama 1992) and monsoon systems (Rodwell and Hoskins 2001); these systems will be further discussed in Section 3.3.3.3.2. We also note that these subtropical FTLE/LCS maxima are typically positioned in-between subtropical anticyclones.

Equatorial features High FTLE and LCS occurrence bands are co-located with the typical position of the ITCZ (triangles in Figures 3.3a and 3.3b). Particularly in the Atlantic and East Pacific, these bands are located between the northern and southern subtropical gyres, revealing the approximation of trajectories associated with the encounter of the southeasterlies and northeasterlies. This suggests that the interface between semi-stationary eddies produces strong deformation. The strong FTLE values (Fig. 3.3a) and frequent occurrence of LCSs (Fig. 3.3b) along the ITCZ suggest that the development of organised precipitation bands is favoured by the large-scale flow kinematics, potentially driving precipitation in those regions.

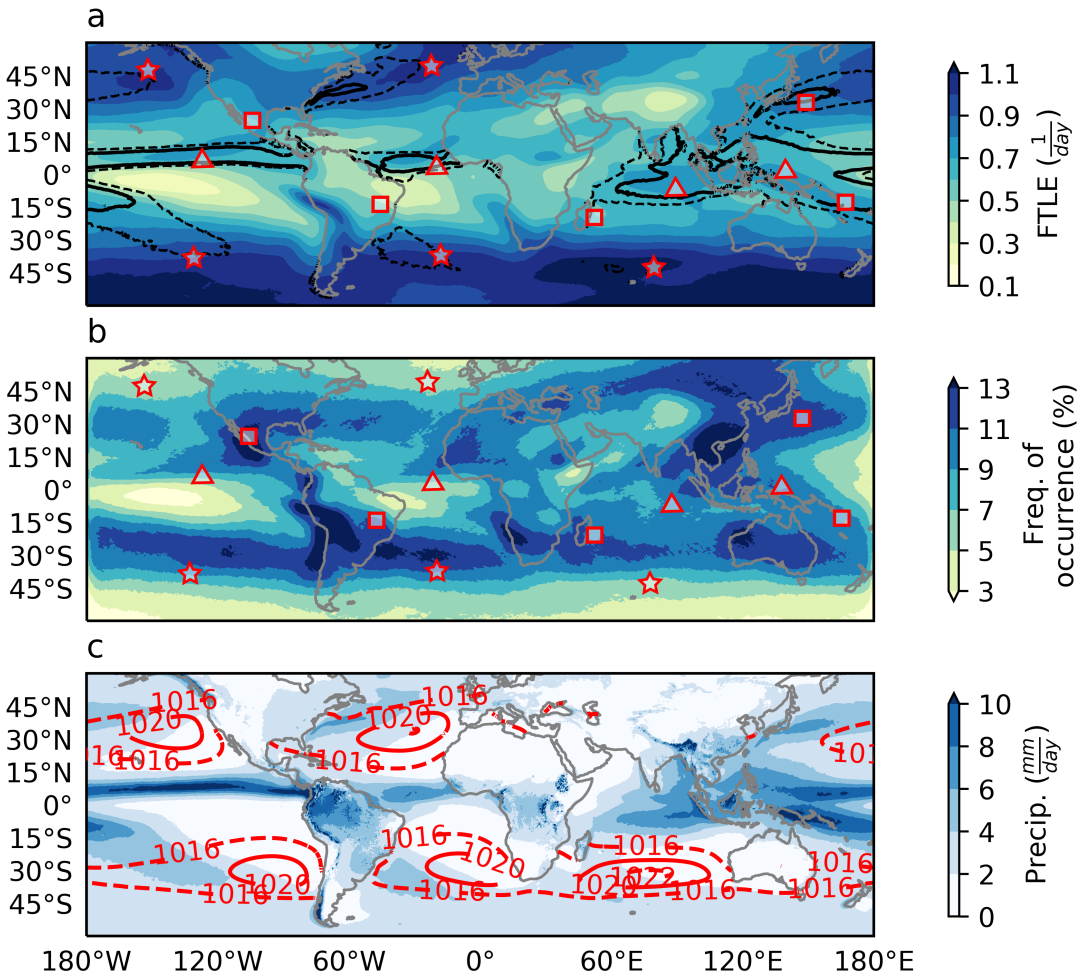

Figure 3.3: Averages between 1980 and 2009 of: (**a**) FTLE (filled contours) and 4 and 6 mm day^{-1} precipitation contours (dashed and solid black contours respectively); (**b**) frequency of LCS occurrence over a homogeneous area of $\approx$ 3100 km^2 and (**c**) precipitation and mean sea-level pressure (MSLP). Red polygons in (a) and (b) are there to assist the text.

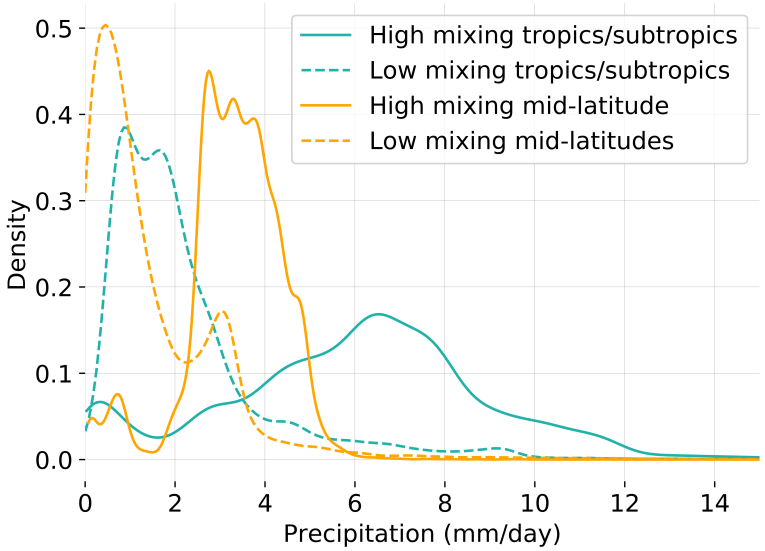

Figure 3.4: Probability density functions of the mean daily precipitation grid boxes in Figure 3.3c separated by latitudinal band and degree of mixing. Subtropical latitudes are defined between $-20°$ and $20°$ and mid-latitudes are defined between $-20°/-50°$ and $20°/50°$. High and low mixing points are separated based on the FTLE value of the grid box using quantiles of 0.1 for low and 0.9 for high mixing. The quantiles are calculated as a function of latitude.

Zonal variability

Atlantic and East Pacific The large-scale mixing pattern characterised by the FTLE and LCS occurrence (Fig. 3.3) in the Atlantic (70°W-15°E) is similar to that of the East Pacific (180°W-90°E). Both sectors present 1) high precipitation and FTLE features in the ITCZ region, 2) mixing minima on the equatorward flank of the subtropical highs, and 3) mixing and precipitation maxima along the poleward flanks of the subtropical highs. The similar relative positions of the subtropical anticyclones (Fig. 3.3c) and the presence of subtropical convergence zones in South America and South Pacific are possible explanations for the likeness between the Atlantic/East Pacific regimes of precipitation and mixing.

West Pacific In the West Pacific sector (120°W, 180°W), in contrast to the Atlantic and the East Pacific, there are no equatorial FTLE and LCS occurrence maxima (Figs. 3.3 a and b). This is expected, considering that the absence of subtropical anticyclones in the West Pacific (Fig. 3.3c) reduces the meridional shear of the zonal winds, consequently reducing the deformation of trajectories at the equatorial band. There is, however, a strong signature of ITCZ precipitation in that region (Fig. 3.3c), suggesting that, in this region, the ITCZ is driven mainly by local thermodynamics rather than by the horizontal redistribution of moisture by the large-scale flow; this is consistent with the dominance of convective precipitation over stratiform precipitation in the West Pacific (Berg et al. 2002). In the Maritime Continent, high contours of FTLE and LCSs overlap with heavy precipitation around the western Pacific warm pool and the South Pacific Convergence Zone (SPCZ). In Northeast Asia, this co-location of high mixing and precipitation contour occurs around the typical location of the Meiyu front and ETC fronts.

Africa and Indian Ocean In the southern part of the African continent there are distinct mixing and LCS features, such as the Congo air boundary and the Kalahari discontinuity; the latter, located at the southwest African coast, presents a particularly strong signature in Fig. 3.3b. These southern African features are known as "drylines" and represent boundaries between moist and dry air (Howard and Washington 2019). In the Indian ocean sector, the main tropical LCS and FTLE feature is a maximum at about 15°N stretching from East Africa to the Indian peninsula co-located with the position of the Somali jet. Near the island of Madagascar at about 18°S, high FTLE, LCS and precipitation contours coincide around the typical position of the South Indian Convergence Zone (SICZ, Cook

2000).

Figure 3.4 summarises the spatial relationship between the averages of mixing and precipitation by showing the probability density functions (PDFs) of the mean daily precipitation grid boxes divided by: (i) intensity of mixing and (ii) latitudinal band. High and low mixing grid boxes are defined above and below FTLE quantiles of 0.9 and 0.1. The quantiles are computed as a function of latitude, so that points reveal distinct mixing regions in relation to their latitudinal band. Tropical and subtropical regions are selected between $20°S$ and $20°N$ and mid-latitudes are defined between $20°S/50°S$ and $20°N/50°N$. We notice that separating precipitation by mixing categories produces clearly distinct precipitation PDFs for both the tropics/subtropics and the mid-latitudes. In the mid-latitudes, the shape of the precipitation PDFs in high and low mixing regions remains similar, but it is shifted towards higher values in the high mixing case. In the tropics and the subtropics, the precipitation PDF in high mixing regions presents both a higher median and higher standard deviation than the precipitation PDF in low mixing regions.

In this section, the spatial analysis of FTLE and precipitation features reveals that, in many regions of the globe, high FTLE and LCS occurrence is co-located with regions of high precipitation. Many of these locations have been identified in literature as regions of convergence zones using a variety of metrics. Our results indicate the usefulness of the proposed framework as a unified diagnostic for identifying convergence zones. In the next section, we present an account of the spatiotemporal variability of the precipitation-FTLE relationship.

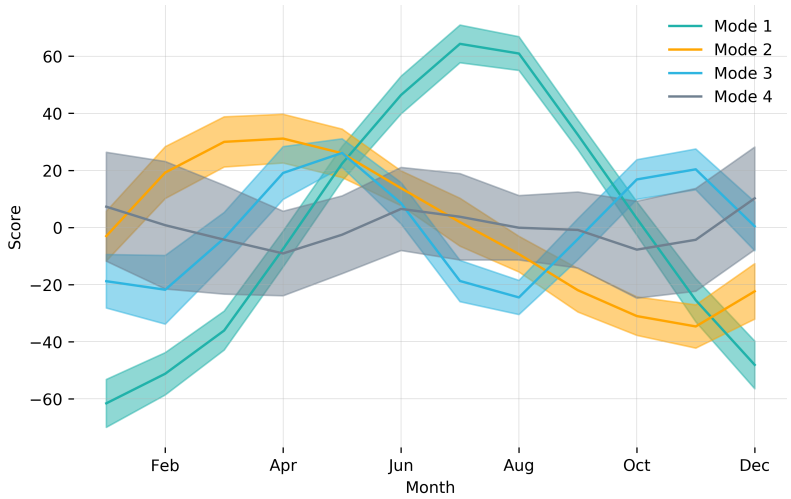

Figure 3.5: Monthly means of the PLS scores (latent variables) associated with modes 1, 2, 3 and 4. The shaded areas represent the interannual standard deviation.

3.3.2 Interannual and seasonal mixing/precipitation relationship

When comparing the precipitation PDFs in Fig. 3.4, there is a clear distinction between the grid-boxes of low and high mixing. However, since the FTLE is measuring the Lagrangian strain within a time interval of 2 days, its association with precipitation is not expected to be necessarily local in space (i.e., at the grid-box level); instead, this association is expected to comprise a neighbourhood around the FTLE feature (see discussion in Perez et al. 2021).

The PLS method is employed here to embed monthly averaged FTLE and precipitation data into pairs of latent variables that are maximally correlated; these latent variables model the covariance relationships between mixing and precipitation considering the entire spatial domain. In order to reduce the computational cost of the PLS method as well as remove high frequency signals, the datasets are downsampled to the monthly scale by calculating the monthly averages of

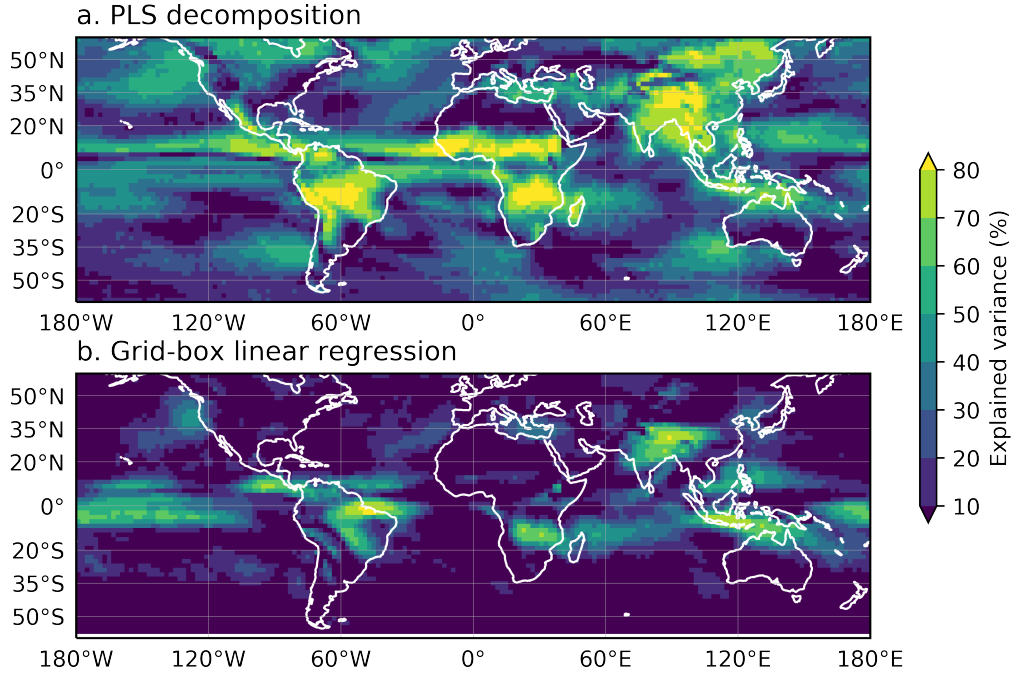

Figure 3.6: Fraction of the precipitation variance (Pearson's r^2) explained by: (a) the four FTLE latent variables obtained by the PLS decomposition and (b) a linear regression of the associated grid-point FTLE and precipitation time series.

the 6-hourly precipitation and FTLE. The PLS algorithm processes the monthly datasets to produce four pairs of FTLE/precipitation latent variables that are most strongly correlated; the time series of the latent modes are shown in the Annex (Figure 3.A.2).

Figure 3.5 shows the monthly average (solid lines) and the interannual variability (shading) of the FTLE modes embedded by the PLS method. We notice that the first mode is strongly seasonal; its amplitude peaks around December-January-February (DJF) and December-January-February (DJF). Mode 2 also varies seasonally, but with smaller amplitude than Mode 1 and peaking in the transition seasons. Mode 3 also presents a clear seasonality, but peaks twice a year in May and November. The interannual variability of the first three modes, represented by the shading, is smaller than their intra-annual variability. Mode 4, on the other hand, varies more strongly at the interannual scale.

The first four FTLE modes identified by the PLS decomposition retain a substantial part of the precipitation variance, particularly over the continent in equatorial and subtropical regions (Figure 3.6) and over the ocean around the ITCZ. In these regions, the explained variance typically over 50% and as high as 90% indicates that the monthly precipitation is well explained by the FTLE modes, pointing to a strong temporal relationship between the two variables. Figure 3.6b shows, for comparison, the explained variance of a linear regression fitted to explain the precipitation time series in each grid-box using the associated FTLE time series of the same grid-box. In some tropical and subtropical regions, the fraction of the variance explained by the PLS algorithm is similar to the grid-box linear regression. In these regions, the temporal FTLE-precipitation relationship is local in space. However, in other locations, such as the Sahel and storm-track

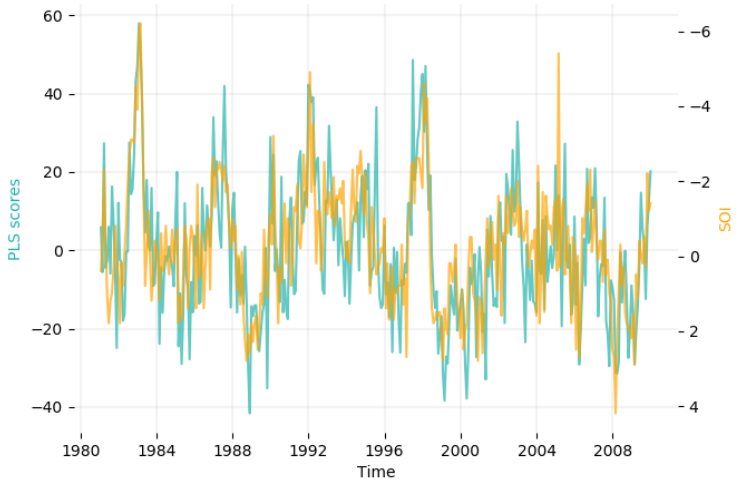

Figure 3.7: Scores associated with mode 4 of the PLS method (left axis) and the Southern Oscillation Index (SOI, right axis).

regions, the PLS explained variance is much higher than the grid-box regression, suggesting that remote mixing features may be influencing precipitation in those regions.

Considering the substantial FTLE-mixing co-variability shown in Fig. 3.6, in the next sections we discuss specific time scales of this co-variability, starting from longer (interannual) to shorter timescales (seasonal and subseasonal). We focus the discussion on the tropical and subtropical regions where the precipitation variability is better explained both by the PLS modes and by the grid-box linear regression.

Interannual variability - ENSO

The fourth FTLE mode presents a strong interannual variability. An obvious candidate to be driving this mode is the El-Niño Southern Oscillation (ENSO), an atmospheric-oceanic coupled mechanism (Jin 1997) known to directly drive tropi-

cal precipitation through changes in the Walker circulation (Ambrizzi et al. 2004) and influence precipitation regimes at higher latitudes through teleconnection mechanisms (Grimm and Silva Dias 1995; Sulca and Rocha 2021). The atmospheric component of the ENSO is typically quantified by the Southern Oscillation Index (SOI), a standardised sea level pressure difference between Tahiti and Darwin, Australia.

Figure 3.7 shows time series of the SOI monthly average along with the scores of the fourth FTLE mode obtained by the PLS method. Simple visual inspection shows that the two time series are well correlated. This indicates that ENSO drives[1] this fourth FTLE mode and, more broadly, underpins the precipitation/mixing relationship on interannual scales.

Figure 3.8 shows the FTLE and precipitation anomalies in months of positive (El Niño) and negative (La Niña) ENSO events defined based on the Niño 3.4 index, a measure of sea surface temperature anomaly in central Pacific that is commonly used to define such events. The FTLE and precipitation anomalies were calculated in relation to the total temporal mean (i.e., the fields shown in Figs. 3.3a and 3.3c). In the equatorial Pacific, there is a co-location between FTLE and precipitation anomalies, indicating a direct impact of the transition of the Walker cell on mixing and precipitation in this region. Remote effects of ENSO on precipitation can be seen in many parts of the world. In many of these remote regions, such as South America and southern Africa, precipitation anomalies are co-located with FTLE anomalies of the same sign. Thus, during ENSO events, higher than average FTLE leads to anomalously high monthly precipitation totals

[1]The causal inference here is simply based on the assumption that ENSO can be explained independently of atmospheric mixing or precipitation patterns.

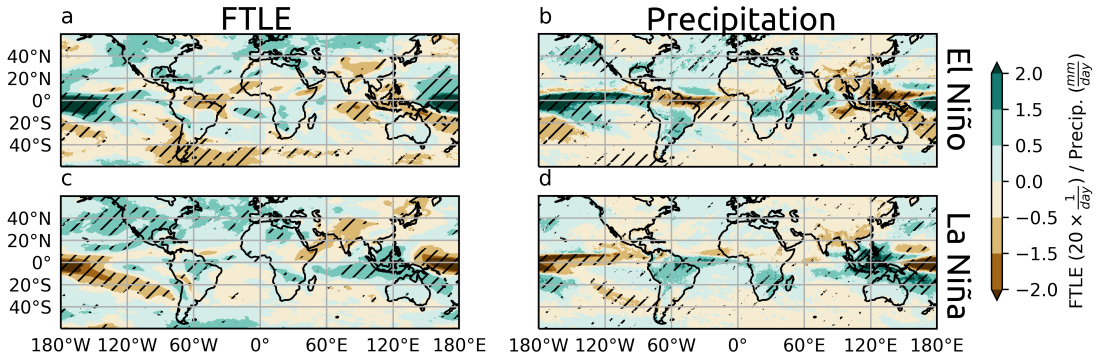

Figure 3.8: FTLE (a, c) and mean precipitation (b, d) anomalies during El Niño (a, b) and La Niña events. Hatched anomalies are significant at the 1% level based on a Student's t-test for the null-hypothesis that the mean of El Niño and La Niña events are not different from total temporal mean.

and vice-versa.

Seasonal variability

Considering that the first PLS mode characterises the DJF/JJA variation (Fig. 3.5), it is of interest to investigate links between precipitation and mixing during these seasons. Figure 3.9 shows FTLE and precipitation anomalies along with mean sea-level pressure (MSLP) in DJF and JJA. The anomalies were calculated by taking the seasonal average and subtracting from the total average (i.e., the fields shown in Figs. 3.3a and 3.3c). We employed the MSLP as a diagnostic of general circulation features, namely the subtropical anticyclones associated with the descending branch of the Hadley overturning circulation.

Figure 3.9 shows anomalies of precipitation and FTLE in DJF and JJA. In most tropical and subtropical regions, these anomalies are of the same sign and visually similar. In particular, the winter/summer migration of the ITCZ precipitation seems to be accompanied by a migration of positive FTLE anomalies. The FTLE anomalies along the Equator seem vary according to the strength of the MSLP

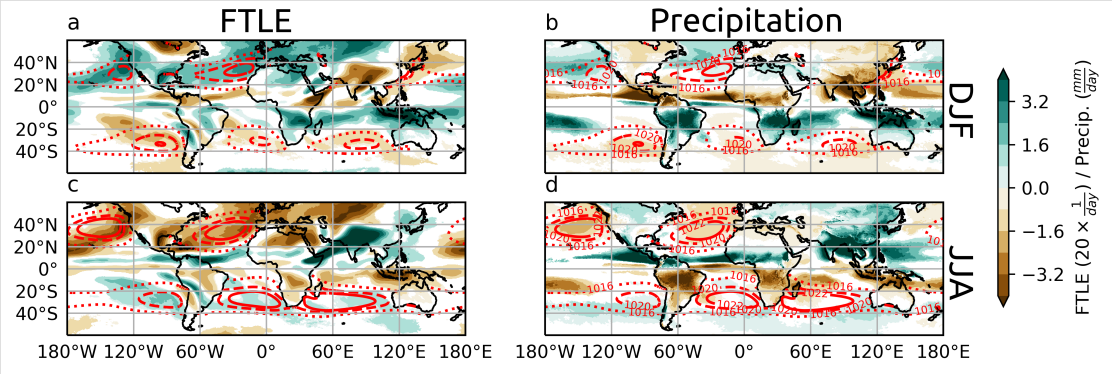

Figure 3.9: Seasonal anomalies of FTLE (a, c) and precipitation (b, d) in DJF (a, b) and JJA (c, d). Average mean sea level pressure is shown in red contours for each season. Precipitation and FTLE contours are only shown when significant at the 1% level based on a Student's t-test for the null-hypothesis that the mean of each season is not different from the total temporal mean.

centres of the adjacent subtropical highs in the Atlantic and East Pacific, suggesting that equatorial mixing is associated with the subtropical anticyclones. On the other hand, the seasonal migration of equatorial mixing in the Indian ocean can be described in terms of the Southeast Asia monsoon winds and the South Indian subtropical high. These migrations will be described in the following paragraphs.

Atlantic The South Atlantic subtropical high presents a strong seasonality (Fig. 3.9), a feature that is particularly influenced by precipitation in the South American monsoon (Rodwell and Hoskins 2001; Reboita et al. 2019). In DJF, equatorial FTLE and precipitation positive anomalies are displaced south as the South Atlantic high pressure centre weakens. In JJA, the South Atlantic high is substantially stronger and the positive FTLE anomalies migrate north at about 10°N. The North Atlantic high is also stronger in JJA, although its seasonality is less pronounced. This suggests that, at the equator, the 2-day FTLE characterises the deformation along the interface of adjacent anticyclones. The migration of this

interface (indicated by positive equatorial FTLE anomalies) is in close agreement with the zonal migration of equatorial precipitation, suggesting that the seasonal migration of the Atlantic ITCZ could be linked with the ability of the large-scale horizontal flow to organise moisture filaments. In other words, Fig. 3.9 suggests that the migration of the Atlantic ITCZ is linked to the migration of the band of maximum FTLE. The strength of this band of maximum FTLE appears to be associated with the strength of the adjacent anticyclones.

Pacific We notice a similar behaviour in the eastern Pacific in terms of the relationship between the strength of subtropical gyres and mixing/precipitation at the equator. The North Pacific high is substantially stronger in JJA and the FTLE and precipitation anomalies are positive at 10°N. In DJF, the FTLE and precipitation anomalies at 10°N become negative as the North Pacific high weakens. This suggests that, in the East Pacific, mixing and precipitation along the ITCZ are also linked with the strength of the adjacent subtropical anticyclones. In the western Pacific, we notice a close agreement between FTLE and precipitation anomalies around the Maritime Continent and northern Australia.

Africa and Indian Ocean In DJF, FTLE (Fig. 3.9a) and precipitation (Fig. 3.9b) positive anomalies stretch from Madagascar to the Maritime Continent. DJF is the dry season of the Indian monsoon, during which the low-level flow is expected to come from the Asian continent to the Indian ocean. This suggests that the stronger mixing over the Indian ocean in DJF is characterised by the Lagrangian deformation at the interface between the southeasterlies from the South Indian subtropical high and the outflow from the Asian Monsoon. During JJA, the Asian

monsoon wet phase, the Lagrangian deformation over the tropical Indian ocean is expected to decrease, as the monsoon winds will not be in opposition to the southeasterlies from the subtropical anticyclone. Accordingly, in JJA, both the FTLE Fig. (3.9c) and precipitation (Fig. 3.9d) anomalies are negative over the tropical Indian ocean.

3.3.3 Intraseasonal variability in the Atlantic and South America

In the previous section we employed the PLS method and composite analyses to show that precipitation and mixing are related on seasonal and inter-annual scales in various regions around the globe. Here, we narrow down our analysis to the East Pacific, Americas and Atlantic sectors to investigate the mixing-precipitation relationship under specific modes of sub-seasonal variability, namely the Madden-Julian Oscillation (MJO) and the North Atlantic Oscillation (NAO). This section focuses on the DJF season, the season in which MJO peaks are stronger and the winter NAO is well-defined. Global maps of the results presented here can be found in the Annex.

MJO

In phases 8 and 1, the MJO transitions from a slow and wet Kelvin/Rossby wave to a fast and dry Kelvin wave while it propagates eastward across the East Pacific and Atlantic. Before entering the dry Kelvin wave regime, MJO pulses trigger Rossby wave trains that enhance precipitation in the SACZ and the SPCZ; it elongates the SPCZ precipitation eastward (Matthews 2012) and enhances the

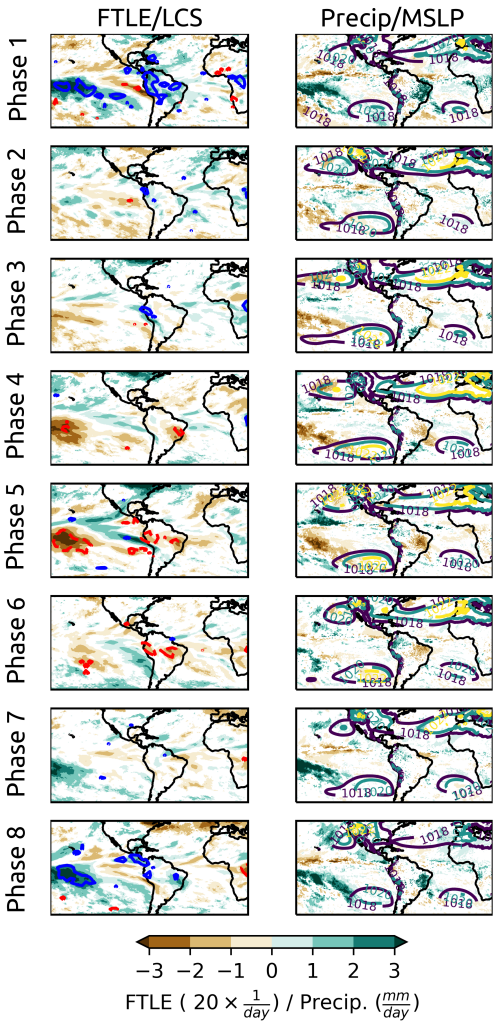

Figure 3.10: Anomalies during MJO events in DJF of: FTLE and LCS occurrence (left column) and precipitation (right column). LCS frequency of occurrence anomalies in the left column are shown as red and blue contours, representing anomaly levels of -2% and $+2\%$ respectively. MSLP contours are also shown in the right column. Precipitation and FTLE contours are only shown when significant at the 1% level based on a Student's t-test for the null-hypotheis that the MJO events have the same mean of the season (DJF).

SACZ (Grimm 2019). In phases 4 and 5, the effect of the MJO teleconnection is opposite; precipitation is suppressed in the SACZ and SPCZ regions. In the other phases (2, 3, 6 and 7) the FTLE, LCS occurrence and precipitation anomalies are consistently weaker.

Figure 3.10 shows anomalies of the FTLE, precipitation, and LCS occurrence during MJO pulses in DJF. MJO events are defined when the amplitude of the real-time multivariate MJO index (RMM, Wheeler and Hendon 2004) is greater than one. The anomalies are computed as the difference between the averages during MJO events of each phase and the seasonal mean of DJF. In many cases, there is an agreement in the signs of FTLE, LCS and precipitation anomalies. In phases 1 and 8, the frequency of LCSs, the FTLE and precipitation are enhanced over South America and South Pacific. In phases 4 and 5, this behaviour is opposite: the large-scale mixing is less favourable for moisture filamentation in the SACZ and SPCZ regions, as indicated by negative FTLE and LCS anomalies coinciding with negative precipitation contours. However, there are cases where FTLE and LCS anomalies are not reflected as precipitation anomalies, such as in northwestern Amazon during Phase 1.

NAO

The equatorial Atlantic has a strong influence on South American precipitation because the meridional gradient of Atlantic equatorial sea surface temperatures (SSTs) and the position of the Atlantic ITCZ modulate spatial and temporal variability of precipitation over northeastern Brazil and the Amazon (Souza and Cavalcanti 2009; Yoon and Zeng 2010; Marengo et al. 2011; Fernandes et al. 2015; Jones and Carvalho 2018). On the other hand, the tropical Atlantic SSTs are

modulated by the strength of the surface easterlies in the subtropical North Atlantic, where the effect of North Atlantic Oscillation is strong (Hurrell et al. 2003; Kushnir et al. 2006; Souza and Cavalcanti 2009). This suggests that the NAO could influence precipitation over South America on subseasonal time-scales but the extent of these teleconnections has not been quantified in the literature.

This section investigates whether there is any influence of the NAO on South American precipitation at sub-seasonal scales in DJF, focusing on the role of mixing structures in this inter-hemispheric teleconnection, as an example of the potential use of these mixing diagnostics to disentangle mechanisms of precipitation variability.

Events associated with the positive and negative phases of the NAO (Hurrell et al. 2003) are defined first by computing the normalised time series of the first Empirical Orthogonal Function (EOF) of the MSLP field over the Atlantic sector (90°W-40°E, 20°-80°N) using ERA5 data. Subsequently, a positive NAO event is defined when the index is higher than 1 for at least 6 consecutive days, with at least a 20-day separation from the latest previously defined event. Negative NAO events are defined in an analogous fashion, but with a negative threshold for the first principal component time-series index. Figure 3.A.3 in the Annex illustrates the selection of events.

We now focus on the differences between positive and negative NAO pulses in DJF (hereafter referred to as NAO anomalies). The anomalies were temporally smoothed in a five day window centred around each lag. The lagged NAO precipitation composites in Figures 3.11d and 3.11f show significant anomalies 5 and 10 days after the pulse around the ITCZ and the South American continent. Interestingly, the associated FTLE and LCS occurrence anomalies in Figures 3.11c

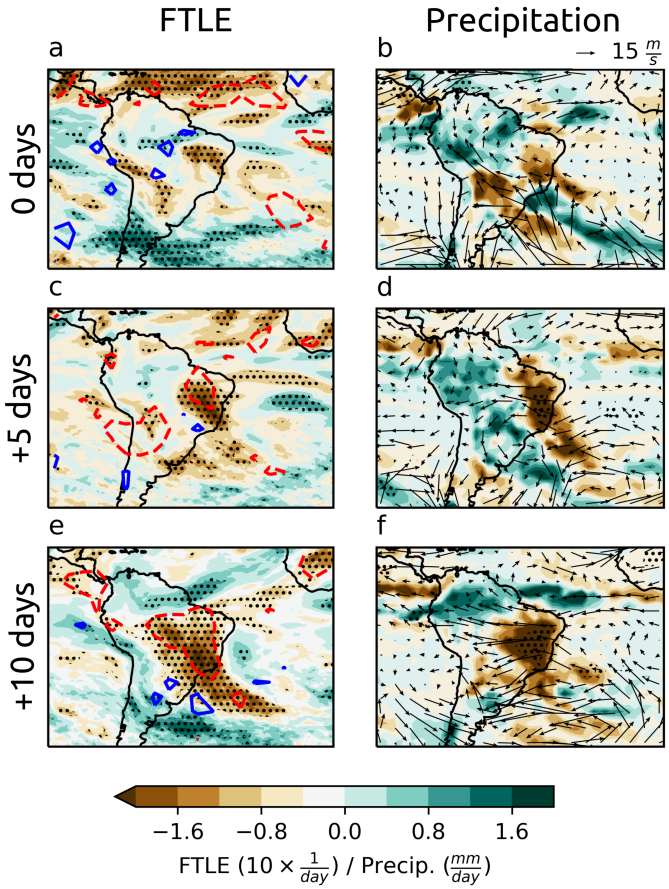

Figure 3.11: Lagged anomalies of FTLE, LCS frequency of occurrence, precipitation and $\boldsymbol{V}_{\rho_v}$ during NAO events in DJF. Left column: FTLE anomalies in filled contours and LCS occurrence in blue and red contours, representing anomaly levels of -2% and $+2\%$ respectively. Right column: Precipitation and $\boldsymbol{V}_{\rho_v}$ anomalies. Stippled anomalies are significant at the 1% level based on a Student's t-test for the null-hypothesis that positive and negative NAO events have the same mean.

and 3.11e indicate that large-scale flow kinematics is unfavourable for the formation of moisture bands, hence suppressing the formation of coherent precipitation features such as the SACZ. Considering that these anomalies are composed by the difference between positive and negative NAO events, Figure 3.11 tell us that positive NAO events suppress the SACZ and enhance the ITCZ, while negative NAO events have the opposite effect. The anticyclonic anomalies of $\boldsymbol{V}_{\rho_v}$ in Figs. 3.11d in the South Atlantic suggest that the negative FTLE anomalies at the SACZ region may be explained by an intensification of the South Atlantic subtropical high.

Figure 3.11 suggests an inter-hemispheric teleconnection, where NAO pulses propagate to the Southern Hemisphere, controlling mixing and precipitation in South America. We hypothesise that there is a causal relationship linking NAO pulses and South American precipitation mediated by the Hadley meridional overturning. This hypothesis can be described as follows: positive (negative) NAO pulses strengthen (weaken) the upwelling at the ITCZ, strengthening (weakening) the southern Hadley cell and the downwelling at the South Atlantic anticyclone (notice the anticylonic anomalies at lag +10 days in Fig. 3.11).

To support this hypothesis, Figure 3.12 shows the anomalies of vertical wind speed zonally averaged between $75°W$ - $20°W$. Similarly to Figure 3.11, the anomalies are shown as differences between positive and negative NAO events and averaged in five day windows around each lag. On the day of the NAO pulse (lag 0), the strongest anomalies are in the Northern Hemisphere, where descending motion is enhanced between $30°N$ - $60°N$. Five days after the event, weaker vertical motion anomalies appear around mid and upper tropospheric levels (200 - 600 hPa) in subtropical latitudes ($0°$ - $30°N$). Ten days after the event's peak, the dominating

anomalies are in the Southern Hemisphere. The enhanced downwelling around $25°S$ is consistent with the anticyclonic anomalies at lag +10 days in Fig. 3.11, which indicates a strengthening of the South Atlantic high.

Together, Figures 3.11 and 3.12 suggest that NAO pulses propagate via the Hadley overturning, establishing vertical wind speed anomalies in the Southern Hemisphere. These anomalies seem to modulate the large-scale horizontal flow around the South Atlantic anticyclone, thus controlling mixing and the occurrence of LCSs at the SACZ and ITCZ regions. Changes in frequency and intensity of these convergence zones then contribute to the precipitation anomalies observed in South America after the NAO pulse. An alternative hypothesis to explain the anomalies in Fig. 3.11 is offered in the next section.

3.4 Discussion

3.4.1 Spatial distribution of mixing and LCSs

Broadly speaking, the horizontal distribution of the 2-day FTLE (Fig. 3.3a) indicates that high values of horizontal mixing is related to the typical positions or interfaces of semi-permanent and transient eddies such as ETCs and subtropical anticyclones. Regions of minimal mixing can be seen along the equatorward branches of subtropical gyres, indicating that trajectories behave as parallel southeasterly or northeasterly flows. Along the ITCZ, higher mixing is indicated between these northern and southern easterlies. At the poleward edges of the subtropical gyres, FTLE maxima suggest that the interaction between the anticylclones and ETCs produce a highly mixed environment; this is noticeable mainly at the North At-

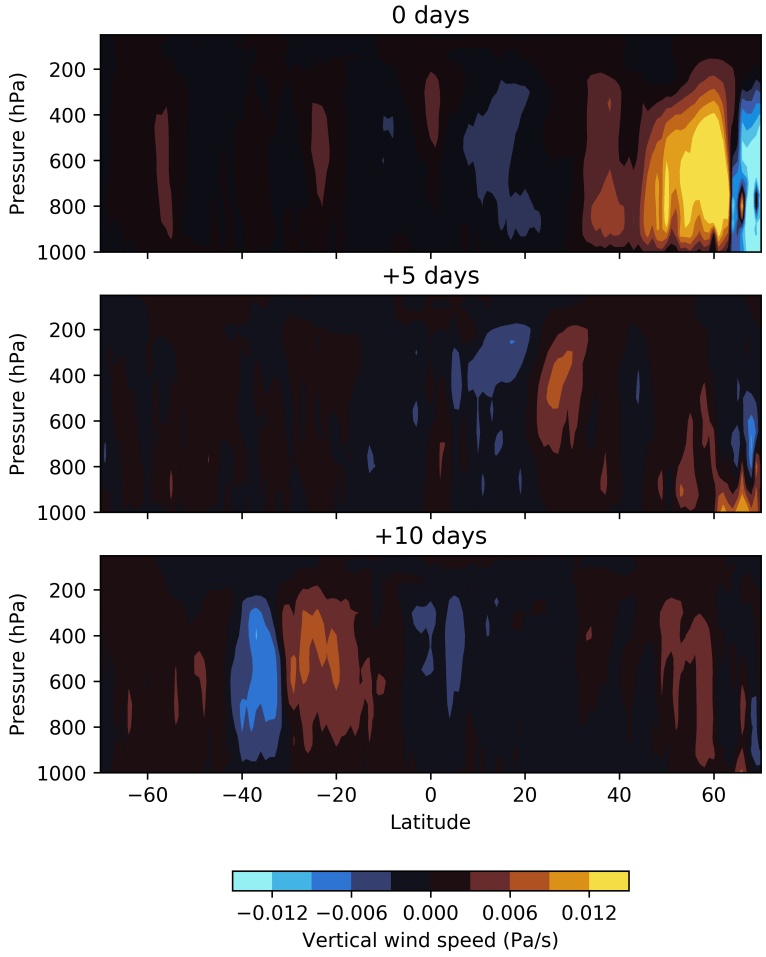

Figure 3.12: Vertical wind speed difference (Pa/s) between positive and negative NAO events in DJF averaged in a longitudinal slice over the Atlantic and Americas ($75°W$ - $20°W$).

lantic and North Pacific. This is consistent with numerical experiments performed by Lapeyre 2002 in idealised 2D turbulence; the authors point that regions whereby eddies interact are associated with higher FTLE values.

The LCS frequency of occurrence in Figure 3.3b naturally bears some similarities with the FTLE distribution, considering that LCSs are defined as FTLE ridges. However, while the average intensity of mixing increases with latitude (this is also shown by Garaboa-Paz et al. 2017), the frequency of occurrence of LCSs decreases rapidly at latitudes higher than 45°. This is consistent with the frequency of occurrence of ETC fronts, that typically peaks at mid-latitudes and decreases closer to the pole (Catto et al. 2014). Other aspects, however, could explain the high-latitude FTLE/LCS comparative discrepancy. For example, it could be that the internal dynamics of some ETCs is such that they do not fall within our definition of LCSs in $\boldsymbol{V}_{\rho_v}$. From another point of view, it could also be the case that some aspects of the ETCs are more appropriately defined as other types of coherent structures, such as hyperbolic or elliptic LCSs (Serra et al. 2017). Regardless, a case-study oriented investigation could help uncover the relationship between ETCs and LCSs.

3.4.2 Precipitation-mixing association

The FTLE and precipitation are associated at multiple spatial and temporal scales. Global averages of FTLE and precipitation spatially co-located; regions of stronger mixing are associated with higher precipitation medians and more frequent extremes (Fig. 3.4). This FTLE/precipitation relationship is not only spatial, but spatiotemporal, as shown by the PLS decomposition and seasonal/interannual

composites. I.e., FTLE/precipitation anomalies are not only co-located, but their temporal variability is in phase in many regions.

The interannual PLS mode is highly correlated with the SOI index, indicating that the ENSO modulates the global FTLE/precipitation co-variabiltiy (Fig. 3.7). Moreover, significant FTLE and precipitation anomalies are co-located during El Niño and La Niña months (Fig. 3.8). This suggests that some of the remote ENSO precipitation anomalies are associated with changes of large-scale mixing that may favour or suppress the development of organised moisture bands depending on the phase of the oscillation. In southern Africa, for example, coherent cloud bands associated with the SICZ are more likely to happen during La Niña events (Hart et al. 2018); consistently, there are significant positive FTLE anomalies during La Niña events in that region (Fig. 3.8d). In South America, the precipitation dipole that reverses sign depending on the ENSO phase (Bombardi et al. 2014) can be explained by FTLE anomalies. These FTLE anomalies suggest that the ENSO impacts on South American precipitation are mediated by the ITCZ and the SACZ, considering that the FTLE is a diagnostic for both convergence zones (Perez et al. 2021).

At the seasonal scale, the dominant PLS mode peaks in JJA/DJF, suggesting that precipitation and mixing variability are connected through summer/winter mechanisms such as the migration of the Hadley cell. This is further confirmed by the seasonal anomalies of precipitation, FTLE and MSLP in Figure 3.9, where we see that tropical and subtropical anomalies of precipitation and FTLE are co-located, particularly along the ITCZ and monsoon regions. We notice that the sign and intensity of the FTLE anomalies near the Atlantic and Pacific ITCZ are associated with the strength of the adjacent subtropical anticyclones; i.e., in

JJA mixing is stronger at the ITCZ while the MSLP of the anticyclones is also stronger. The opposite happens in DJF. This suggests a direct link between the Hadley overturning and horizontal large-scale mixing at the tropics. Rodwell and Hoskins 2001 discussed the role of tropical precipitation in idealised simulations in producing realistic subtropical anticyclones.

At subseasonal scales, the FTLE composites highlight important mechanisms of precipitation. During MJO pulses in DJF, precipitation, mixing and LCS occurrence anomalies in the Pacific, Americas and the Atlantic are co-located. This supports that the MJO controls precipitation in those regions by the means of enhancing or suppressing kinematical mechanisms like convergence zones. The agreement between the FTLE and precipitation anomalies is especially noticeable in southeastern and northeastern Brazil during Phases 1 and 8, where the propagation of Rossby waves through the Pacific-South Atlantic channel has been shown to enhance SACZ precipitation (Grimm 2019). Noticeably, in the Atlantic ITCZ, around the northeastern coast of South America, the FTLE does not seem to explain the negative precipitation anomalies in Phase 1. In that phase, the fast Kelvin wave is known to suppress precipitation in that region (Sobel and Kim 2012). The absence of a counterpart negative FTLE anomaly indicates that this precipitation suppression does not rely on the horizontal kinematics of moisture transport. Interestingly, Rossby waves, such as the MJO teleconnection through the Pacific-South American (PSA) channel, seem to be more effective in creating the FTLE anomalies than equatorial Kelvin waves. Shepherd et al. 2000 observed the same effect when comparing mixing regimes in the stratosphere and the mesosphere: the stratospheric flow, dominated by Rossby waves, is more likely to generate coherent tracer filaments than the mesospheric flow, typically dominated

by high wave numbers.

Similarly to the MJO, the NAO lagged composites (Fig. 3.11) also indicate the existence of a remote influence on precipitation by the means of changing the horizontal kinematics of moisture distribution: after an NAO pulse, significant precipitation anomalies arise around the ITCZ and SACZ regions; these anomalies are co-located with FTLE anomalies. In Figure 3.12, we explore the hypothesis that this teleconnection is mediated by the Atlantic Hadley overturning (Figure 3.12). An alternative, but not mutually exclusive, hypothesis would be that the MJO acts as a confounding factor, controlling both the NAO and the South American precipitation. We notice that the negative FTLE and precipitation anomalies in South America after NAO pulses (Fig. 3.11) are similar to the MJO anomalies in phases 4 and 5 (Fig. 3.10). Indeed, the MJO modulates the impact of the NAO consistently: in phases 4 and 5, the MJO intensifies positive NAO pulses while suppressing negative NAO pulses (Cassou 2008). Considering that the MJO acts as a confounding factor, a more detailed investigation should be performed before establishing a firm causal link between the NAO and South American precipitation.

3.4.3 A comment on mixing-precipitation causal pathways

Broadly speaking, the results suggest a causal relationship between features of large-scale horizontal mixing and precipitation. A possible causal pathway is that large-scale mixing features reshape the moisture distribution, controlling regional precipitation regimes. This causal pathway is based on: (i) the flow $\boldsymbol{V}_{\rho_v}$ (Eq. 3.1) was defined to represent the moisture pathways, (ii) ridges of the backwards

FTLE (Eq. 3.2) represent attracting structures and (iii) the back-trajectories were computed well within the median residence time of moisture in the atmosphere. The causal relationship could also go in the opposite direction; i.e., precipitation features may cause changes in horizontal mixing. For example, the condensational heating associated with precipitating clouds intensifies the low-level horizontal shear and dilation of air parcels (Dias and Pauluis 2009), potentially influencing the FTLE. Such co-dependence between mixing and precipitation could even create a positive feedback mechanisms. For example, near the Atlantic and Pacific ITCZ in JJA, the band of positive FTLE anomalies (Fig. 3.9) favours the organisation of coherent cloud bands that increase precipitation, which, in its turn, might increase existing positive FTLE anomalies.

Alternatively, it could be argued that the FTLE/precipitation relationship is not one of cause and effect. This is the same to say that the purely kinematic ability of the flow to shape the horizontal moisture distribution has little or no influence on precipitation and vice-versa. This could be the case when mixing features coincide with dynamically active regions (i.e., regions of intense vertical motion) with enough local moisture supply such that large-scale transport does not contribute significantly to precipitation. However, this is unlikely to be the case in most regions since the median residence time of moisture even in dynamically active structures such as ETCs (estimated to be approximately two days, Papritz et al. 2021) is long enough for moisture trajectories to be deformed by the large-scale flow. Nonetheless, this potential confounding effect could be untangled in a future study by decomposing precipitation anomalies in terms of vertical motion and moisture anomalies. Such decomposition would quantify the individual contributions of kinematics (horizontal transport) and dynamics to precipitation.

3.5 Conclusions and final remarks

In this study we present a global climatology of the Finite-Time Lyapunov Exponent (FTLE) and Lagrangian Coherent Structures (LCSs), discussing the relationship between mixing and precipitation features in subseasonal, seasonal interannual scales. We show that a number of aspects of precipitation variability can be explained by mixing features, particularly in tropical and subtropical regions. These results extend the analyses of Perez et al. 2021 to a global scale, suggesting that attracting LCSs are able to identify convergence zones and other similar precipitation mechanisms without relying on region-specific information such as existing convergence zone detection algorithms.

The application of the conceptual and mathematical framework of mixing and LCSs is in still its early stages in meteorology and remains unknown to the majority of field experts. This is unsurprising, considering that the theoretical basis is relatively recent (Haller and Yuan 2000) and still undergoing development (Balasuriya et al. 2018; Nolan et al. 2020). Moreover, the computation of Lagrangian diagnostics is usually more complex and expensive than Eulerian diagnostics, with little literature on how to overcome the practical limitations of processing global atmospheric data. However, we argue that there is much to be gained by the weather and climate communities from adopting Lagrangian kinematic frameworks, especially if we consider that the concentration of long-lived properties directly impacts human activities, such as volcanic ash (Dacre and Harvey 2018), biomass-burning smoke (Gonzalez-Alonso et al. 2019) and water vapour. In the context of climate change, identifying the underlying mechanisms of moisture accumulation and their relationships with precipitation can help assess the limitations of climate models in

the present climate and derive storylines to provide useful information for decision-makers where changes in regional precipitation regimes are uncertain (Shepherd 2014).

We hope that the broad nature of the analyses presented here will motivate future studies in the use of Lagrangian kinematics to diagnose features associated with coherent tracer accumulation, such as tropical rain bands and fronts.

Appendix

3.A Supplementary figures

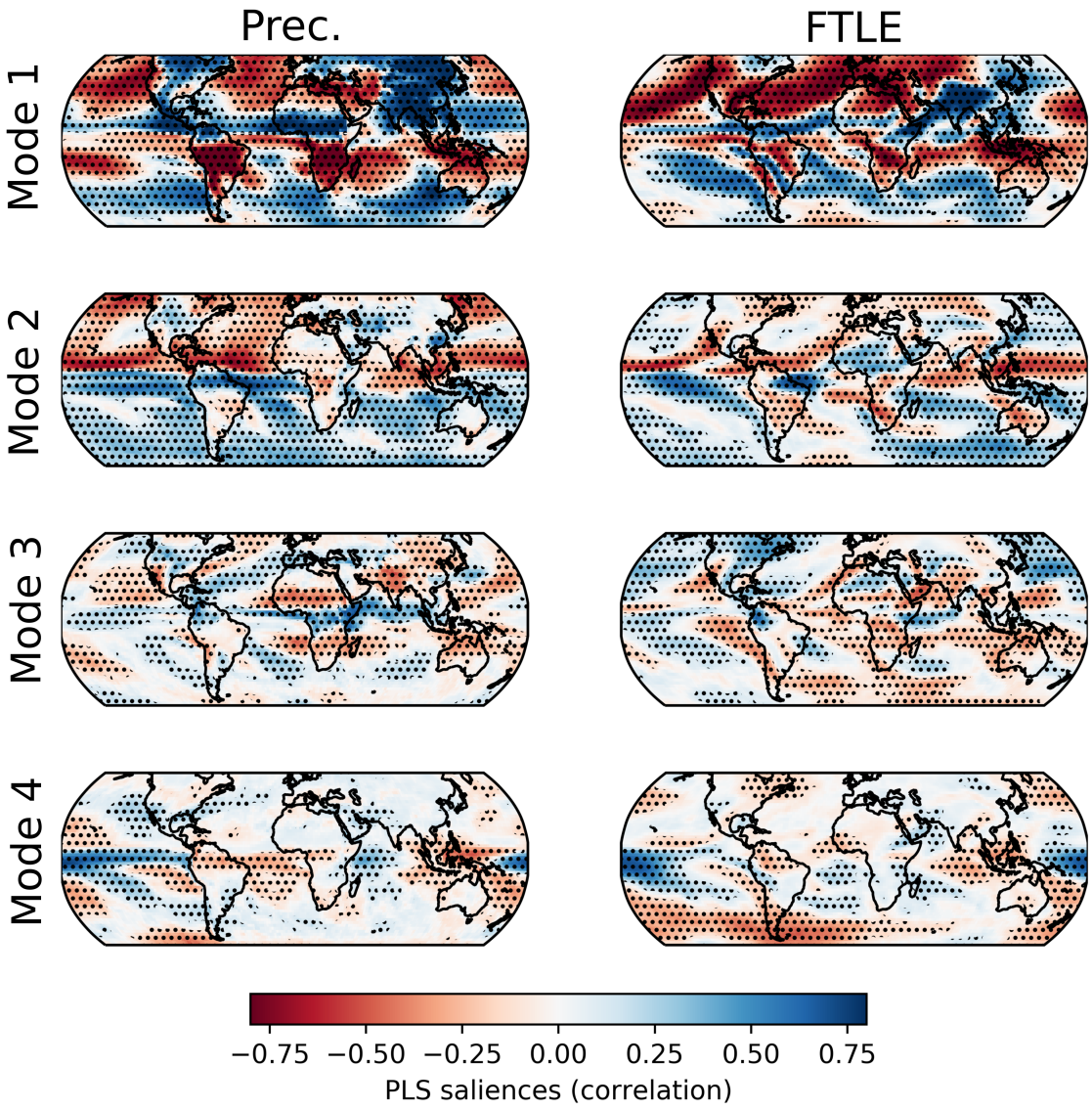

Figure 3.A.1: FTLE and precipitation spatial modes obtained from the PLS decomposition. Stippling shows correlations significant at the 1% level based on a Student's t-test.

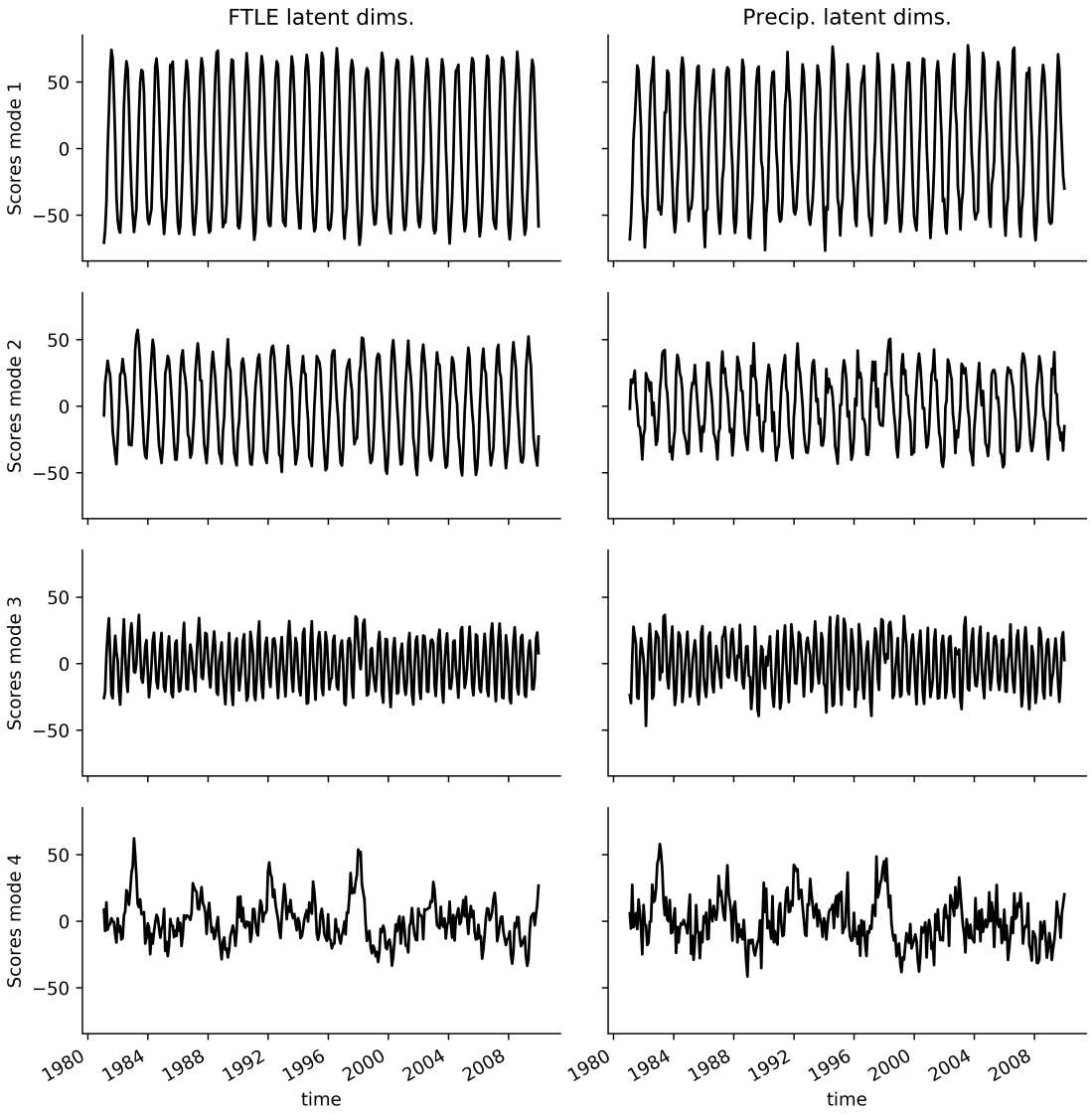

Figure 3.A.2: Time series of the 4 pairs of latent variables obtained from the PLS decomposition.

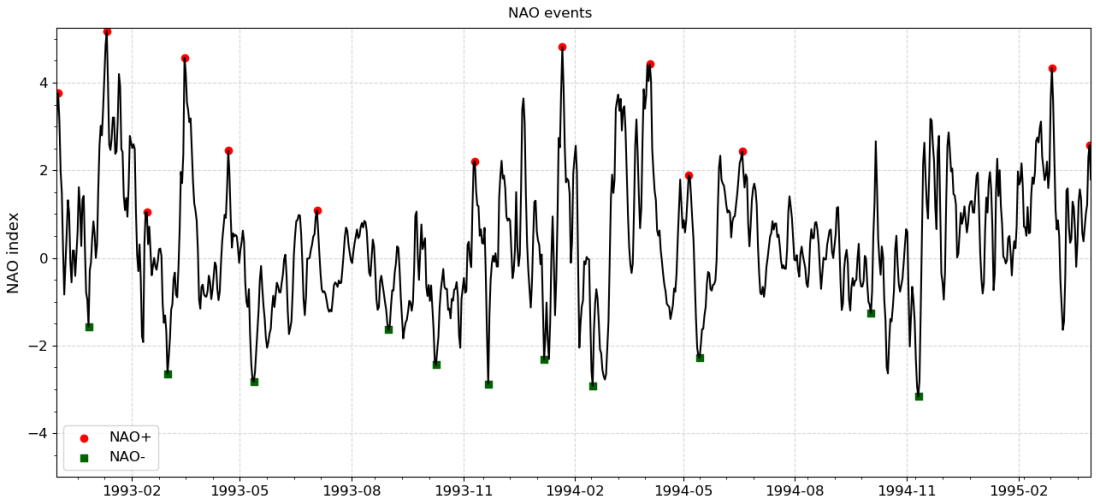

Figure 3.A.3: Time series of the normalised first principal component of the Atlantic sector sea-level pressure, referred to as NAO index. NAO positive events are marked with a red circle and negative events with a green square.

Chapter 4

How much does it rain over convergence zones? Assessing observations and climate model biases

This chapter is a draft of a paper soon to be to the Journal of Geophysical Research.

Authors: Gabriel M P Perez, Pier Luigi Vidale, Helen Dacre, Thomas Martin

Abstract

Although convergence zones (CZs) are known drivers of regional precipitation regimes, there is an absence of techniques to assign precipitation to CZs globally. In this study, we build upon a recently developed diagnostic of synoptic-scale horizontal mixing to allocate precipitation to convergence zone events in observations and simulations submitted to the Coupled Model Intercomparison Project 6 (CMIP6). Observed CZs are identified using ERA5 reanalysis wind and allocated precipitation from observational products based on satellite estimates and rain gauges. We estimate that approximately 54% of global precipitation falls over CZs; this proportion is greater than 60% at the Intertropical Convergence Zone (ITCZ) region and subtropical monsoon regions. All CMIP6 simulations analysed here allocate more precipitation to CZ events than the observations suggest. To investigate this overestimation, we decompose the precipitation error in terms of frequency and intensity of CZ precipitation and find that all models present a significant positive bias in the frequency of CZ precipitation. Among the analysed models, CNRM-CM6-1, developed by the Centre National de Recherches Météorologiques and Cerfacs, presents an apportionment of precipitation to CZs closest to the observational estimates. Our results indicate that improving how climate models simulate precipitation over mixing features, which enhance moisture gradients via advection, can mitigate important precipitation biases, such as the double-ITCZ in the Pacific.

4.1 Introduction

Advection by the low-level horizontal flow reshapes the atmospheric moisture distribution so as to support large-scale organised precipitation features; this occurs around well-known features associated with the confluence of airmasses[1] such as fronts, the Intertropical Convergence Zone (ITCZ) and subtropical convergence zones (Kodama 1992; Cohen and Kreitzberg 1997). Generally, we will be referring to these phenomena as convergence zones (CZs). Most algorithms to identify CZs are region specific, i.e., they are calibrated to capture rainfall or cloudiness bands with certain local characteristics (Carvalho et al. 2004; Van Der Wiel et al. 2016). The case of fronts is an exception; fronts can be objectively detected by thermodynamic parameters and precipitation in their neighborhood can be masked (Catto et al. 2015). However, such thermodynamic parameters are not effective in the tropics and subtropics, where the atmosphere is mostly barotropic and airmass boundaries do not show a distinct signature in thermodynamic variables.

Weller et al. 2017 apply an Eulerian metric on 6-hourly wind fields to identify convergence lines in the low-level flow. The authors further mask precipitation around these lines using a fixed-distance criterion and estimate that between 55% and 96% of the precipitation (between 60°N and 60°S) is associated with these convergence lines, with large differences in the estimates over land and ocean. A shortcoming of their approach is that the instantaneous convergence field over land is noisy, resulting in climatologies that are hard to interpret. Moreover, Eulerian convergence lines do not necessarily favour moisture accumulation as the pathlines along which moisture is transported diverge from the instantaneous

[1] Here we refer to airmass as parcels of air with a similar origin in space.

streamlines (see discussion in Section 1.1.3) within the median lifetime of water vapour (approximately 4 days, Läderach and Sodemann 2016).

The ability to associate precipitation with weather phenomena, such as CZs, is an important step in identifying and understanding the causes of model biases and enabling the improvement of models as well as of their use (Leung et al. 2022). Important biases in mean precipitation are still present in CMIP6 simulations (Li et al. 2021), limiting the reliability of future climate simulations. The double ITCZ is one such problem that has been present in CMIP3, CMIP5 and still persists in CMIP6 (Tian and Dong 2020). Catto et al. 2015 have shown that, in the mid-latitude winter, errors in the frequency and intensity of frontal precipitation also explain a substantial portion of the precipitation biases in CMIP5 models.

In this study we define CZ precipitation as precipitation occurring under conditions where the Lagrangian kinematics of the synoptic-scale flow favours the accumulation of moisture. We build upon the mixing diagnostic developed in Perez et al. 2021 to propose a spatio-temporal masking technique that allows the allocation of precipitation to CZs. We then adapt the decomposition in Catto et al. 2015 to perform a process-based evaluation of precipitation biases in CMIP6 models in terms of frequency and intensity of CZ precipitation. The scientific questions we aim to answer are the following:

1. What fraction of global precipitation falls over convergence zones?
2. Are climate models capable of representing this apportionment?
3. What is the contribution of frequency and intensity of CZ precipitation to model biases?

4.2 Synoptic-scale mixing and precipitation

Filaments of high tracer concentration in the atmosphere arise as a consequence of mixing, which is defined as the stretching and folding of material contours caused by advection (Welander 1955; Ottino 1989; Methven and Hoskins 1999). Mixing can be quantified by the Finite-Time Lyapunov Exponent (FTLE), a measure of the Lagrangian deformation of neighbouring parcels (Pierrehumbert 1991; Shepherd et al. 2000). When trajectories are computed to represent pathways of water vapour, FTLE features identify flow structures that promote moisture accumulation. Some key considerations have to be made in order to find the relevant pathways: (a) the duration of the back-trajectories and (b) the flow from which the trajectories are computed. Here we follow the approach in Perez et al. 2021 and Perez et al. 2022 and compute 2-day back-trajectories in a horizontal flow derived from a vertical weighting that accounts for moisture concentration at each vertical level. A similar approach was adopted by Garaboa-Paz et al. 2015; Garaboa-Paz et al. 2017 to investigate atmospheric rivers as FTLE features.

FTLE features computed as described above quantify the purely kinematical effect of mixing in enhancing existing gradients via advection. The extent of the effect of FTLE features on precipitation will therefore depend on the existing background moisture distribution and on the presence of vertical motion that enables parcel saturation and precipitation, such as slantwise ascent or convection. Indeed, Perez et al. 2022 show that the sensitivity of monthly-mean precipitation to the FTLE varies across the globe; particularly, this relationship is stronger in tropical and subtropical regions, where total column water vapour is typically higher than in the extratropics. In the next section, we describe a masking technique to assign

precipitation to CZs that accounts for the spatially dependent mixing-precipitation relationship.

4.3 Convergence zone precipitation mask

We allocate precipitation to CZ events in a given grid-box based on two criteria: (i) the FTLE is positive, meaning that air parcels arriving at the CZ are approximating each other in a 2-day time interval and (ii) the FTLE value of that grid-box is higher than a threshold σ'. The threshold σ' is defined per grid-box as a function of the probability of a precipitation event occurring: σ' is the FTLE value of a quantile that is as frequent as a precipitation event $P > 1$ mm/day in that grid-box. It can be written as:

$$\sigma' = F_\sigma[F_P^{-1}(P > 1\tfrac{mm}{day})] \tag{4.1}$$

where F_P^{-1} is the inverse Cumulative Density Function (CDF) of precipitation and F_σ is the CDF of the FTLE. This look-up process is illustrated in Figure 4.1.

Assigning precipitation to CZs when the FTLE exceeds the spatially dependent threshold σ' serves two purposes: (i) it compensates for the meridional variation in mean FTLE values, which are typically higher at higher latitudes and (ii) it accounts for the spatially dependent mixing-precipitation relationship described in Section 4.2. I.e., if precipitation events are rare in a given region, CZ precipitation is masked with with equally rare FTLE contours. In the same way, if precipitation is very frequent, we will look for FTLE contours that occur frequently. Global maps of σ' are shown in Figure 4.A.1.

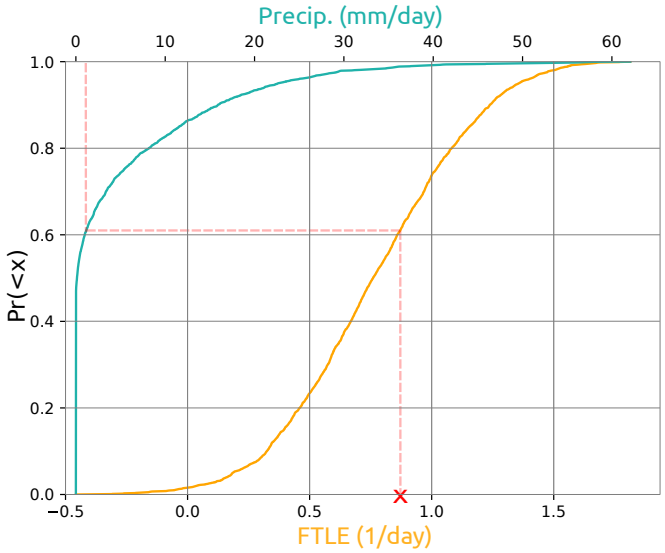

Figure 4.1: Look-up process to determine the FTLE threshold σ' based on a precipitation event of $1\frac{mm}{day}$. The orange and light green curves represent respectively the CDFs of the FTLEs and precipitation at the grid-box closest to São Paulo, Brazil ($-23.5°$S, $-46.5°$N). The dashed red lines illustrate the transformation of the 1 mm/day precipitation threshold into an FTLE threshold via the comparison of the respective CDFs.

The threshold of $P > 1$ mm/day is chosen to define precipitation events in order to avoid the drizzle problem in climate models; i.e., CMIP6 models precipitate very small amounts too frequently (Chen et al. 2021). Catto et al. 2015 finds that employing this threshold brings the ratio of rainy days in models closer to the satellite estimates. Therefore, precipitation amounts below 1 mm/day are set to zero.

Figure 4.2 illustrates the procedure with the observational datasets on a particular day. Fig. 4.2a shows the FTLE and the contours where the FTLE exceeds σ' (i.e., the CZ mask). Fig. 4.2b shows GPCP precipitation on the same date and the precipitation contours that overlap with the CZ mask. All precipitation enclosed by the red contours in Fig. 4.2b is assigned to convergence zones. Similar masking procedures have been used with other process-based diagnostics to

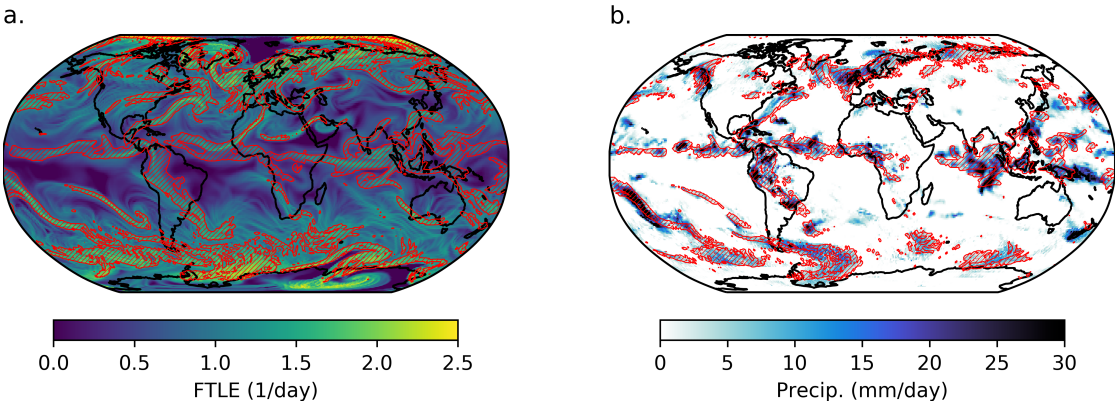

Figure 4.2: Example of the methodology to attribute precipitation to CZs on 16/10/1996. (a) FTLE and CZ mask (red contours); the FTLE was computed using the 5th generation of the ECMWF atmospheric reanalysis (ERA5). (b) Global Precipitation Climatology Project 1° daily precipitation analysis (GPCP-1DD) precipitation on the same date; the red contours show where precipitation overlaps with the CZ mask.

assess the contributions of fronts (Catto et al. 2015) and tropical cyclones (Guo et al. 2017; Franco-Diaz et al. 2019) to the hydrological cycle. A key difference between our CZ mask and the one employed in Weller et al. 2017 is the width or shape of our contours is variable because it depends on the FTLE values, whilst Weller et al. 2017 mask precipitation within a fixed 2° distance of the Eulerian convergence lines.

4.4 Decomposition of precipitation error

We break down the precipitation errors associated with CZ and non-CZ events in terms of errors in frequency and intensity of precipitation. To this end, we employ the same bias decomposition approach employed by Catto et al. 2013, Catto et al. 2015 and Hawcroft et al. 2016 to assess frontal precipitation errors. Please refer to Catto et al. 2015 for a more detailed explanation of this decomposition.

The precipitation error E_P can be written as a sum of the precipitation error

during CZ events (E_{CZ}) and non-CZ events (E_{nCZ}):

$$E_P = E_{\mathrm{CZ}} + E_{\mathrm{nCZ}} \tag{4.2}$$

E_{CZ} and E_{nCZ} can be further decomposed in terms of frequency (ΔF_{CZ}, ΔF_{nCZ}) and intensity (ΔI_{CZ}, ΔI_{nCZ}) errors, where Δ denotes the difference between model and observation estimates. The first terms in the right hand side (RHS) of Eqs. 4.3 and 4.4 are the errors in frequency of CZ and non-CZ multiplied by the intensity of these events in observations ($I_{\mathrm{CZ,o}}$ and $I_{\mathrm{nCZ,o}}$ respectively). The second terms in the RHS of Eqs. 4.3 and 4.4 are the intensity errors of precipitation during CZ and non-CZ events multiplied by the average frequency of these events in observations ($F_{\mathrm{CZ,o}}$ and $F_{\mathrm{nCZ,o}}$). The last terms in the RHS are the mixed terms of errors in frequency and intensity of precipitation during these events.

$$E_{\mathrm{CZ}} = \Delta F_{\mathrm{CZ}} I_{\mathrm{CZ,\,o}} + F_{\mathrm{CZ,\,o}} \Delta I_{\mathrm{CZ}} + \Delta F_{\mathrm{CZ}} \Delta I_{\mathrm{CZ}} \tag{4.3}$$

$$E_{\mathrm{nCZ}} = \Delta F_{\mathrm{nCZ}} I_{\mathrm{nCZ,o}} + F_{\mathrm{nCZ,o}} \Delta I_{\mathrm{nCZ}} + \Delta F_{\mathrm{nCZ}} \Delta I_{\mathrm{nCZ}} \tag{4.4}$$

4.5 Models and observations

In this study we employ a subset of the Atmospheric Model Intercomparison Project (AMIP) historical simulations submitted to CMIP6. This subset is chosen based on the availability of the 6-hourly outputs required to reproduce the methodology in Perez et al. 2021 and calculate the FTLE. The variables required are the horizontal wind components and water vapour concentration at a mini-

mum of 8 vertical levels. The only simulations that present the required outputs are the ones following the HighResMIP protocol (Haarsma et al. 2016), designed to answer questions related to systematic errors and tackle challenges of water availability (Eyring et al. 2016). A summarised description of these models and an evaluation of their representation of the global hydrological is provided by Vannière et al. 2019.

As a best estimate, we employ the 5^{th} generation of the ECMWF atmospheric reanalysis (ERA5) (Hersbach et al. 2020) to compute the FTLE, similarly to Perez et al. 2021 and Perez et al. 2022. Because precipitation is a forecast variable in ERA5, we employ precipitation estimates from the Global Precipitation Climatology Project 1° daily precipitation analysis (GPCP-1DD) (Huffman et al. 2001) and from the Climate Prediction Center morphing method (CMORPH) (Joyce et al. 2004). The FTLE and precipitation from model and observational datasets are brought to a daily scale and interpolated to a common $1° \times 1°$ lat-lon grid. The time period we analyse in this study is 1996-2014; this range is limited by the first date available in GPCP-1DD and the final date in the CMIP6 present-climate simulations forced with observed sea surface temperatures (SSTs). Table 1 lists the simulations and observational datasets and their characteristics.

Table 4.1: CMIP6 present-climate simluations and observational datasets employed in this study. The spatial resolution is presented as an approximation of the lat-lon grid spacing at the equator.

Dataset	Members	Period	Coverage	Resolution	Type
EC-Earth3P	3	1950 - 2014	Global	100 km	AMIP
EC-Earth3P-HR	2	1950 - 2014	Global	50 km	AMIP
ECMWF-IFS-HR	2	1950 - 2014	Global	25 km	AMIP
CNRM-CM6-1	1	1950 - 2014	Global	250 km	AMIP
CNRM-CM6-1-HR	1	1950 - 2014	Global	50 km	AMIP
ERA5	1	1950 - present	Global	30 km	Reanalysis
GPCP 1DD	1	1996 - present	Global	100 km	Satellite-related
CMORPH	1	2002 - present	60°S - 60°N	30 km	Satellite-related

4.6 Contribution of CZ precipitation to total precipitation

4.6.1 Contribution in observations

Figure 4.1 shows the mean GPCP-1DD precipitation (Fig. 4.1a), the contributions of CZ (Fig. 4.1b) and non-CZ (Fig. 4.1c) events identified using ERA5 winds to the mean precipitation and the fraction of total precipitation associated with CZ events. In the regions where precipitation is higher (Fig. 4.1a), such as the ITCZ, subtropical convergence zones and regions dominated by fronts, over 50% of the accumulated precipitation falls over CZs (Fig. 4.1c). In dry regions, such as the subtropical highs and deserts, the contribution of CZs is typically below 10%. In a global average, approximately 53% of precipitation falls during CZ events when GPCP precipitation is considered. Between 60°S - 60°N, the estimated contribution of CZs to global precipitation is approx. 54% using GPCP, 51% using CMORPH and 67% using ERA5 data. Spatial maps showing the contribution of

CZs to total precipitation using CMORPH and ERA5 precipitation data can be found in the Appendix.

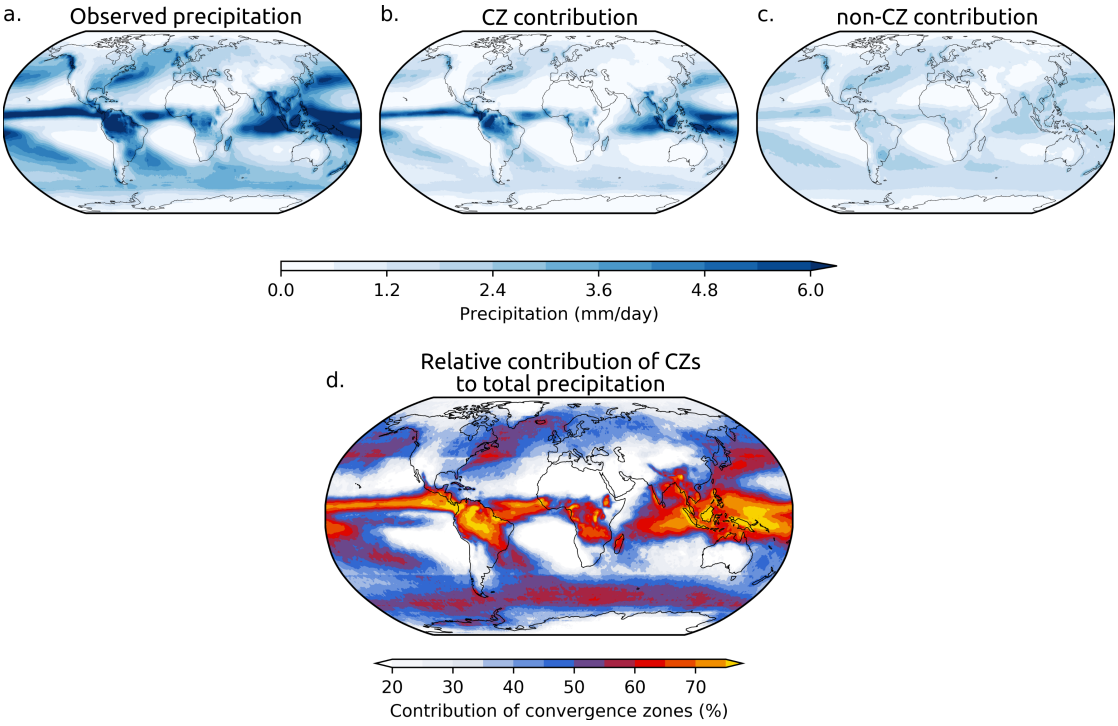

Figure 4.1: Mean GPCP-1DD precipitation (a), contribution of CZ (b) and non-CZ events (c) to the mean precipitation. (d) Fraction of the total precipitation allocated to CZs (i.e., the ratio between subplots "b" and "c").

Figure 4.2 shows the contribution of CZs to the total precipitation grouped by season (DJF, MAM, JJA and SON) using GPCP-1DD precipitation data. In the equatorial region, contours above 70% reveal the seasonal migration of the ITCZ. In DJF, over 70% of precipitation in the monsoon regions in South America and South Africa falls during CZ events; these regions are known to be affected by the migrations of the ITCZ and the occurrence of the South Atlantic Convergence Zone (SACZ) and South Indian Convergence Zone (SICZ). Still in DJF, we note that over 60% of precipitation in the South Pacific Convergence Zone (SPCZ) and the North Atlantic storm-track falls during CZ events. In MAM and JJA, we

highlight the 60% contour close to Japan, marking the region of the Baiu front, a subtropical convergence zone with similar characteristics to the SACZ and the SPCZ (Kodama 1992). In JJA we notice that over 70% of precipitation falls during CZ events in parts of southeast Asia. Also noticeable in all seasons except MAM is the 60% contour along the East Coast of the United States of America; this contour roughly overlaps with the low-level atmospheric convergence generated by the Gulf stream (Kuwano-Yoshida et al. 2010).

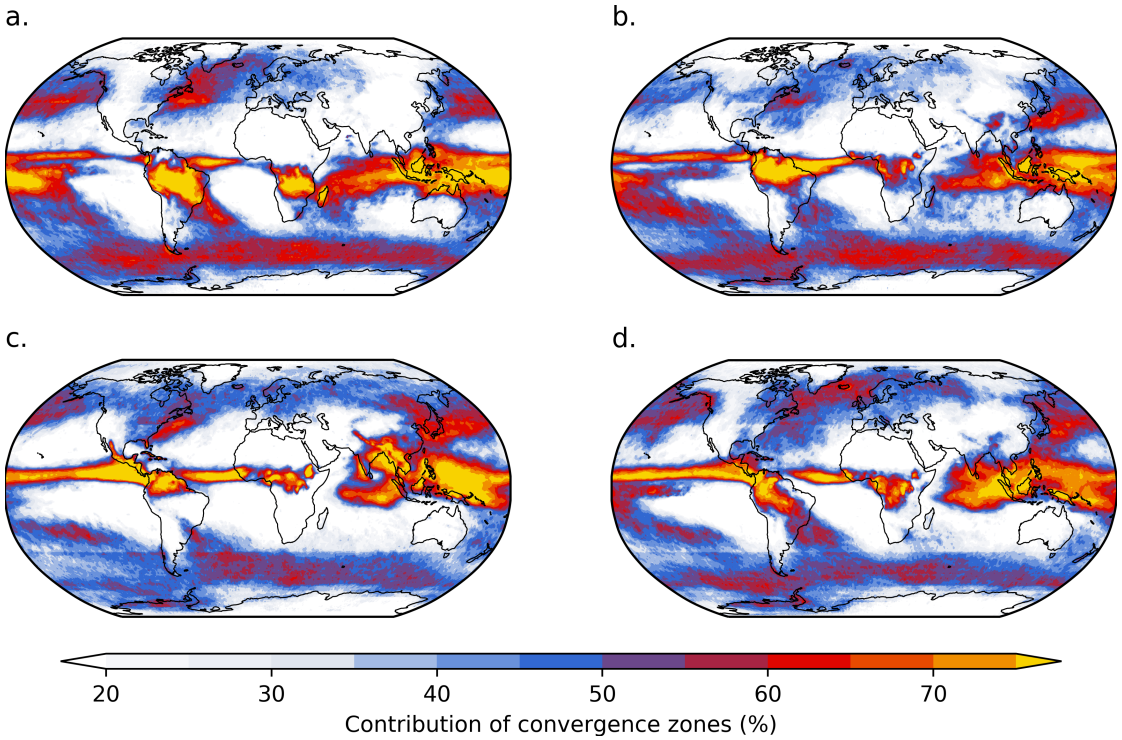

Figure 4.2: Fraction of total GPCP-1DD precipitation allocated to CZs identified using ERA5 winds in DJF (a), MAM (b), JJA (c) and SON (d).

We expect uncertainties in the estimated CZ contrbibution to originate from the observational limitations of precipitation products rather than from the FTLE. This is expected because (i) the FTLE is derived from large-scale reanalysis wind and (ii) the formation of tracer filaments is robust to errors in the wind field

(Methven and Hoskins 1999). A first estimate of uncertainty can be achieved by comparing the CZ contribution in GPCP (54%) versus CMORPH (51%): the difference between the estimates of the two products is 3%. A more robust assessment of uncertainty could be achieved by using other observational precipitation products.

4.6.2 Contribution in climate models

Figure 4.3 shows the apportionment of precipitation to CZ and non-CZ events in CMIP6 simulations compared with the observational estimates (i.e., convergence zones found with ERA5 winds and assigned precipitation from GPCP-1DD, CMORPH and ERA5). When compared to GPCP-1DD and CMORPH estimates, all climate models allocate more precipitation to CZ events (Fig. 4.3a) and less precipitation to non-CZ events (Fig. 4.3b). This results in a higher relative contribution of CZ precipitation than expected from observations (Fig. 4.3c). We highlight that the precipitation apportionment to CZs in CNRM-CM6-1 and CNRM-CM6-1-HR is closer to the GPCP-1DD and CMORPH estimates than the other models. The apportionment using ERA5 precipitation is closer to the climate models than to GPCP-1DD and CMORPH, which is expected considering that precipitation is a forecast variable in reanalyses.

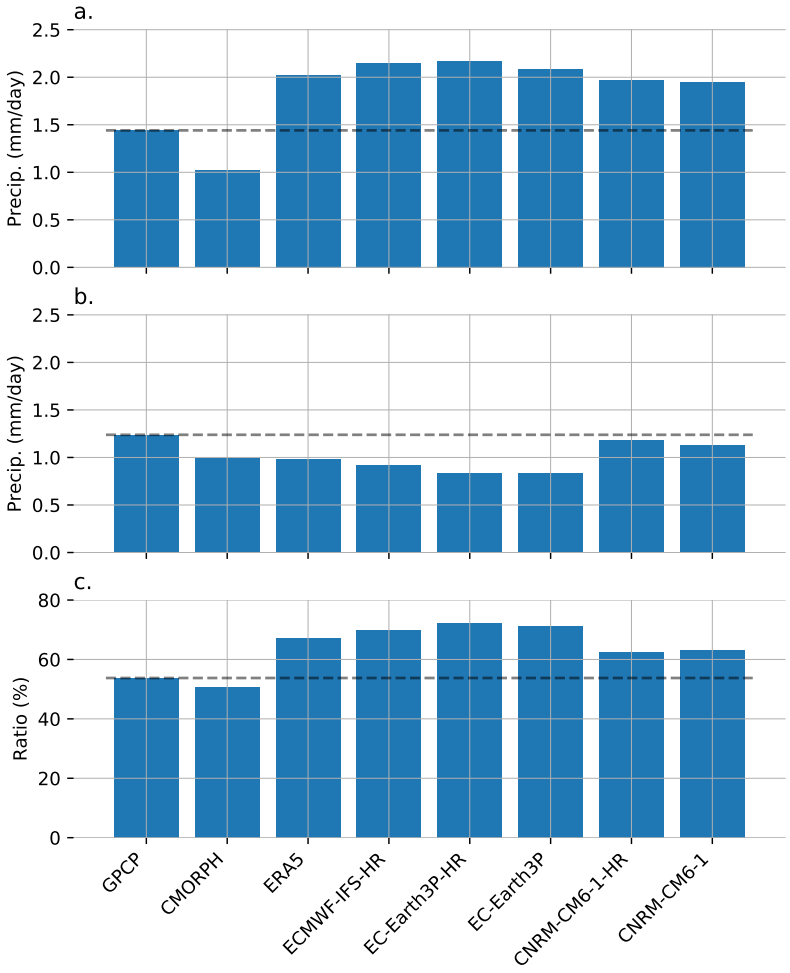

Figure 4.3: Contribution to the precipitation mean of: CZ events (a) and non-CZ events (b). Relative contribution of CZ precipitation to the total precipitation (c). The horizontal dashed line is marking GPCP-1DD estimate for comparison. The domain considered here is limited between 60°S and 60°N due to CMORPH's spatial coverage. Differences between simulations using the same model are negligible (three orders of magnitude smaller than the values presented), therefore, the ensemble mean is shown for the EC-Earth3P, EC-Earth3P-HR and ECMWF-IFS-HR.

Figure 4.4 shows the percentual bias, averaged among models, of the contribution of CZs to precipitation when compared to the GPCP-1DD estimates. On average, climate models assign more precipitation to CZs especially in the tropics and some storm-track regions (e.g., North Atlantic and southern Indian). Around the Pacific ITCZ, we notice positive percentual biases higher than 25%; this is the

region where the systematic double-ITCZ bias occurs in CMIP6 models (Tian and Dong 2020). In the equatorial Atlantic, biases greater than 25% also coincide with displacement errors in the simulation of the Atlantic ITCZ (Richter and Tokinaga 2020). Negative biases are found over the Eurasian continent, the equatorial eastern Pacific, and along the southern coast of Argentina. To further investigate the sources of precipitaton biases, the next section presents the error decomposition in terms of frequency and intensity of CZ and non-CZ precipitation.

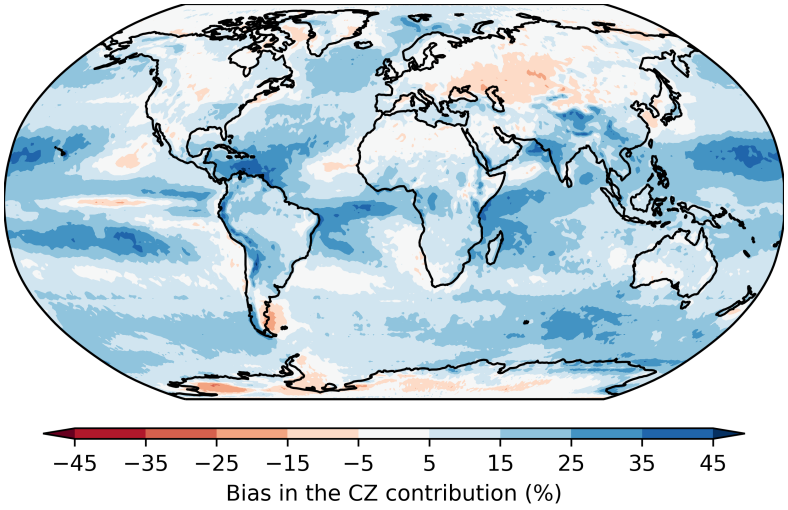

Figure 4.4: Percentual bias, averaged across models, of the contribution CZ events to the precipitation mean. The bias of each climate model is obtained by comparing it with estimates using ERA5 CZs and GPCP-1DD precipitation.

4.6.3 Decomposition of frequency and intensity precipitation biases

Figure 4.A.5 shows the average across models of the error terms on the RHS of Equations 4.3 and 4.4; the observational reference is obtained from CZs found using ERA5 winds and precipitation from GPCP-1DD. We first notice that the largest biases come from the frequency terms (ΔF): CZ precipitation shows pre-

dominantly positive biases (term $\Delta F_{\mathrm{CZ}} \times I_{\mathrm{CZ,o}}$) while non-CZ precipitation biases are predominantly negative (term $\Delta F_{\mathrm{nCZ}} \times I_{\mathrm{nCZ,o}}$). We highlight the signature of the double-ITCZ bias in the CZ term ($\Delta F_{\mathrm{CZ}} \times I_{\mathrm{CZ,o}}$). The biases associated with intensity errors (ΔI) present both positive and negative values; we highlight a positive bias along the northeastern coast of South America in both the CZ and non-CZ terms. One of the strongest errors in the intensity of non-CZ precipitation ($\Delta I_{\mathrm{nCZ}} \times F_{\mathrm{nCZ,o}}$) is in the region dominated by mesoscale convective complexess (MCCs) in southern South America (Durkee et al. 2009). MCCs are driven by the vertical shear between the low-level jet along the Andes and the subtropical jet; they are indeed not expected to be caused by CZs. The magnitudes of the biases in the mixed terms ($\Delta I_{\mathrm{CZ}} \times \Delta F_{\mathrm{CZ}}$ and $\Delta I_{\mathrm{nCZ}} \times \Delta F_{\mathrm{nCZ}}$) are much smaller than the other terms. The error terms aggregated by season can be found in the Appendix.

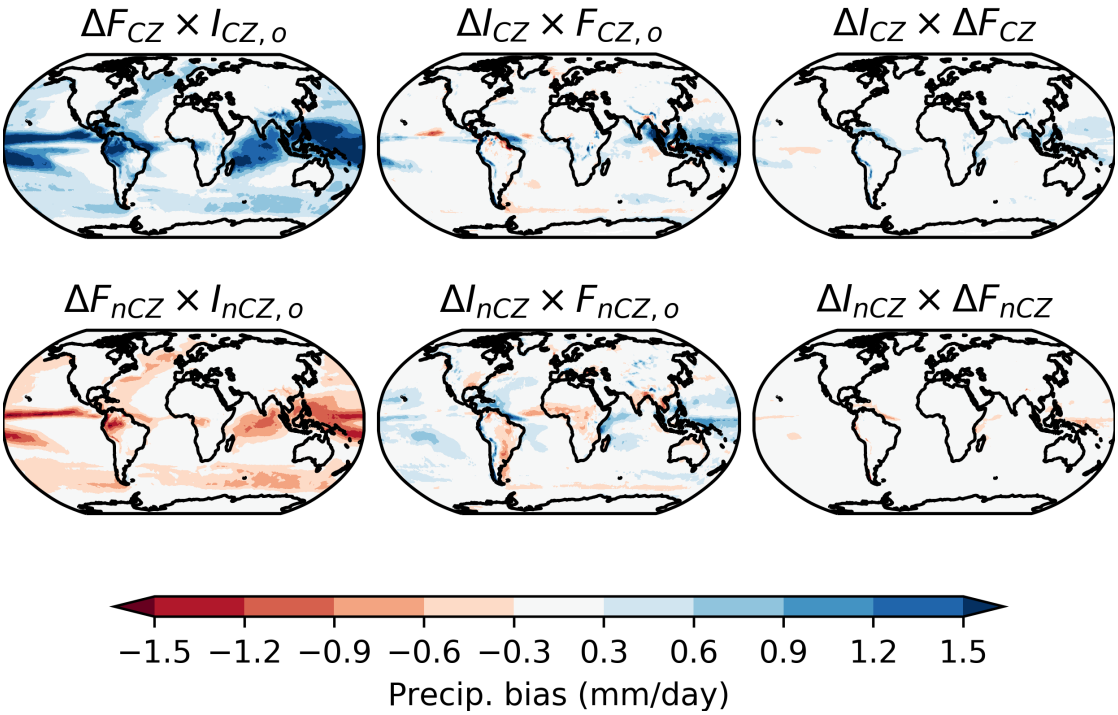

Figure 4.5: Decomposition of the precipitation biases in terms of frequency (ΔF) and intensity (ΔI) for CZ and non-CZ events. Each term represents the average of the CMIP6 simulations employed here. See Section 4.4 for details.

Figure 4.6 aggregates all the terms on the RHS of Eqs. 4.3 and 4.4 to compose the CZ and non-CZ precipitation errors (E_{CZ} and E_{nCZ}) in DJF and JJA. In both seasons, E_{CZ} is predominantly positive while E_{nCZ} is predominantly negative. In JJA we notice a strong negative bias in the Atlantic ITCZ sided by a positive biase along the northeastern coast of South America, indicating an error in the position of the ITCZ. In the DJF North Atlantic and the JJA South Indian, storm-track regions present positive precipitation biases during CZ events and negative biases during non-CZ events. We also highlight the strong diagonal positive bias of CZ precipitation in the South Pacific in DJF, indicating that climate models exaggerate the SPCZ precipitation.

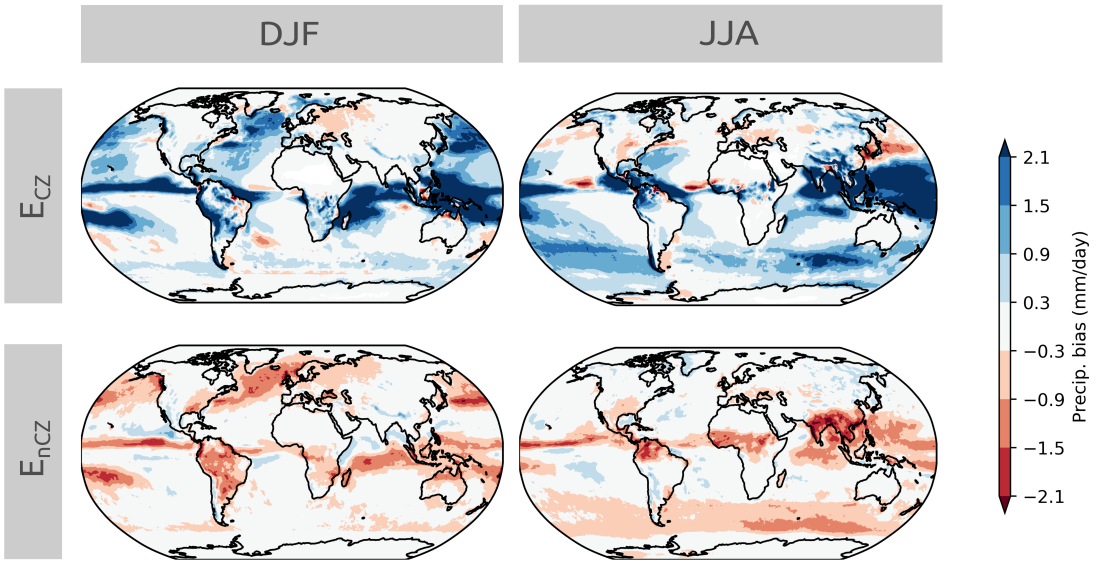

Figure 4.6: Precipitation errors associated with CZ (E_{CZ}) and non-CZ events (E_{nCZ}) averaged across all simulations.

We can average the error terms spatially to see how they vary across simulations (Fig. 4.7). We notice that, in all simulations, the error in CZ precipitation is dominated by positive frequency biases. In terms of non-CZ precipitation, all simulations present negative frequency biases. The mixed terms ($\Delta F \Delta I$) remain small for both CZ and non-CZ precipitation. We highlight that CNRM-CM6 presents a smaller bias in the frequency of CZ and non-CZ precipitation (although its intensity bias is higher); this helps explaining the better representation of the apportionment of CZ precipitation in that model (see Fig. 4.3). However, the smaller frequency bias of that model could be caused by cancellation of positive and negative biases in the spatial averaging. To remove the possibility of spatial cancellation, Figure 4.8 shows the spatial average of the absolute value of the bias components. We notice that the CNRM-CM6 simulations indeed present an smaller frequency errors, but the intensity errors are larger than in the other

models.

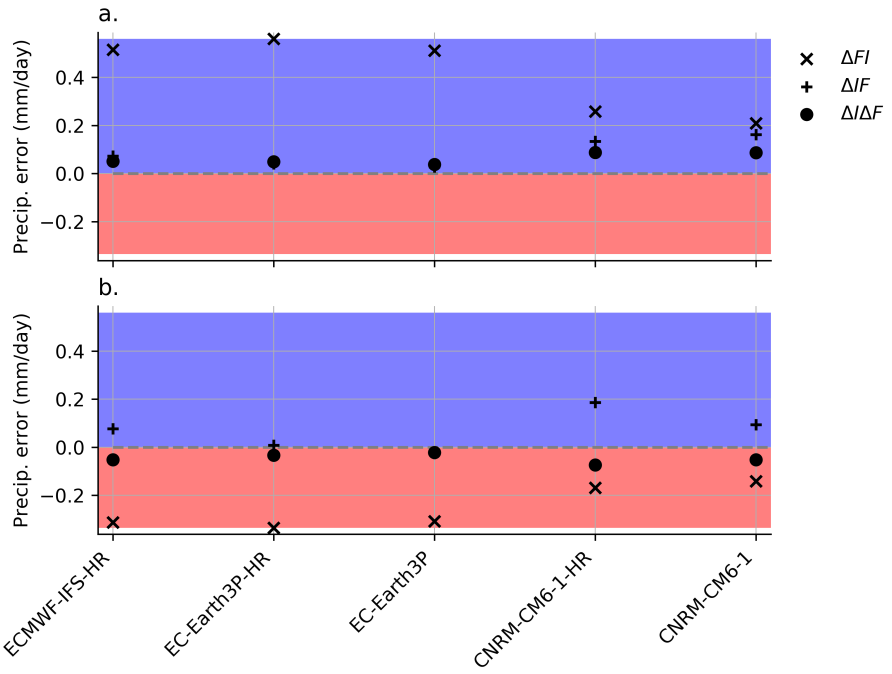

Figure 4.7: Spatial average of the model precipitation bias for CZ events (a) and non-CZ events (b).

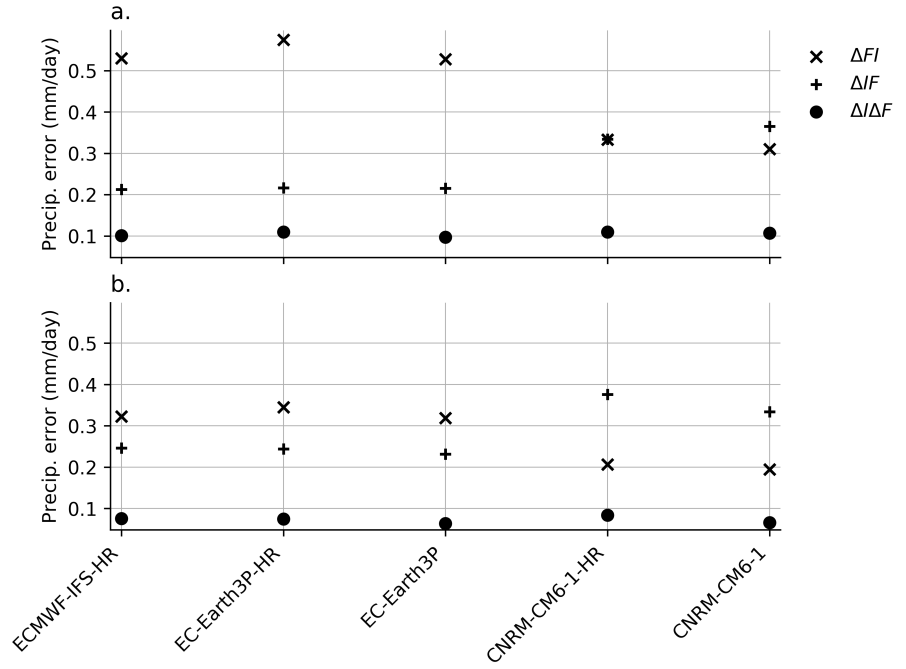

Figure 4.8: Spatial average of the absolute model precipitation bias for CZ events (a) and non-CZ events (b).

4.7 Conclusion

In this chapter we quantify the contribution of convergence zones (CZs) to precipitation by employing an objective diagnostic based on the degree of mixing of the synoptic-scale horizontal flow. We find that approximately 54% of global precipitation falls during convergence zone events. This quantification is enabled by the recent developments in Perez et al. 2021 and Perez et al. 2022, who adapted a Lagrangian framework to identify atmospheric structures where the flow kinematics favours the accumulation of moisture. To the best of our knowledge, the only other similar global quantification of CZ precipitation is presented in Weller et al. 2017. There are two key distinctions between their methodology and the one employed here: (i) the convergence lines in Weller et al. 2017 are identified with an Eulerian

diagnostic applied over a 6-hourly wind field, whilst here we employ a Lagrangian diagnostic calculated over 2-day trajectories to focus on synoptic-scale processes and (ii) Weller et al. 2017 ascribe precipitation to convergence lines based on a fixed-distance mask of 2° on a lat-lon grid; in our case, the shape of our CZ mask is variable and based only on the FTLE value. Nonetheless, over oceanic regions our apportionment of precipitation to CZs and their apportionment to convergence lines is similar; over land, however, our CZ precipitation features are smoother. We expect this to be the case because the low-level flow over the ocean is typically steadier, leading to a better agreement between Lagrangian and Eulerian diagnostics.

When evaluating AMIP simulations submitted to CMIP6, we find that climate models overestimate the ratio of the total precipitation that falls during CZ events: observations suggest 54% (GPCP-1DD) and 51% (CMORPH) while all climate models and ERA5 present a ratio above 60%; CNRM-CM6-1 and CNRM-CM6-1-HR present the ratio closest to the observations. All climate models analysed here perform poorly at conserving moisture (Vannière et al. 2019), with the exception of CNRM-CM6-1 and CNRM-CM6-1-HR that nearly close the water budget (Fig. 9h in Vannière et al. 2019) due to a mass conserving procedure applied at every time step to the semi-Lagrangian advection scheme (Voldoire et al. 2013). In, EC-Earth3P, for example, global precipitation exceeds evaporation by approx. 0.1 mm/day (derived from Fig. 9h in Vannière et al. 2019). This excess of precipitation due to non-conservative advection schemes could be amplified in regions of high mixing where horizontal gradients tend to be sharper; Dacre 2010 shows that Met Office Unified Model overpredicts tracer concentration due to a non-conservative advection scheme, an issue that is more pronounced in

regions where concentration gradients are sharper. Therefore, the improved mass advection scheme in CNRM-CM6-1 and CNRM-CM6-1-HR models may partly explain why these models allocate precipitation to high mixing events (CZs) in a proportion that is closer to observations than the other climate models.

We also show that the largest contribution to the precipitation error comes from a positive bias in the frequency of CZ precipitation. In other words, models trigger precipitation too frequently in situations of high mixing. This could be due to an exaggerated response of the convective parameterizations to the horizontal strain and accumulation of moisture in regions of high mixing. Indeed, some classes of climate models appear to underestimate the convective inhibition energy (Brockhaus et al. 2008), a problem that could potentially be alleviated in convection permitting simulations (Fosser et al. 2015). We also show that the persistent double-ITCZ bias (Tian and Dong 2020) appears in the frequency of CZ precipitation.

The subset of simulations analysed here is limited to those under the HighResMIP protocol due to the availability of 6-hourly winds and specific humidity outputs. To enable the reproduction of this diagnostic in a wider range of models, we recommend that future AMIP submissions output the required variables on at least 8 vertical levels. Alternativelly, 6-hourly outputs of the vertically integrated moisture flux and the total column water vapour can also be employed (Perez et al. 2021).

Appendix

4.A Supplementary figures

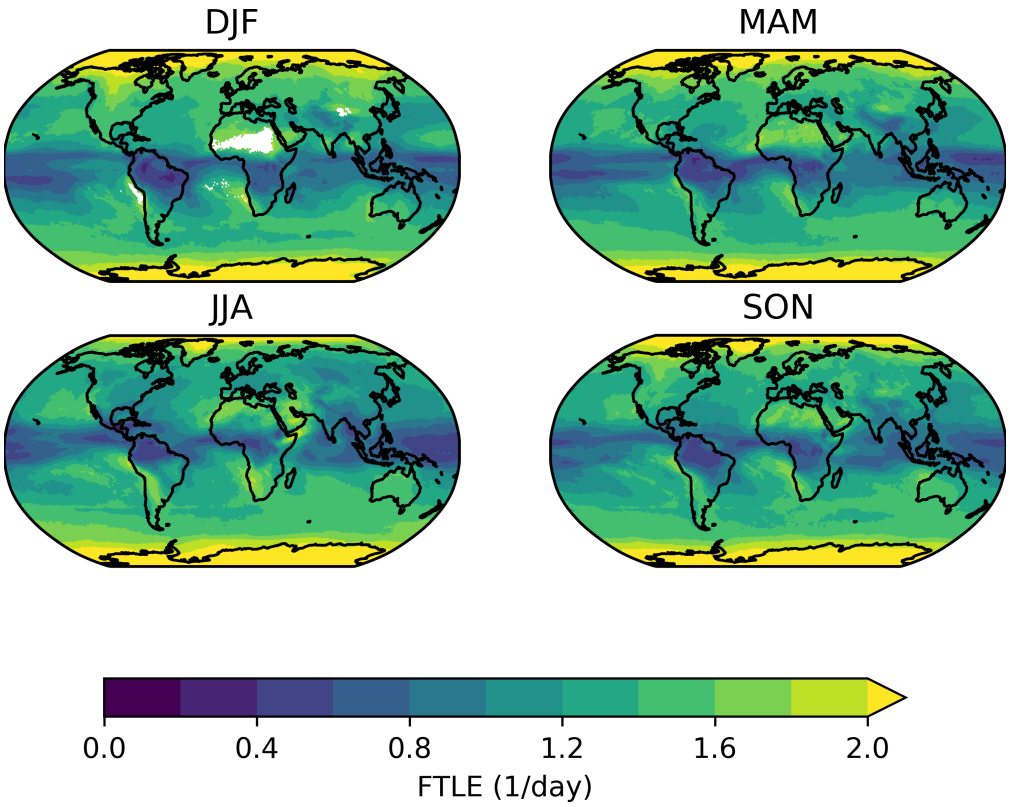

Figure 4.A.1: Finite-Time Lyapunov Exponent (FTLE) values derived from ERA5 winds employed as a threshold to mask precipitation associated with convergence zones. The FTLE value in each grid-box is as frequent as a precipitation event of 1 mm/day in that location using Global Precipitation Climatology Project (GPCP) precipitation. Grid-boxes with no occurrence of precipitation events greater than 1 mm/day are white. The thresholds are calculated per season to account for the seasonal dependence of the FTLE/precipitation relationship revealed in the third chapter of this thesis.

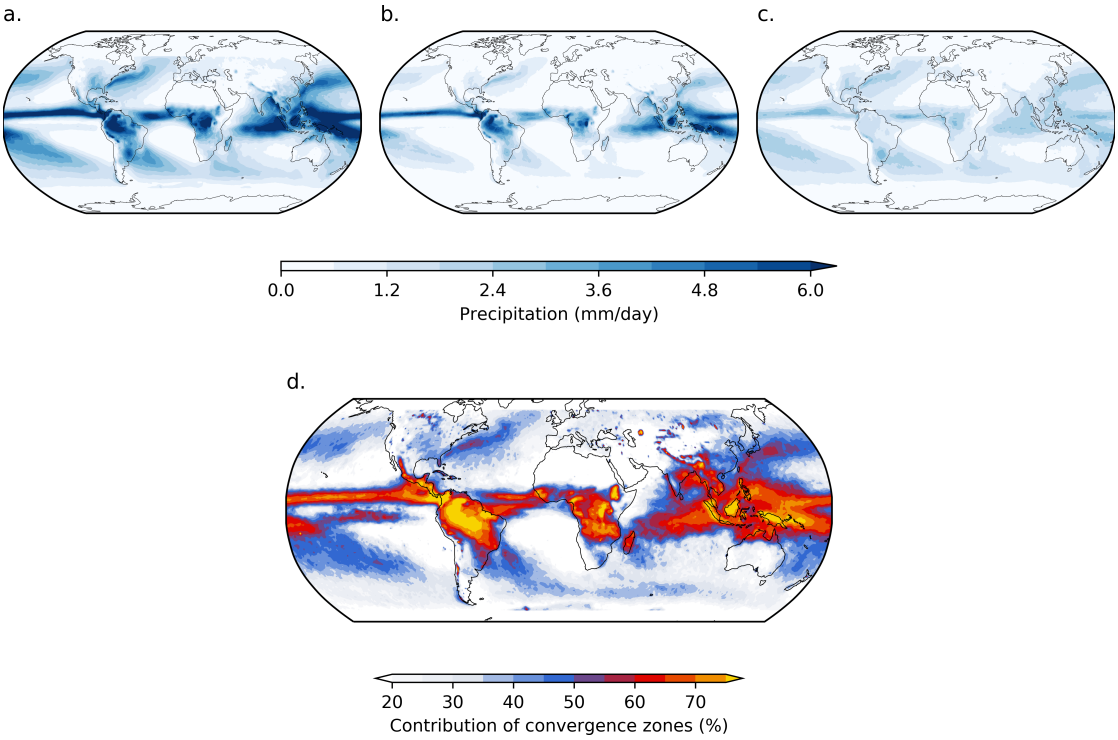

Figure 4.A.2: Mean CMORPH precipitation (a), contribution of CZ (b) and non-CZ events (c) to the mean precipitation. (d) Fraction of the total precipitation allocated to CZs (i.e., the ratio between subplots "b" and "c").

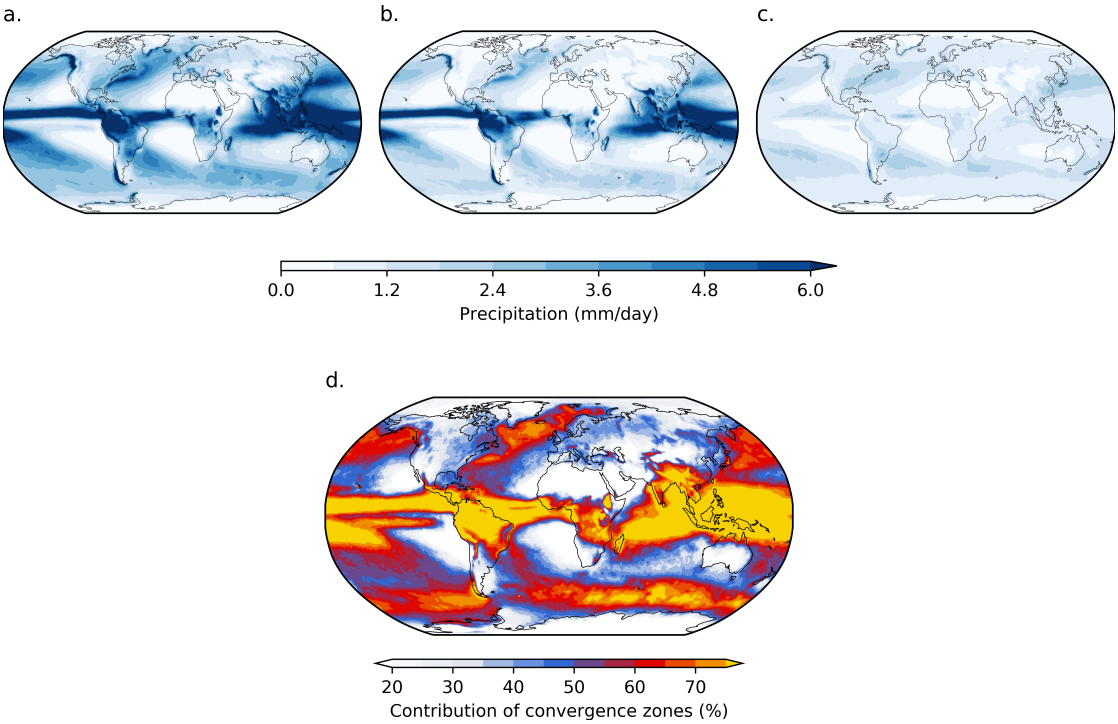

Figure 4.A.3: Mean ERA5 precipitation (a), contribution of CZ (b) and non-CZ events (c) to the mean precipitation. (d) Fraction of the total precipitation allocated to CZs (i.e., the ratio between subplots "b" and "c").

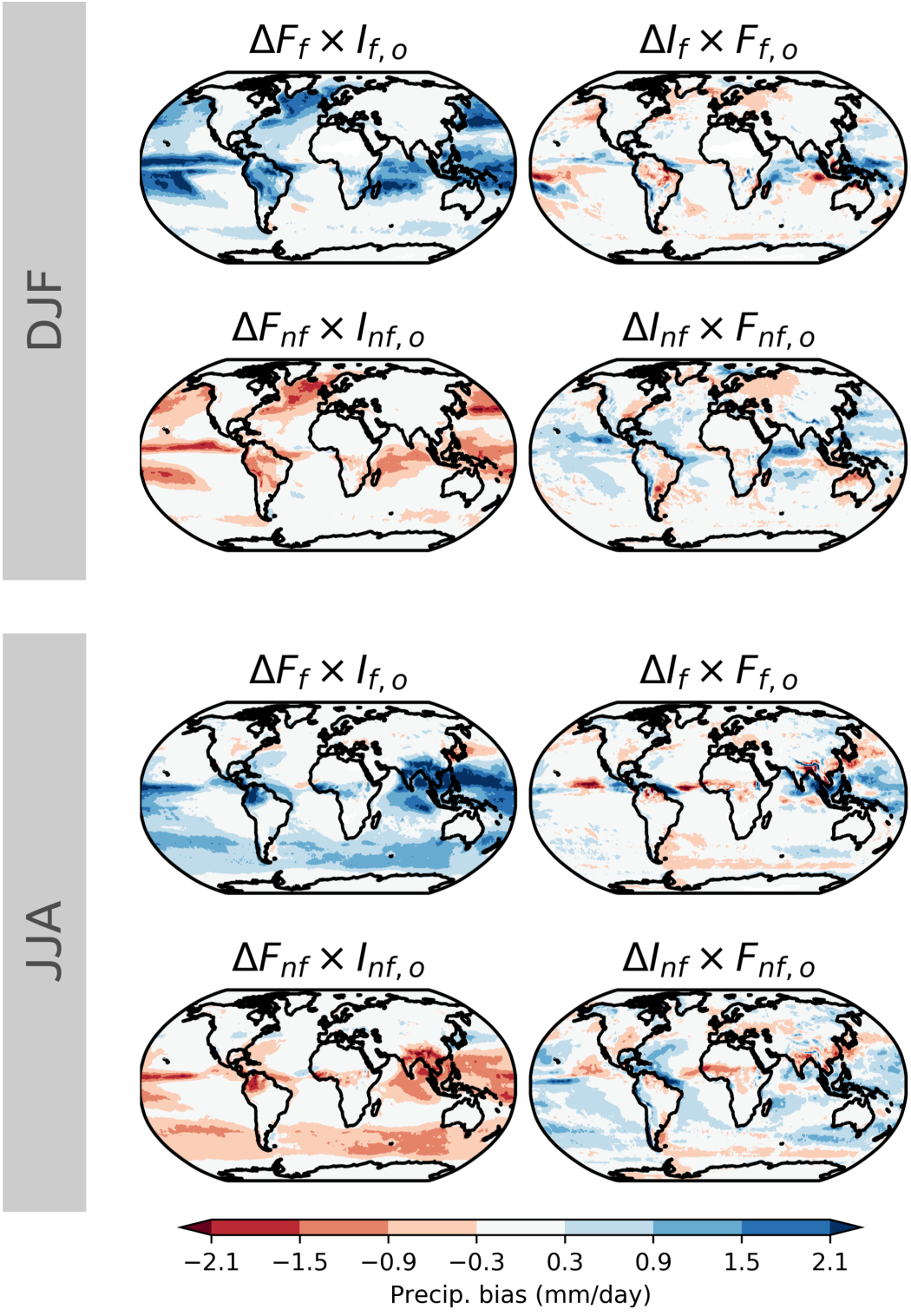

Figure 4.A.4: Decomposition of the precipitation biases in terms of frequency (ΔF) and intensity (ΔI) for CZ and non-CZ events in DJF and JJA. Each term represents the average of the CMIP6 simulations employed here. See Section 4.4 for details.

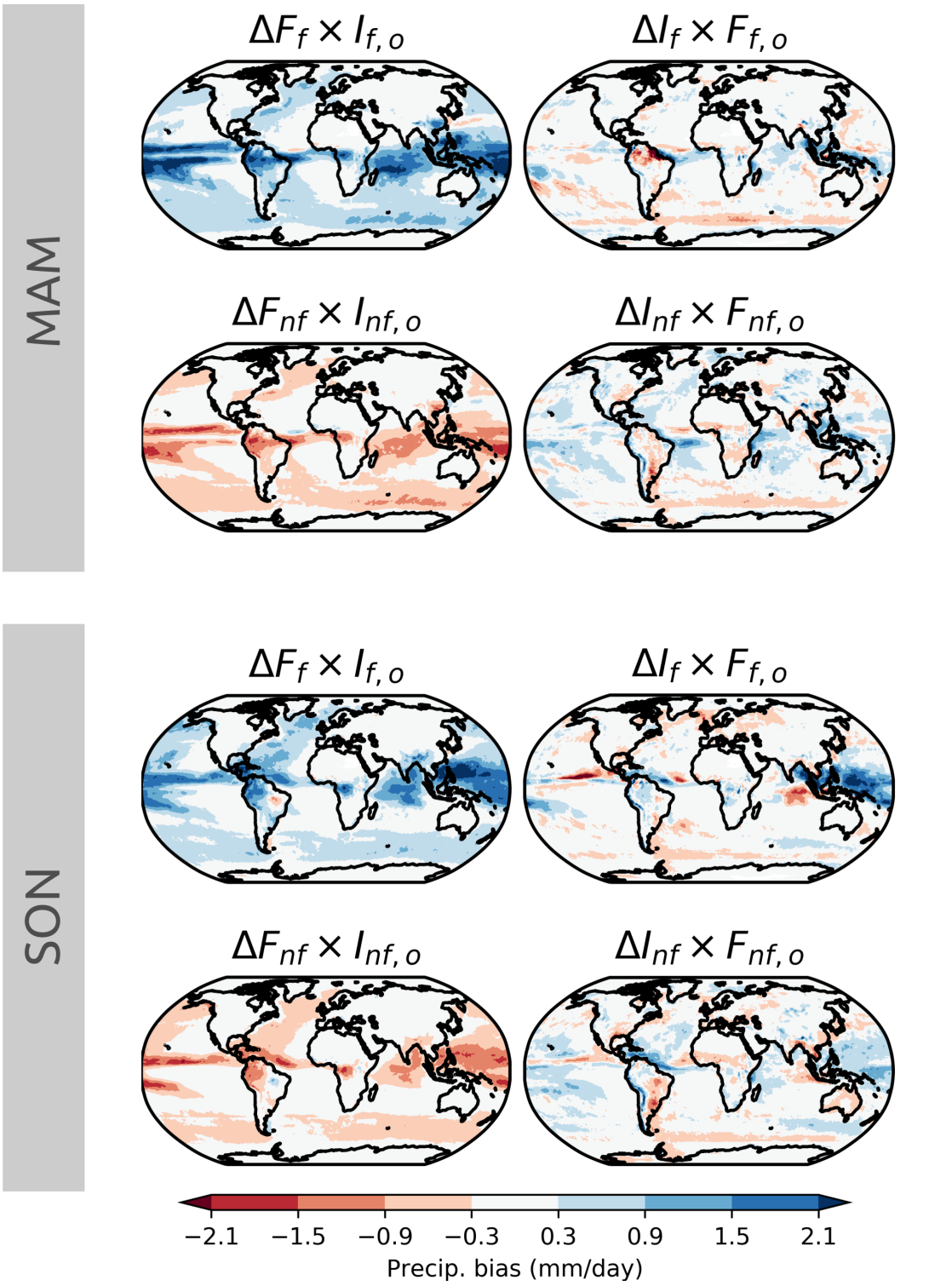

Figure 4.A.5: Decomposition of the precipitation biases in terms of frequency (ΔF) and intensity (ΔI) for CZ and non-CZ events in MAM and SON. Each term represents the average of the CMIP6 simulations employed here. See Section 4.4 for details.

Chapter 5

Conclusion

5.1 Where this thesis places itself?

Concepts of mixing have been used to describe meteorological phenomena (Simpson 1947) and investigate the evolution of turbulence (Welander 1955) for over half a century now. However, the development of a Lagrangian framework to quantify mixing only surged after a seminal paper by Aref 1984, that linked the emergence of complex tracer filaments to the chaotic particle trajectories present even in simple 2-D flows, coining the term "chaotic advection". Julio Ottino compiled the kinematical tools to quantify mixing in their 1989 book, where they describe mixing as follows: "mixing is stretching and folding, and stretching and folding is the fingerprint of chaos". The Lyapunov exponent, a measure of chaos in dynamical systems, was adapted to non-periodic planetary flows and termed Finite-Time Lyapunov Exponent (FTLE) by Pierrehumbert 1991. The FTLE was then employed to characterise airstream boundaries in frontal regions (Cohen and Kreitzberg 1997) and to investigate tracer transport in the mesosphere and strato-

sphere (Shepherd et al. 2000). In the 2000s, ridges of the FTLE were employed to give a precise definition to Lagrangian Coherent Structures (LCSs) (Haller 2001; Shadden et al. 2005). More recently, Garaboa-Paz et al. 2015 and Garaboa-Paz et al. 2017 employed FTLE ridges to identify LCSs underlying atmospheric rivers.

Despite the long history of the mixing framework, meteorological applications are still scarce and climatological studies linking mixing and LCSs to precipitation were not available. In this thesis, I presented three pieces of work that adapted this framework to investigate synoptic-scale mixing features underlying precipitation and answer the scientific questions in Section 1.4. In the next section, I summarise the main findings of this thesis and their implications.

5.2 Summary of contributions and implications

The first piece of work (Chapter 2) establishes via a case study and a 30-year climatology in South America, that LCSs reveal the kinematical skeletons underlying the South Atlantic Convergence Zone (SACZ) and the Intertropical Convergence Zone (ITCZ). Consistent with the SACZ literature (Van Der Wiel et al. 2015; Zilli and Hart 2021), this study also finds that the occurrence of LCSs in Southeast Brazil is associated with the propagation of Rossby wave trains and diagonal rainfall anomalies ranging from the central South America to the South Atlantic. Moreover, it is shown that the FTLE is significantly correlated with daily precipitation and total column water vapour especially, in the SACZ and ITCZ regions. This study aims to answer **SQ1** (see Section 1.4); it confirms the theoretical expectation that attracting LCSs can organise moisture and precipitation bands, reshaping and enhancing existing contrasts of moisture between the Amazon and

southern South America through horizontal advection. This expands the association of FTLE ridges with mechanisms of precipitation in the mid-latitudes (Cohen and Kreitzberg 1997; Garaboa-Paz et al. 2015) to a tropical region, indicating the potential of the method to be applied in a globally.

Chapter 3 presents the first 30-year global climatology of FTLE and LCSs. It is shown that regions of high mixing and high LCS occurrence correspond with many well-known large-scale precipitation features. It is also shown that regions of high mixing are more likely to have higher precipitation averages than regions of low mixing. The temporal relationships between mixing and precipitation are explored through monthly-mean correlations and composites of the FTLE and precipitation during El-Niño, Madden-Julian Oscillation (MJO) and North Atlantic Oscillation (NAO) events. In the case of the NAO, it is shown that the method is capable of disentangling the role of horizontal kinematics in a poorly understood inter-hemispheric teleconnection. Monthly-mean correlation maps (computed via grid-box linear regressions and partial least squares) show that the mixing explains a substantial fraction of the precipitation variability, particularly in tropical and subtropical regions (between 40-80%), answering **SQ2**. The climatological analyses in Chapter 3 complements Chapter 2 by answering **SQ1** in a global domain. The main implications of this chapter are: (i) from a technical point of view, to confirm the feasibility of global climatologies of FTLE and FTLE ridges and (ii) the indication that the method could be used as an automated detection of CZs due to the consistency of the spatio-temporal analyses presented here with the existing CZ literature.

Chapter 4 presents an automated method to detect CZs and assign precipitation to these events. The method is applied to a set of climate models and

observational datasets. This is achieved by an adaptation of the mixing diagnostic presented in Chapters 2 and 3 that allows the attribution of precipitation to CZ events through the definition of a spatial mask. It is found that all of the examined simulations exaggerate the contribution of CZs to total precipitation. In two observational estimates, 51% and 54% of the global precipitation falls over CZs, while this ratio is higher than 60% in the examined models. The climate model with the ratio closest to the observations applies a mass conserving procedure to its advection scheme. An error decomposition reveals that climate models rain too frequently over CZs and not frequently enough outside CZs; it is suggested that the lack of convective inhibition may be the source of this exaggerated response of precipitation to horizontal mixing. The analyses in this chapter is limited by the availability of CMIP6 models that present the required outputs to calculate the FTLE. A recommendation is made for modelling groups to include these outputs in future CMIP submissions.

5.3 Limitations and future work

Combined, the three pieces of work quantify the association between precipitation and mixing in multiple spatio-temporal scales, bringing out the usefulness of the proposed framework to investigate mechanisms precipitation variability. Nonetheless, this thesis only presents an initial investigation of the mixing/precipitation relationship and important practical and theoretical limitations remain. In the list below, I enumerate the main technical and theoretical limitations while presenting suggestions for future work.

1. Technical aspects

Computational efficiency The approach proposed here is more computationally expensive than usual Eulerian diagnostics. The two computational bottlenecks are: (i) the calculation of Lagrangian trajectories and (ii) the linear algebra operations to extract the LCSs as FTLE ridges. The Python implementation developed in this study (*LagrangianCoherence* library available here) optimises the most expensive routines with Numba's just-in-time compiling (documentation). However, using CEDA's Jasmin batch computing, I found that it is too time consuming to extract LCSs as FTLE ridges in multiple global CMIP6 simulations. However, with a greater uptake from the community, more efficient and parallelised routines can be implemented to mitigate this problem.

High level interface The uptake of the mixing framework by the wide meteorology community is currently hindered by the lack of high level interfaces that allow the quick extraction of mixing diagnostics from atmospheric data. A researcher or a research group interested in this approach would have to invest a considerable amount of time and effort to implement from scratch or adapt trajectory and linear algebra routines. Currently, mixing and LCS diagnostics for atmospheric data are only publicly available in Python in the *LagrangianCoherence* library developed during this thesis. *LagrangianCoherence* still lacks an in-depth documentation and a set of examples so that it can be easily adopted by other research groups. The only similar library is "LCS Tool" (available here). However, it is implemented in MATLAB, a commercial proprietary language, which limits the democratisation of LCS analyses only for research groups with a MATLAB license.

Moreover, from the documentation provided in Onu et al. 2015, it is unclear if LCS Tool supports lat-lon grids and if it performs trajectories and linear algebra operations on spherical coordinates.

2-D trajectories The trajectories used here to quantify mixing are 2-dimensional. A 3-dimensional implementation could possibly reveal different features in situations where a vertically integrated flow cannot reasonably approximate true moisture pathways. A 3-D option is currently being implemented in the *LagrangianCoherence* library, however, it may not be computationally feasible to carry out climatological studies that require the computation of 3-D trajectories for the whole globe and the eigendecomposition of the 3-D deformation tensors that are necessary to extract the FTLE. However, with the optimisation of the routines mentioned above, fully 3-D global climatologies of the FTLE might become feasible. Alternatively, more widely used trajectory softwares, such as LAGRANTO (Sprenger and Wernli 2015), could be adapted to provide the departure points required by the *LagrangianCoherence* library to assemble the Cauchy-Green strain tensor and derive the FTLE.

Data availability The subset of CMIP simulations in which the methodology can be applied is limited. The calculation of trajectories that represent pathways of moisture require at least 6-hourly outputs and eight vertical levels of water vapour and horizontal winds. Currently, only models submitted under the HighResMIP protocol provide the required outputs. This issue can be overcome if climate modelling groups include these outputs in future CMIP submissions.

2. Theoretical aspects

LCS mathematical framework The mathematical theory of LCSs is still under active development (Haller 2015; Balasuriya 2020) and the general validity of transport barriers defined as FTLE ridges has been questioned. For example, Shadden et al. 2005 propose that FTLE ridges approximate truly Lagrangian LCSs because they admit almost zero perpendicular flux (i.e., they are material lines advected by the flow) while Haller 2011 provides examples where the cross-flux is not negligible. Another example of debate can be found between Norgard and Bremer 2012 and Peikert et al. 2013 that disagree about the implications of defining LCSs as second-derivative ridges of the FTLE. Nonetheless, FTLE ridges unequivocally reveal material lines that suffered the most stretching (Allshouse and Peacock 2015) and this has been repeatedly shown to provide important insights about tracer transport in the atmosphere and oceans (Beron-Vera et al. 2008; Waugh et al. 2012; Nolan et al. 2020). Although more modern and complex definitions of LCSs have been proposed (see review in Haller 2015), the practical gains and the computational costs of their application to atmospheric datasets is still unclear. Once more, an increased uptake in the use of mixing diagnostics in the broad meteorology community, combined with a close interaction with the applied mathematics and fluid mechanics community, could advance the field towards a better understanding of, for example, how strict the definition of atmospheric LCSs should be and what are the relevant theoretical limitations of FTLE ridges that we should be cautious about in meteorological applications.

Other types of LCSs In this thesis I presented ridges of the FTLE calculated over trajectories backwards in time. Such ridges approximate "hyperbolic attracting LCSs"; however, other types of exist, such as elliptic, parabolic and repelling hyperbolic LCSs (see review in Haller 2015). Elliptic LCSs could be extracted in atmospheric datasets to identify cyclone cores while parabolic LCSs can identify jet cores (Farazmand et al. 2014). Moreover, simple modifications of the methodology presented in this thesis, such as extending the back-trajectory integration time from 2 days to 10 days could reveal planetary-scale LCSs.

Communicating with diverse communities A number of mixing features discussed in Chapters 2-4 overlap with atmospheric phenomena that are objects of study of diverse scientific communities, such as fronts, studied by the ETC experts, versus the ITCZ, studied by tropical meteorologists. Therefore, it is important to refine how the role of horizontal mixing is communicated so that it does not conflict with the established understanding of specific meteorological phenomena. For example, in this thesis I define CZs purely through mixing, so one might assume that I am arguing that subtropical CZs and the ITCZ are the same type of meteorological object there are important distinctions in terms of mechanisms and impacts. This refinement in communicating what horizontal mixing represent in the context of each meteorological phenomenon can be achieved by more regional or phenomenon-specific studies, in the same spirit of Chapter 2 that focus on South America and the SACZ.

Kinetic spectral slope The slope of the kinetic energy spectrum

determines the nature of tracer transport (Bartello 2000). In particular, if the spectrum is steeper than $E(k) \propto k^{-3}$, the formation of fine-scale tracer filaments will be directed by the large-scale circulation, in a scale cascade regime. The behaviour of tracer transport in the stratosphere is consistent with this scale cascade regime, where the energy spectrum is dominated by Rossby waves and high FTLE filaments are frequent (Shepherd et al. 2000). Consistently, in Chapter 2, it is shown that Rossby wave trains are precursors of LCSs in South America. Therefore, future studies could investigate if model errors in LCS occurrence and FTLE intensity are tied to discrepancies in the kinetic spectral slope between models and observations.

5.3.1 Final remarks

This thesis characterised and quantified the role of synoptic-scale kinematics in controlling the variability of precipitation on Earth through a novel adaptation of the framework of mixing and Lagrangian Coherent Structures. By doing so, it enabled the development of a global convergence zone (CZ) detection algorithm and the automatic attribution of precipitation to CZs, presenting a new phenomena-based precipitation diagnostic to help disentangling sources of errors in models.

Although studies employing similar diagnostics are scarce in the meteorology literature, I hope that the analyses and computational tools presented here motivate and facilitate the uptake of the framework of mixing by atmospheric scientists. Particularly, I hope to have mitigated some barriers to this uptake by (i) clarifying the methodological and implementation details for atmospheric datasets and (ii) translating the language and concepts from the fluid mechanics community into

a discourse that is more accessible for those that, like myself, have a meteorology background.

References

Allshouse, Michael R, and Thomas Peacock. 2015. "Refining finite-time Lyapunov exponent ridges and the challenges of classifying them". *Chaos: An Interdisciplinary Journal of Nonlinear Science* 25 (8): 087410.

Aref, Hassan. 1984. "Stirring by chaotic advection". *Journal of fluid mechanics* 143:1–21.

Balasuriya, Sanjeeva. 2020. "Uncertainty in finite-time Lyapunov exponent computations".

Bartello, Peter. 2000. "Using low-resolution winds to deduce fine structure in tracers". *Atmosphere-Ocean* 38 (2): 303–320.

Beron-Vera, Francisco J, Maria J Olascoaga, and GJ Goni. 2008. "Oceanic mesoscale eddies as revealed by Lagrangian coherent structures". *Geophysical Research Letters* 35 (12).

Cohen, Robert A, and Carl W Kreitzberg. 1997. "Airstream boundaries in numerical weather simulations". *Monthly weather review* 125 (1): 168–183.

Farazmand, Mohammad, Daniel Blazevski, and George Haller. 2014. "Shearless transport barriers in unsteady two-dimensional flows and maps". *Physica D: Nonlinear Phenomena* 278:44–57.

Garaboa-Paz, Daniel, Jorge Eiras-Barca, and Vicente Pérez-Muñuzuri. 2017. "Climatology of Lyapunov exponents: the link between atmospheric rivers and large-scale mixing variability". *Earth System Dynamics* 8 (3): 865–873.

Garaboa-Paz, Daniel, et al. 2015. "Lagrangian coherent structures along atmospheric rivers". *Chaos: An Interdisciplinary Journal of Nonlinear Science* 25 (6): 063105.

Haller, George. 2011. "A variational theory of hyperbolic Lagrangian coherent structures". *Physica D: Nonlinear Phenomena* 240 (7): 574–598.

— . 2001. "Distinguished material surfaces and coherent structures in three-dimensional fluid flows". *Physica D: Nonlinear Phenomena* 149 (4): 248–277.

— . 2015. "Lagrangian coherent structures". *Annu. Rev. Fluid Mech* 47 (1): 137–162.

Nolan, Peter J, Hosein Foroutan, and Shane D Ross. 2020. "Pollution transport patterns obtained through generalized Lagrangian coherent structures". *Atmosphere* 11 (2): 168.

Norgard, Greg, and Peer-Timo Bremer. 2012. "Second derivative ridges are straight lines and the implications for computing Lagrangian coherent structures". *Physica D: Nonlinear Phenomena* 241 (18): 1475–1476.

Onu, Kristjan, Florian Huhn, and George Haller. 2015. "LCS Tool: A computational platform for Lagrangian coherent structures". *Journal of Computational Science* 7:26–36.

Peikert, Ronald, David Günther, and Tino Weinkauf. 2013. "Comment on "Second derivative ridges are straight lines and the implications for computing Lagrangian Coherent Structures, Physica D 2012.05. 006"". *Physica D: Nonlinear Phenomena* 242 (1): 65–66.

Pierrehumbert, RT. 1991. "Large-scale horizontal mixing in planetary atmospheres". *Physics of Fluids A: Fluid Dynamics* 3 (5): 1250–1260.

Shadden, Shawn C, Francois Lekien, and Jerrold E Marsden. 2005. "Definition and properties of Lagrangian coherent structures from finite-time Lyapunov exponents in two-dimensional aperiodic flows". *Physica D: Nonlinear Phenomena* 212 (3-4): 271–304.

Shepherd, Theodore G, John N Koshyk, and Keith Ngan. 2000. "On the nature of large-scale mixing in the stratosphere and mesosphere". *Journal of Geophysical Research: Atmospheres* 105 (D10): 12433–12446.

Simpson, Robert H. 1947. "Synoptic aspects of the intertropical convergence near Central and South America". *Bulletin of the American Meteorological Society* 28 (7): 335–346.

Sprenger, Michael, and Heini Wernli. 2015. "The LAGRANTO Lagrangian analysis tool–version 2.0". *Geoscientific Model Development* 8 (8): 2569–2586.

Van Der Wiel, Karin, et al. 2015. "A dynamical framework for the origin of the diagonal South Pacific and South Atlantic convergence zones". *Quarterly Journal of the Royal Meteorological Society* 141 (691): 1997–2010.

Waugh, Darryn W, Shane R Keating, and Mei-Lin Chen. 2012. "Diagnosing ocean stirring: Comparison of relative dispersion and finite-time Lyapunov exponents". *Journal of physical oceanography* 42 (7): 1173–1185.

Welander, Pierre. 1955. "Studies on the general development of motion in a two-dimensional, ideal fluid". *Tellus* 7 (2): 141–156.

Zilli, Marcia T, and Neil CG Hart. 2021. "Rossby wave dynamics over South America explored with automatic tropical–extratropical cloud band identification framework". *Journal of Climate* 34 (20): 8125–8144.